A Deconvolution Formulation for Cerenkov Light Dosimetry in Radiation Therapy

A DISSERTATION
SUBMITTED TO THE FACULTY OF THE GRADUATE SCHOOL
OF THE UNIVERSITY OF MINNESOTA
BY

Eric Edward Brost

IN PARTIAL FULFILLMENT OF THE REQUIREMENTS
FOR THE DEGREE OF
DOCTOR OF PHILOSOPHY

Yoichi Watanabe, Ph.D.

June, 2019

Acknowledgements

The first project I had with my advisor, Dr. Yoichi Watanabe, came about from a misunderstanding. Dr. Watanabe asked about my background in optics and told me about a research project in his lab concerning "OCT", which I knew previously as optical coherence tomography. What he was really referring to was something completely different - optical computed tomography! I was simply excited to learn that someone was applying optics to medical physics, so I agreed to work on the project. Needless to say, I was slightly confused when I learned that this topic was completely off from what I knew it as. After a few months of working on optical computed tomography, I warmed up to both the subject and to working with Dr. Watanabe. I quickly learned that he is a steadfast and curious person, always willing to dive into a new line of thinking with a student. I approached him during my second year of graduate school about trying experiments with Cerenkov light and scintillation. He took to these ideas quickly and helped us to secure initial funding from the department. This move served as the catalyst for much of the work we went onto produce. Without Dr. Watanabe's help and support, my time in graduate school would have been dim and difficult. He has been a constant source of support and has pushed me to fully explore my research and ideas.

This work would also have not been possible without the support of my friend and mentor, Dr. Adam Green at the University of St. Thomas. Dr. Green gave me my first introduction to optics through a well-designed and challenging undergraduate course. A key component to this course was an intensive series of optics lab experiments, including one on optical tweezers. Without my introduction to this subject by Dr. Green, I would not have gone into optics. He helped to spark my interest in the interface between physics and biology that would eventually bring me to pursue studies in medical physics. Dr. Green has continued to be a strong mentor to me throughout graduate school and

a sounding board for both research ideas and my general well-being.

There are many more people that have provided me with support throughout my graduate studies. I would like to thank Dr. Leah Bar at the Tel Aviv University, Israel, for her work in comparison of the space-variant deconvolution methods presented in this work. Dr. Bruce Gerbi, at the University of Minnesota, has provided me with much guidance and motivation throughout graduate school. Dr. Fadil Santosa, also at the University of Minnesota, has been an invaluable resource for questions on mathematical methods and deconvolution. I would also like to thank my wife and family. My time in graduate school has been much richer with their love and support.

Dedication

For my wife, Rebecca.

Abstract

Cerenkov light is the visible optical emission of photons that are created by the passage of high-energy charged particles in a dielectric medium. Since its discovery in 1934, Cerenkov light has been paramount to applications of high-energy radiation research. Recently, there has been considerable interest in imaging Cerenkov light during external beam radiation therapy as a means to perform in-vivo dose measurement. However, the exact relationship between Cerenkov light emission and dose deposition is not well characterized. In this thesis, the relationship between radiation beam fluence, dose deposition, and Cerenkov light emission is derived in an integral equation, describing the convolution relationships that exist between these physical parameters. This set of equations contained a convolution kernel called the Cerenkov scatter function (CSF). The CSF was solved with Monte Carlo techniques using the Geant4 architecture for medically-oriented simulations (GAMOS) to simulate radiation-induced optical emissions in an optical phantom and human skin tissue model. The theoretical formulation was experimentally evaluated using an optical phantom irradiated by high-energy photon beams. Next, the limitations and dependence of theoretical formulation were tested through a perturbation analysis performed on the CSF through Monte Carlo simulation. Lastly, the theoretical formulation was extended to clinically-relevant geometries, including curved surfaces, by breaking the limitation of space-invariance of the CSF. The theoretical formulation was found to improve the light-to-dose correspondence in Cerenkov light images, particularly in high dose gradient regions, and has the potential to improve the methods of Cerenkov imaging arising within radiation oncology. Based upon these results, it is expected that the theoretical formulation may be extended for use in a new Cerenkov imaging system which couples patient geometry imaging and measurement of Cerenkov light in-vivo.

Contents

List of Tables

List of Figures

Chapter 1

Introduction

1.1 Radiation Therapy

Cancer is the abnormal growth of malignant cells in the body, of which more than 100 different known types exist [5]. The primary symptom of cancer is the growth of lumps of tissue in the body, known as tumors, which are formed by a colony of malignant cells. Without treatment, tumors can bring about many other symptoms and possibly spread or invade other parts of the body through formation of metastases. The most common types of cancer occur in the breast, skin, lung, colon, prostate, or are a lymphoma. Cancer is the leading cause of death in the developed world, where it is estimated that 17-20% of the population will succumb to the disease over the course of their lifetime [6]. Many types of cancer treatments exist including chemotherapy, surgery, and radiation therapy. Different therapy types can be combined to fight tumors depending on the extent and aggressiveness of the cancer. This work is motivated by the radiation treatment of cancer, specifically, on the use of external beams of radiation that are used to treat tumors with a high degree of conformity.

Megavoltage (MV) external beam radiation therapy (EBRT) is the most common type of radiation therapy techniques. To deliver EBRT, a linear accelerator (linac) is used to accelerate electrons to high energies (commonly 6 to 18 megaelectronvolt, MeV) and then treat a patient with either the accelerated electrons or bremsstrahlung photons. The treatment particles cause cell killing through the transfer of their energy to deoxyribonucleic acid (DNA) in the form of dose deposition. Dose deposition as a

function of depth, known as the percent depth dose (PDD), by the treatment particles is well characterized for the range of common treatment types and energies [1]. The radiation treatment is planned such that the dose to the surrounding normal tissues is minimized by using multiple beams with various energies, field sizes, and field shapes in order to conform the expected dose distribution to the treatment volume. The treatment volume may be in a superficial area or deep within the body depending on the type and extent of the cancer. Some dose is inevitably deposited within normal tissues due to the flux of radiation passing through these tissues along the path to the treatment volume. The following sections discuss the medical linac, the nature of dose deposition, and medical dosimetry related to MV EBRT.

1.2 The Medical Linear Accelerator

The treatment of cancer by EBRT can be achieved through the use of either MV electron and x-ray radiation. With sufficient energy, both types of radiation can produce cell killing at a depth within a biological target. In order to reach energies high enough to produce sufficient damage to DNA in the target, a particle accelerator must be used. The primary method of particle acceleration is achieved through the use of a linac. A linac relies on the synchronized operation of many individual components in order to accelerate electrons and produces either electron or x-ray radiation in the MV energy range. An x-ray beam is produced by the linac from the bombardment of a high-Z, tungsten target by high-energy electrons to produce high-energy photons through a bremsstrahlung interaction. Removal of the tungsten target in the beam path allows for electrons to be used in treatment. The final energy output of either the x-ray or electron beam is tunable based upon the electron accelerating parameters used in the linac.

The basic components of a linac are the magnetron or klystron, electron gun, wave-guide, modulator, and the treatment head, as seen in Figure 1.2. The magnetron allows for both the production and amplification of microwaves within the linac. Alternatively, a kylstron can be used in place of a magnetron to amplify waves produced separately by a radio-frequency driver. After amplification by either the magnetron or klystron, the microwaves are sent to the wave-guide. Within the wave-guide, microwaves will

configure into either standing or traveling waves based upon the geometry of the guide. Both standing and traveling waves can be used to accelerate charged particles based upon a electromagnetic interactions. A simple analogy for the interaction can be thought of as a surfer. A surfer gains energy and speed by continuously falling down a wave as it moves forward. In the same way, electrons injected into the wave-guide are accelerated to very high speeds through the electrons interaction with the large potential generated by the amplified microwaves. The electron injection occurs at the distal end of the wave-guide, and electrons gain energy through this interaction as they move down the center of the guide. At the proximal end of the guide, the electrons leave the acceleration area and enter the treatment head.

The treatment head contains multiple components that are used for creating, modifying, and measuring the treatment beam. The primary components in the treatment head can be seen in Figure 1.3 and include the bending magnet, tungsten target, the primary and secondary collimators, the flattening filter or scattering foil, and the ionization chamber. The wave-guide is typically oriented in a plane parallel to the treatment couch, therefore, the accelerated electron beam must first be reoriented downwards. This is achieved through the use of a 270-degree bending magnet or a series of bending magnets. After the bending magnet, the accelerated electrons bombard a high-Z tungsten target. The primary interaction that occurs within the target is a bremsstrahlung, or braking, interaction. The negatively charged electrons experience a force from the positively charged tungsten nuclei through Coulombic attraction. This causes the electrons to change their trajectory and release all or part of their energy in the form of electromagnetic radiation. As seen in Figure 1.2, this interaction produces the x-ray beam. The electron beam enters the tungsten target as a near mono-energetic pencil beam, but after the bremsstrahlung interaction occurs, the exiting x-ray beam can be treated as a poly-energetic diverging beam originating as a point source from the target. The tungsten target is absent from the beam path when the linac is in electron treatment mode, and no bremsstrahlung interaction occurs. When in this mode, a scattering foil is inserted into the beam path that causes the pencil-like electron beam to become divergent. A divergent beam is safer than a pencil beam for treatment because it spreads the focused radiation over a larger area, lowering potential hot spots of beam flux.

Due to the diverging nature of the x-ray beam, more radiation flux is produced at the center of the beam than at the edges. When in photon treatment mode, the flattening filter is place in the beam path for the purpose of making the output profile of the beam to be uniform across the beam path. The flattening filter is designed in a conical shape so that it attenuates a large portion of the central radiation in the beam, converting the output beam from a Gaussian to a square profile. The primary and secondary collimators tailor the shape of the output beam. They can be placed at a variable distance into the beam path to absorb radiation, shaping the beam to a desired size. The basic example of a collimator is called jaws, which can shape the beam into square and rectangular geometry, usually defined as 10x10 cm^2, 20x40 cm^2, ...etc. A more customization collimator is called a Multileaf Collimators (MLC) which are commonly equipped on most modern linacs. The MLC is composed of many sliding and interlocking rectangular leaves, which allow the beam to be shaped much more precisely. Additional accessories such as wedges and beam blocks can be placed at the end of the treatment head to further modify the beam shape and intensity. In addition to modifying the beam output, the treatment head is allowed to rotate 360-degrees about the beam isocenter to allow for varied treatment directions.

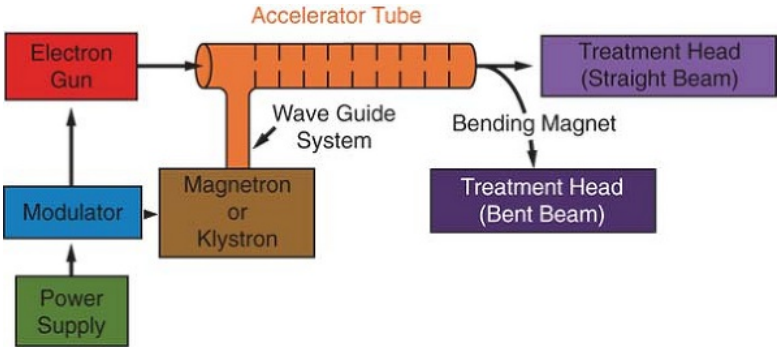

Figure 1.1: The basic components of a linear accelerator. (Figure from Khan, 2010. [1])

1.3 Dose Deposition

The high-energy particles produced by a medical linear accelerator can cause liberation of electrons in the atoms they interact with, known as ionization. The energy required

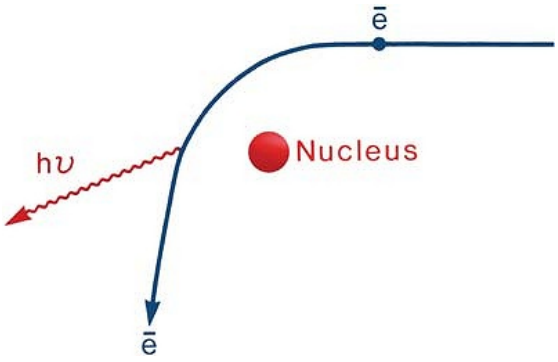

Figure 1.2: A Bremsstrahlung interaction produces the treatment x-rays. (Figure from Khan, 2010. [1])

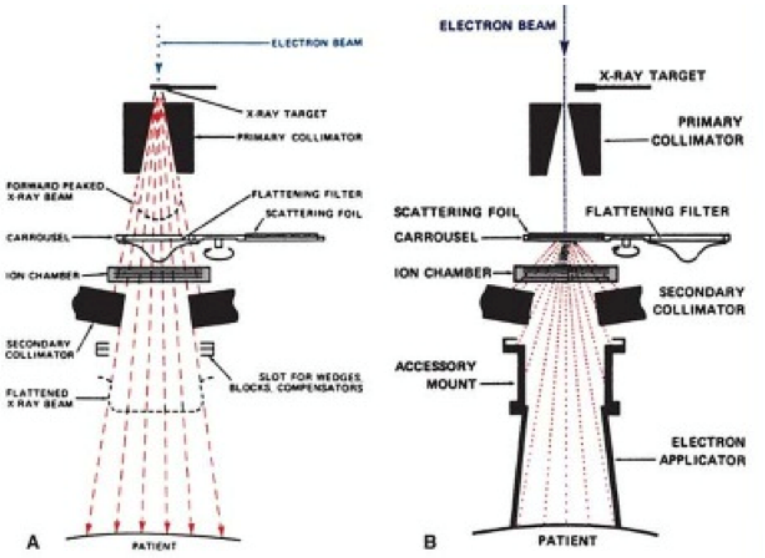

Figure 1.3: The linac treatment head in both (A) x-ray and (B) electron treatment modes. (Figure from Khan, 2010. [1])

for ionization of electrons is dependent upon the irradiated material properties, but is in the eV range for soft tissue materials. The measurement of ionization in air is defined by the quantity exposure which has units of roentgen (C/kg). This definition cannot be applied for all types of radiation and mediums, so the definition of absorbed dose is used instead to describe the quantity of radiation for all ionizing particles, charged and uncharged. Absorbed dose is defined as the energy deposition per unit mass, or $d\epsilon/dm$,

where $d\epsilon$ is the mean energy transferred to a material of mass dm by ionizing radiation [1]. The unit of dose is gray (Gy), which is equivalent to joules per kilogram (J/kg).

Dose deposition in an irradiated medium is due to either the primary or secondary electrons interacting with neighboring atoms. Primary electrons are those that come directly from the linac and are present in electron treatments. Secondary electrons are those that are created by either the primary electrons or by primary photons. Both primary and secondary electrons can interact by the same mechanisms depending on their energy, it is only their origin that differs. All charged particles are capable of dose deposition on their own and are therefore directly ionizing particles. Photons are not responsible for dose deposition on their own but can generate many secondary electrons. Therefore, photons are referred to as indirectly ionizing particles.

The quantity kerma (kinetic energy released in matter), K, is defined as the quotient of E_{tr}, the sum of the kinetic energies of all charged particles liberated by primary photons, by dm [1]. Kerma has the same units as dose (Gy) and is represented by the equation:

$$K = \frac{dE_{tr}}{dm}. \tag{1.1}$$

For a photon beam, the kerma is directly proportional to the beam fluence ψ through the medium:

$$K = \psi \frac{\overline{\mu}_{tr}}{\rho}, \tag{1.2}$$

where $\overline{\mu}_{tr}$ is the mass energy transfer coefficient averaged over the spectrum of the incident photon beam and ρ is the medium density [1]. Kerma can be further decomposed into two parts, collisional kerma K^{col}, arising from inelastic collisions between the secondary charged particles and atomic electrons, and radiative kerma K^{rad}, arising primarily from bremsstrahlung interactions between secondary charged particles and atomic nuclei. A further component of K^{rad} is from photons created by annihilation interactions that are a result of pair-production in the atomic nuclei. Kerma is represented by the equation:

$$K = K^{col} + K^{rad}. \tag{1.3}$$

Radiative kerma results in tertiary photons within the medium which can impart their energy into dose through creation of quaternary charged particles. Collisional kerma has a relationship to absorbed dose D through the equation:

$$\beta = D/K^{col}, \tag{1.4}$$

where β is the ratio of absorbed dose to collisional kerma at a point. The value of β changes depending on the region of the beam, as seen in Figure 1.4. The collisional kerma is highest at the surface of the medium yet the dose reaches a maximum at a depth $z = d_{max}$ beneath the surface, depending on the energy spectrum of the primary beam. Before the point charged particle equilibrium, electron buildup occurs and dose depositing electrons are being created within this region, but depositing their energy at a point further down their path. Beyond the point of charged particle equilibrium, both dose and kerma decrease at the same rate. Transient charged particle equilibrium is established in this region, meaning that dose depositing electrons are being created and terminated at the same rate.

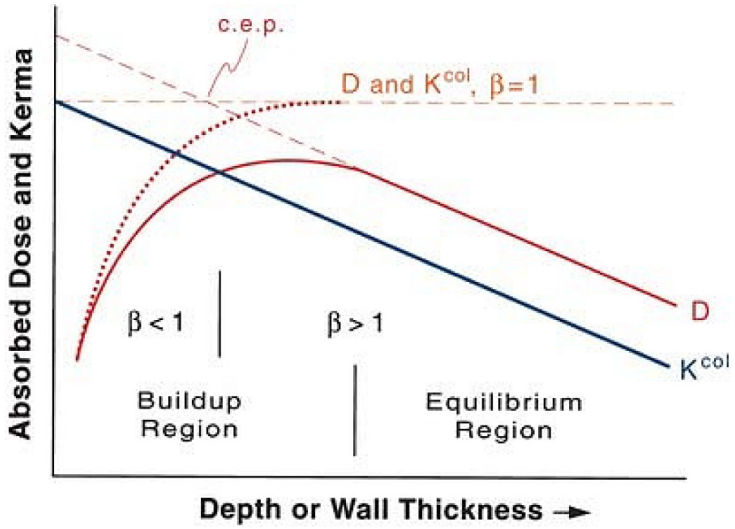

Figure 1.4: The relationship between collisional kerma and absorbed dose as a function of depth. Within the build-up region, electronic equilibrium is no established, and the relationship between kerma and dose is non-linear. Charged particle equilibrium is estabilished at a depth, at which kerma and dose have a linear relationship. (Figure from Khan, 2010. [1])

The result sum of the transfer of collisional kerma to a medium is dose deposition, which varies as a function of depth. As previously defined, the dose as a function of depth along the central axis for a given particle type is called as the percent depth dose (PDD). Various PDDs for common particle types and energies used in radiation therapy can be seen in Figure 1.5.

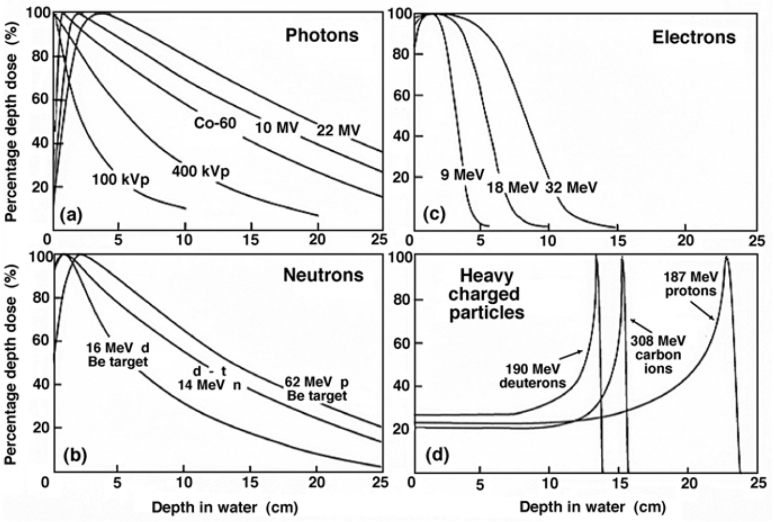

Figure 1.5: The percent depth dose trends in water for photons, electrons, neutrons, and heavy charged particle beams. (Figure from Podgorsak, 2006. [2])

1.4 Interactions of Photons with Matter

This chapter discusses the four distinct interactions between photons and matter: coherent scatter, the photoelectric effect, Compton scatter, and pair production. The definitions for these interactions were adapted from those given by Khan [1].

1.4.1 Coherent Scatter

Coherent scattering, also known as Rayleigh scattering, consists of a photon passing near a bound electron and setting it into oscillation. The oscillating electron reradiates the incident energy in the form of an electromagnetic wave at the same frequency. This interaction can be thought of as a scattering of the incident photon with no loss in

energy. None of the incident energy is exchanged into kinetic energy in the electron due to absorption. The net effect is scattering of the incident photon at small angles. The mass attenuation coefficient of coherent scatter (σ_R/ρ) is proportional to the atomic number of the material (Z) divided by the square of the energy ($h\nu$):

$$\frac{\sigma_R}{\rho} \propto \frac{Z}{(h\nu)^2} \tag{1.5}$$

where σ_R is the coherent scatter cross section. The kinematics of coherent scatter are illustrated in Figure 1.6.

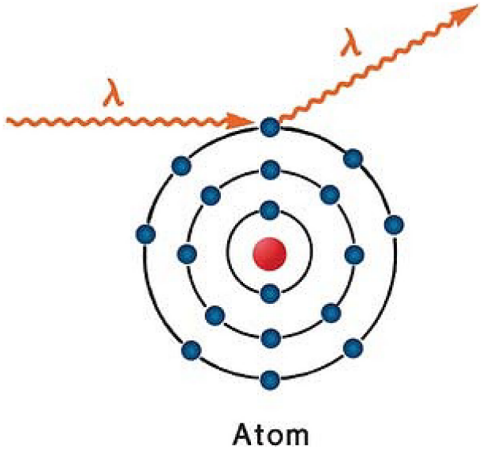

Figure 1.6: An illistration of coherent scatter. (Figure from Khan, 2010. [1])

1.4.2 The Photoelectric Effect

The photoelectric effect occurs when an incident photon interacts with an atom with energy sufficient to eject an orbital electron. The incident photon is completely absorbed and all of its energy is transferred to the orbital electron. The kinetic energy of the ejected electron is equal to $h\nu - E_B$, where $h\nu$ is the energy of the photon and E_B is the binding energy of the electron. The photoelectric effect is the dominant process for low energy photons, and the mass attenuation coefficient for the photoelectric effect (τ/ρ) is roughly proportional to the cube of the atomic number of the atom divided by the energy of the photon:

$$\frac{\tau}{\rho} \propto (\frac{Z}{h\nu})^3 \tag{1.6}$$

where τ is the photoelectric absorption cross section. After the electron is ejected, an orbital vacancy is created and the atom is left in an excited state. The orbital vacancy can be filled by another outer electron with the emission of a characteristic x-ray. The kinematics of the photoelectric effect are illustrated in Figure 1.7.

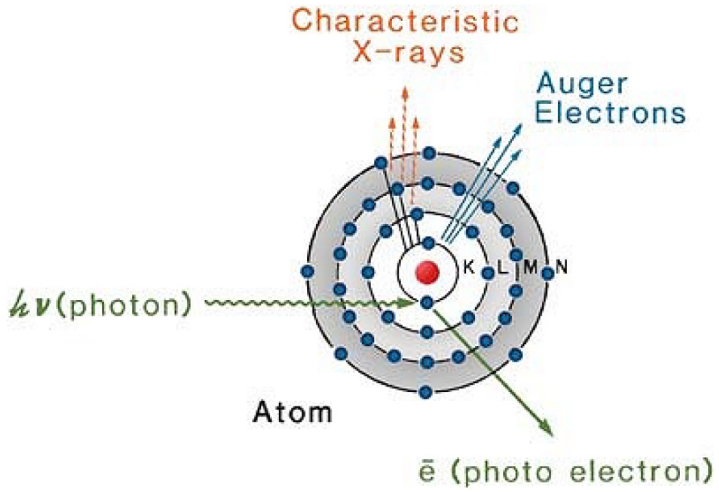

Figure 1.7: An illistration of the photoelectric effect. (Figure from Khan, 2010. [1])

1.4.3 Compton Scatter

Compton scattering occurs when a moderate-energy photon interacts with a 'free' electron and imparts a portion of its energy to the electron, scattering off of it. The electron may be bound to an atom, but is considered free because the energy of the incident photon is much greater than the binding energy of the electron. The mass attenuation coefficient for Compton scattering (σ/ρ) is given by:

$$\frac{\sigma}{\rho} = \frac{N_A Z}{A}\sigma_e \tag{1.7}$$

where σ is the Compton scatter cross section, N_A is Avogadro's number, and σ_e is the Compton scatter cross section per electron, as defined by Klein-Nishina [7]. Compton

scattering is the dominate process in water or tissue for the particle energy range used in radiation therapy, with an effective energy range from about 100 keV to 30 MeV. The kinematics of Compton scatter are illustrated in Figure 1.8.

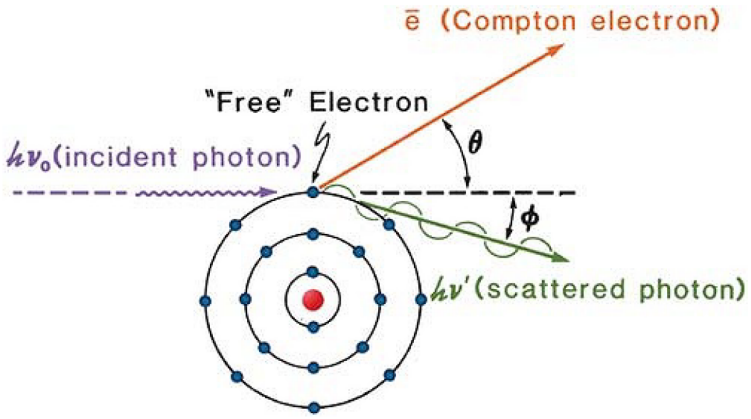

Figure 1.8: An illistration of Compton scatter. (Figure from Khan, 2010. [1])

1.4.4 Pair Production

Pair production is the spontaneous generation of an electron and a positron due to an incident high energy photon interacting with an atomic nucleus. If the energy of the incident photon is greater than 1.02 MeV, it can react with the strong columbic field of the nucleus and generate both β particles. The incident photon is completely absorbed and its energy is imparted to the β particles, which have a combined rest mass equal to $2m_oc^2$. Thus, the net kinetic energy of the β particles is equal to the energy of the incident photon minus the rest masses of the β particles. The mass attenuation coefficient for pair production (κ/ρ) is given by:

$$\frac{\kappa}{\rho} = \frac{N_A}{A}\kappa_a \tag{1.8}$$

where κ_a is the pair production cross section. The kinematics of pair production are illustrated in Figure 1.9.

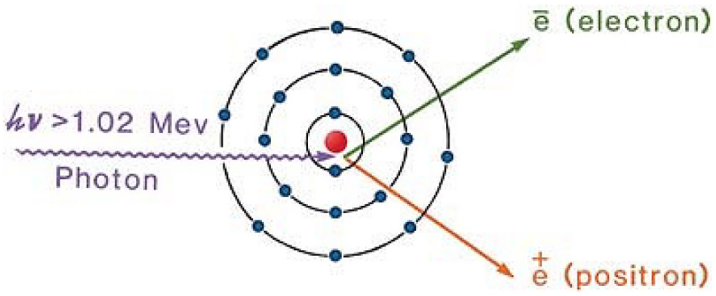

Figure 1.9: An illistration of pair production. (Figure from Khan, 2010. [1])

1.4.5 Total Mass Attenuation Coefficient

The total mass attenuation coefficient (μ/ρ) for a given medium is expressed as the sum of the attenuation coefficients from the individual photonic processes:

$$\frac{\mu}{\rho} = \frac{\sigma_R}{\rho} + \frac{\tau}{\rho} + \frac{\sigma}{\rho} + \frac{\kappa}{\rho} \tag{1.9}$$

where μ is the linear attenuation coefficient for a given medium. The units of the total mass attenuation coefficient are typically given in ($cm^2\ g^{-1}$) and the units of the linear attenuation coefficient are typically given in (cm^{-1}). Each process is more dominate within a given range of energies, as seen in Figure 1.10, which displays the total mass attenuation plotted for both carbon and lead.

1.5 Interactions of Charged Particles with Matter

Whereas photons are indirectly ionizing particles, interacting with matter by the photoelectric, Compton, or pair production processes, charged particles are directly ionizing and interact with matter through a different set of processes. These processes can be broken up into distinct classes but all concern a charged particle interacting with an atom. As shown in Figure 1.11, the interaction is dependent upon the distance of the charged particle from the atomic nucleus (b) and the radius of the atom (a). From the relative size of each factor, the classes of interactions can be defined as: a hard collision (b $\approx$ a), a soft collision (b $>>$ a), or a radiative collision (b $<<$ a). The definitions for these interactions were adapted from those given by Podgorsak [2].

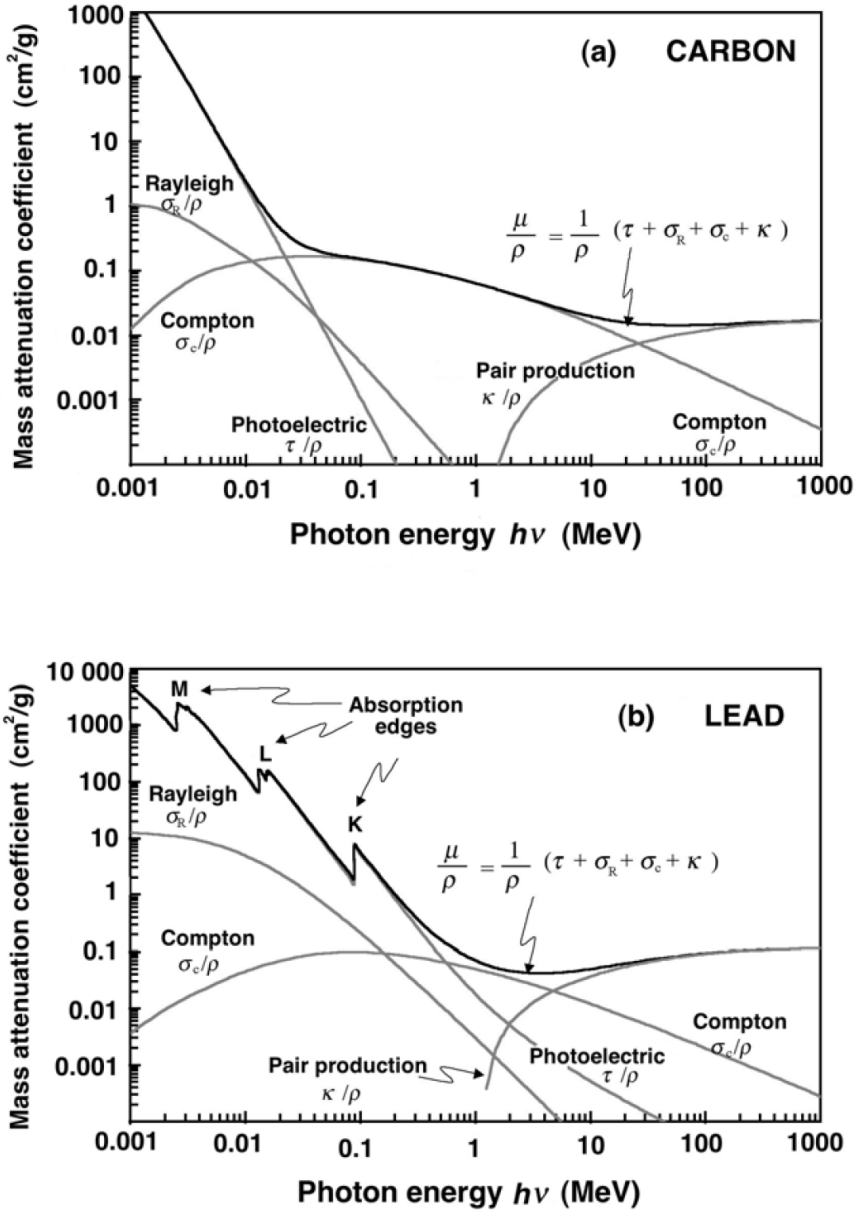

Figure 1.10: The total mass attenuation coefficient for (a) carbon and (b) lead plotted against photon energy. (Figure from Podgorsak, 2006. [2])

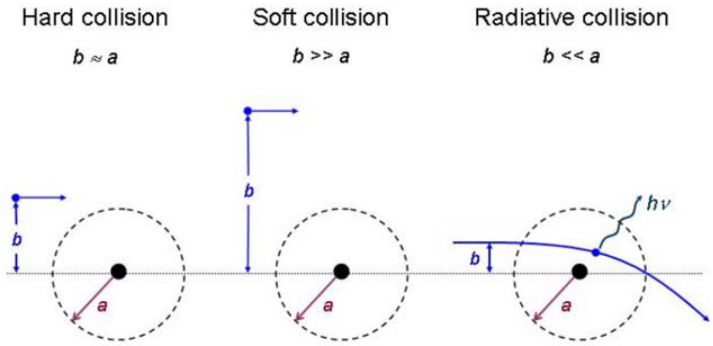

Figure 1.11: The three types of collisions between an atom and a charged particle, depending on the relative atomic distances. (Figure from Podgorsak, 2006. [2])

1.5.1 Hard Collisions

When the distance of the charged particle from the atomic nucleus approaches the atomic radius, the likelihood of a collision between the charged particle and the electron cloud increases. This interaction is called a hard or 'knock-on' collision, and leads to ionization of the atom through an outer shell electron being ejected. A hard collision can be described by Moller scattering and a significant fraction of the incident charged particle's energy can be transferred to the scattered electron. The secondary electron can cause additional ionizations and excitations of neighboring atoms and is referred to as a δ-ray. The δ-ray will continue to lose energy until it can be absorbed as a thermal electron.

1.5.2 Soft Collisions

Soft collisions arise when the distance between the charged particle and the atom is much greater than the atomic radius. In a soft collision, energy will still be transferred to the atom through a weak Coulombic field interaction. This process will cause continuous energy loss to the charged particle, yet, only a small amount of energy is transferred (on the order of an eV) to the atom. With sufficient incident energy, a soft collision can cause either distortion or excitation in the atom. Distortion of the atom can occur when the incident charged particle is traveling faster than the phase velocity of light within the material, leading to coherent optical emission by the Cerenkov effect (see

Chapter 2). Excitation of valence electrons in the atom by charged particles can lead to radiation induced luminescence, or scintillation, within the material. Soft collisions are more probable than hard collisions and therefore account for about half of the total kinetic energy loss from incident charged particles in matter.

1.5.3 Radiative Collisions

When charged particles travel very close to the nucleus, a Coulombic force interaction will occur. In most cases, if the charged particle is an incident electron, it will simply be scattered elastically from the nucleus. In 2-3% of these collisions, the electron will change directions due to the pull of the nucleus and a bremsstrahlung photon will be released. For low energy electrons, the bremsstrahlung photon will be emitted between the range of 60-90 degrees relative to the direction of the electron. For higher energy electrons, the bremsstrahlung photons tend to be in the forward direction. The energy of the bremsstrahlung photon is determined by the proximity of the charged particle to the nucleus, but it can possess up to the full kinetic energy of the electron. The probability of a bremsstrahlung or radiative collision increases with the square of the atomic number divided by the squared mass of the material (Z^2/m^2).

1.5.4 Total Mass Stopping Power

The total mass stopping power (S/ρ) is the sum of the collisional and radiative energy losses of charged particles per unit distance for a given material. It is expressed as:

$$\frac{S}{\rho} = (\frac{dE}{\rho dx})_{col} + (\frac{dE}{\rho dx})_{rad} \tag{1.10}$$

where S is the stopping power, $(\frac{dE}{\rho dx})_{col}$ is the collisional energy loss per unit distance, and $(\frac{dE}{\rho dx})_{rad}$ is the radiative energy loss per unit distance. The collisional energy losses account for both hard and soft collisions. The total mass stopping power is usually expressed with units of (MeV cm^2 g^{-1}). Figure 1.12 displays the total mass stopping power plotted against electron kinetic energy for lead, aluminum, and water.

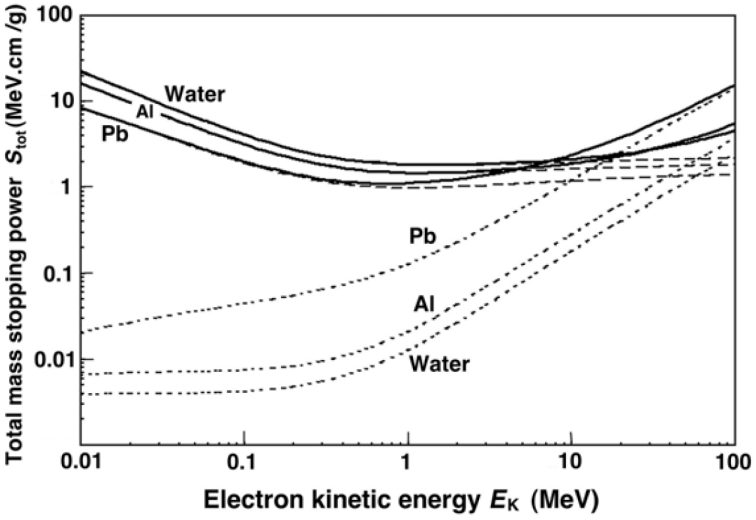

Figure 1.12: The total mass stopping power for water, aluminum, and lead is plotted against electron kinetic energy as solid lines. The collisional stopping power is plotted as the long dashed lines. The radiative stopping power is plotted as the short dashed lines. (Figure from Podgorsak, 2006. [2])

1.6 Quality Assurance

Quality assurance (QA) of linacs is designed to control, monitor, and maintain the operating standards that allow radiation therapy to be a safe option for treating cancer. Due to the nature of the ionizing radiation employed in therapy, when a mistake is made during treatment it can have very serious consequences. To reduce the risk of errors being made, the American Association of Physicists in Medicine (AAPM) has published numerous reports that outline the parameters that should be tested, and their frequency during QA [8]. If these QA guidelines are followed properly, it can not only reduce the risk of errors but also improve the treatment outcomes for patients. Standard QA procedures involve monitoring the mechanical and dosimetric parameters of a linac to reduce the likelihood of an accident, by also increases the chance of identifying and rectifying issues sooner. In addition, a well-established QA program allows for inter-comparisons of results with other radiotherapy centers necessary for clinical trials.

Before a medical linac can be used for clinical treatments, the mechanical and dosimetric parameters must be carefully measured and characterized. This includes calibration of the machine output, acceptance testing, and commissioning. Calibration of the linac involves measurement of the machine's radiation output, which is defined as the dose rate at a given point to a reference depth in water for a 10x10 cm^2 field size along the beam isocenter. Acceptance testing involves checking the electrical and mechanical operations of the linac to ensure the machine is within specifications and tolerances. This involves checking the machine interlocks, radiation leakage, machine rotation, the primary and secondary jaw motion, the light to radiation field alignment, and the patient couch motion. Commissioning of the linac is the most extensive step, which involves collection of all of the radiation beam data using a scanning water tank system. This involves collection of the PDD and beam cross-line profiles for the various treatment energies, field sizes, and particle types, then transferring of this data to the treatment planning system (TPS). After a linac is fully commissioned, on-going QA occurs on a daily, monthly, and annual basis.

1.6.1 Radiation Dosimetry

Modern treatment planning systems and computer technology allow for the delivery of very precise doses of radiation to biological targets, however, this technology is ineffective unless it is properly calibrated and doses are known to exact values. The quantification of these radiation doses is known as dosimetry and allows for verification of doses given to patients on a day-to-day basis in the clinic. Various devices exist for measuring of radiation dose, including: ionization chambers, silicon diodes, plastic scintillators, radiographic and radiochromic film, and gel dosimeters.

The 'gold standard' device for performing dosimetry is known as the ionization chamber, which consists of an air cavity, central electrode, thimble wall, and insulating material. The ionization chamber operates by measuring ions created within the air cavity of the chamber, which are subsequently collected by the central electrode within the chamber. When high-energy radiation travels through the air cavity, a fraction of the energy is transferred to the gas within chamber, creating free electrons that can be detected. The central electrode collects the free electrons as a current, which can then be related to both total ionization charge and dose. A voltage bias is applied

between the chamber wall and the central electrode so that the free electrons will be attracted toward the electrode. If the free electrons recombine with an air molecule, this will result in a loss of signal and an inexact measurement. Another requirement for the ionization chamber is that electronic equilibrium exists within the air cavity. While most electrons are created within the air cavity, some are produced either before or after the chamber. This could cause an either a higher or lower ionization reading respectively, however, if these ionizations are equal then an accurate measurement is still obtained because the loss of charge is equal to the gain of charge. If the ionizations entering and leaving the chamber are equal, then electronic equilibrium exists. In general, performing measurements with ionization chambers requires the use of many calibration factors to convert a reading of ionization to equivalent dose in water. Another limiting factor of the ionization chamber is that all measurements are inherently made in one-dimension (1D).

Silicon diode detectors operate on the same basis as ionization chambers, in that, a measurement of charge liberated in the device can be related to a measurement of absorbed dose. However, the method for charge liberation in silicon diode detectors differs from ionization chambers. When ionizing radiation traverses a silicon diode, electrons in the diode are excited from a bound state to a free state in an electron-hole pair generation. Free electrons are read as charge due to the bias on the diode supplied intrisically from the presence of the N-type and P-type regions. The primary advantage of a diode is that it can be made much smaller than an ionization chamber, but are similarly 1D detectors. Grids of silicon diode detectors are commonly used in the clinic to view beam profiles in a two-dimensional (2D) manner [2].

Plastic scintillators operate on the basis of using optical photons created from fluorescent and phosphorescent electron interactions in the form of scintillation. As charged particles enter a plastic scintillating material, a cascade of soft collisions will occur, creating many optical photons from a single changed particle. Plastic scintillators are commonly used as signal amplifiers on photomultiplier tubes (PMT) due to their high yield of optical photons. In radiation therapy applications, plastic scintillators are typically attached to optical fibers in order to route the optical signal from the linac area to a reading device. Plastic scintillators can be formed into complex geometries or small

sizes, are nearly water equivalent, and are resistant to radiation damage [9, 10]. Scintillator detectors can be used as either 1D detectors or as an array of 2D detectors. However, the soft collisions which provide the scintillation signal in these materials also generate Cerenkov photons, which contaminate the primary signal and are non-trivial to remove [11, 12].

Radiographic and radiochromic films are thin 2D radiation detectors that can obtain dose profiles from single or multiple beam irradiations. Both radiochromic and radiographic films operate through a similar mechanism: incident radiation triggers a localized chemical reaction within the film forming an image of the irradiation profile. The image can be detected as a change in the optical density which can be related to absorbed dose through sensitometric calibration curves. Film provides a distinct advantage over ionization chambers and other 1D dosimeters, in that it can provide the highest resolution 2D dosimetry measurements. However, the development and readout of film can be a time-consuming and delicate process.

Gel dosimeters are a method for measurement of a radiation profile in three-dimensions (3D). Upon irradiation, gel dosimeters will undergo a chemical change which brings about a property change as a function of absorbed dose. Gel dosimeters can be either a Fricke or polymer gel, which can be read out with magnetic resonance imaging (MRI), optical computed tomography (CT), x-ray CT or ultrasound [13]. Gel dosimeters provide the distinct advantage of true 3D dosimetry, however their read-out can be highly sensitive, and diffusion of the ions within the dosimeter can degrade the radiation changes over time [13].

The radiation dosimeters previously mentioned are most commonly used for linac QA and commissioning, but not for in-vivo dose measurements. The radiation dose is rarely measured in-vivo during patient treatment. When it is performed, in-vivo measurements are typically done with 1D devices such as thermo-luminescent dosimeters (TLDs), optically stimulated luminescence dosimeters (OSLs), or diode detectors, which measure the dose only at a point on the patient's skin surface. Film can be used to take a 2D measurement of dose over a patient's skin surface, but is less commonly used. Both TLDs and OSLs relate a measurement of electrons excited to long-lived energy states within the dosimeter to a radiation dose using a calibration curve. A 2D in-vivo dose measurement method could be helpful for evaluating the accuracy of

the prescribed treatment, monitoring hot spots of dose deposition, and improving the therapeutic outcomes of the radiation therapy [14]. However, there is no method that can perform this type of dosimetry in real-time with sufficient accuracy.

1.6.2 Patient Imaging

The ability to verify the patient position prior-to and during each treatment allows for highly conformal treatment plans with a narrow alignment tolerance. The use of imaging techniques to verify the patient position throughout the treatment process is known as image-guided radiation therapy (IGRT). IGRT is a technique that utilizes image guidance as a method to localize the relative positions of a patient's anatomy through various stages of the therapy procedure. Most importantly, it allows for localization of the target just before delivery of a radiation fraction. Imaging data is also taken and utilized during patient data acquisition, treatment planning, treatment simulation, and patient setup [1]. By taking an image just before delivery of each fraction, the location of the target volume can be known precisely on a daily basis.

The purpose of IGRT is to reduce the uncertainties associated with target localization at the time of treatment. Due to inter and intrafractional variations in patient setup, coupled with changes in patient anatomy, the target volume can be positioned differently each day. This introduces inaccuracies and uncertainty to the treatment. The standard approach for accounting for these types of uncertainties was to add geometric margins to the target volume, usually at the expense of maximizing treatment benefits [1]. However, new treatment techniques over the past decade have allowed planning target volumes to be made increasingly conformal through intensity-modulated radiation therapy (IMRT) and three-dimensional conformal radiation therapy (3D CRT). The uncertainty requirements for these techniques are far more stringent, as a geometric miss in treatment due to incorrect patient positioning would result in a large overdose outside of the target volume. Therefore, IGRT reduces target localization uncertainties and has allowed for these highly conformal radiotherapy techniques to be used as viable treatment options.

Several radiographic techniques are available for verifying the patient position before treatment. Modern linear accelerators are commonly equipped with both kV and MV imaging systems. The kV imaging system consists of a conventional x-ray tube with an

opposing flat-panel detector. The x-ray imaging system shares the same isocenter as the treatment head, therefore, imaging with this system provides useful coordinates that can be used in alignment of the patient. The MV imaging system consists of an electronic portal imaging device (EPID) with a flat-panel detector mounted opposite from the treatment head. The treatment head can generate lower MV energy x-rays that can be used to image a patient prior to treatment. While kV imaging systems mounted on linac units have better image contrast than MV portal images, neither methods can visualize soft tissues entirely [1]. Instead, for these techniques, bony landmarks or implanted radio-opaque fiducial markers can be used to localize and position a target prior to treatment.

In order to improve the soft tissue contrast in images used for alignment during IGRT, tomographic reconstruction techniques can be used. These methods rely on filtered back-projection reconstruction of a target volume to generate an alignment image. There are a few ways to take tomographic images for IGRT, including in room CT scanners, MV cone beam CT, and kV cone beam CT. In room CT scanners consist of a conventional CT scanner placed in the treatment room. The CT scanner and the linac share a common axis, typically by using a single couch that can move between the CT scanner and underneath the gantry head. The CT is used to establish the time-of-treatment target configuration, then the couch moves back into treatment position underneath the linac. Cone beam CT (CBCT) scans can be taken using the same on-board kV and MV imaging systems used to take radiographs. Instead of taking a single projection, the x-ray source and image receptor rotate around the patient to capture tomographic data before reconstruction. MV CTs are taken using a Megavoltage beam and the EPID, while kV CTs use a conventional x-ray tube. When comparing MV to kV CBCTs, MV CTs are less susceptible to high Z artifacts and the attenuation numbers are relevant to treatment energies. However, kV CTs exhibit better soft tissue contrast with higher resolution. Other radiographic techniques used for patient positioning include dual, ceiling-mounted, orthogonal x-ray source systems [1].

1.7 Monte Carlo Simulation for Dose Calculation

After commissioning is performed on a linac and TPS, the TPS is capable of planning treatments by optimizing the dose delivered to both normal tissues and treatment volumes. These doses are calculated with CT data using semi-analytical methods such as the convolution-superposition method or by Monte Carlo (MC) simulation [15]. The convolution-superposition method accounts for the indirect nature of dose deposition by including a dose kernel, which is convolved by the primary beam fluence to calculate the 3D dose distribution over a region of interest. The convolution-superposition method is a fast and robust means to calculate dose, but has limited accuracy in complex anatomies with many heterogeneities.

Monte Carlo is considered the 'gold standard' method for calculating radiation dose deposition. It is a model-based computational method which considers the well-characterized probability distributions of the individual photon and electron interactions. Monte Carlo methods operate on an event and step basis, where individual particles traverse through a medium with a probability of an event occurring at each step depending on the event statistics, the particle type, energy, medium, and a random number generator. The full radiation dose is calculated through the generation of many primary particles and the subsequent steps and events that arise from these statistical interactions. Monte Carlo is essential to characterization of the clinical beam emanating for the radiation source in a linac, but can also be used to directly compute the dose distribution with patient CT data.

A simple analogy for Monte Carlo is a pachinko machine, a game where ball bearings are set to fall through an array of rods and pulled downwards by gravity. The rods redirect the falling motion of the ball bearings, which eventually come to rest at the bottom of the machine. If many ball bearings are put through the pachinko machine, it will form a distribution of balls on the bottom of the machine based upon the placement of the rods. In this analogy, the ball bearings can be thought of as the primary particles, their motion is the steps, and the rods are the events. The final distribution of the ball bearings in the pachinko machine is the dose distribution, which is one end result of a Monte Carlo calculation.

Numerous Monte Carlo codes exist for calculations relevant to radiation therapy,

including: ETRAN, ITS, MCNP, EGSnrc, PENELOPE, Geant4, and VCM++. These codes can be divided into two classes depending on their handling of events. ETRAN, ITS, and MCNP are class I algorithms, where all events are grouped together and condensed into a step which includes the full particle history. EGSnrc, PENELOPE, Geant4, and VCM++ are class II algorithms, where events are divided into hard and soft collisions. Soft collisions are predetermined using a set path-length in a medium along with average energy loss over a distance. Hard collisions are simulated as stochastic events above a certain energy threshold.

This work used Geant4 for all Monte Carlo simulations, in particular, the GAMOS (Geant4-based Architecture for Medicine-Oriented Simulations) version 4.0.0 software system [3, 16, 17]. GAMOS was developed for the purpose of applying Geant4 to medically oriented simulation environments and was well suited to simulate the linac geometry and external beam dose deposition. To simulate the optical physics and Cerenkov light emission, the Tissue Optical Modeling plugin was used with GAMOS [18]. Figure 1.13 shows a diagram of the framework of GAMOS, Geant4, and the user input.

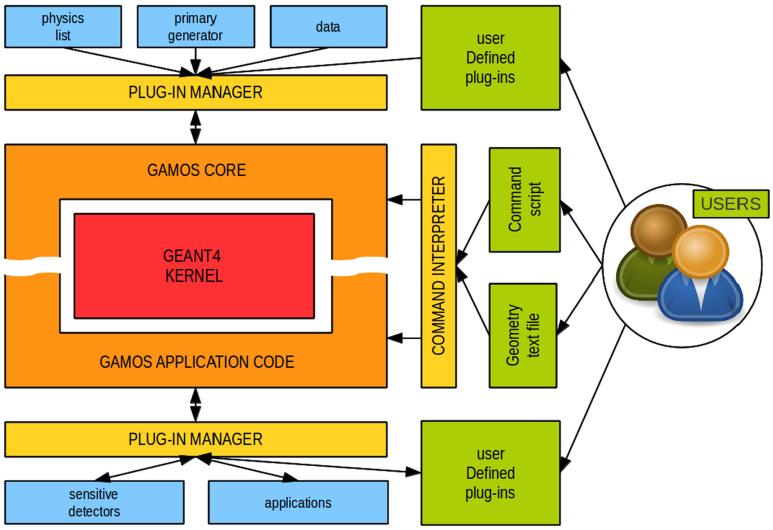

Figure 1.13: The architecture for GAMOS, a Geant4-based Monte Carlo toolkit used throughout this work. (Figure from Arce, et. al, 2014. [3])

The installation of GAMOS used throughout this work was tested by comparing the dose delivered to a water tank using a photon beam on a TrueBeam linear accelerator

(Varian Medical Systems, Palo Alto, CA) to Monte Carlo simulation. The phase space data for the TrueBeam linac was obtained from Varian and used to simulate dose delivered to a tank of water with a 10x10 cm^2 field size at 6 and 10 MV beam energies. This was compared with the commissioning data collected for the TrueBeam used throughout this work.

Figure 1.14 shows a comparison between the Monte Carlo and measured dose and the error with respect to the measured dose for the 6 MV photon beam. Figure 1.14(a-b) shows the PDD and the error along the central axis. The error between the Monte Carlo and measured dose is largest up to a depth of around 1.5 cm, within the build-up region of the beam. Figure 1.14(c-d) shows the cross-line profile and error of the beam at d_{max}. The error between the Monte Carlo and measured dose is largest within the penumbra region of the beam. The errors shown in Figure 1.14 exist within the high gradient regions of the beam, and could be due to slight differences between the measurement and Monte Carlo coordinate systems. Figure 1.15 shows the same comparison for the PDD between the Monte Carlo and measured dose and the error with respect to the measured dose for the 10 MV photon beam. Here, the error is also largest within the build-up region of the beam.

In both Figure 1.14 and Figure 1.15, the highest errors are shown to exist in the regions with a large dose gradient. These errors could be attributed to the finite volume of the ionization chamber used to collected the measured dose data. Agreement of PDDs and the cross-line profiles in other regions validated the use of the Monte Carlo installation.

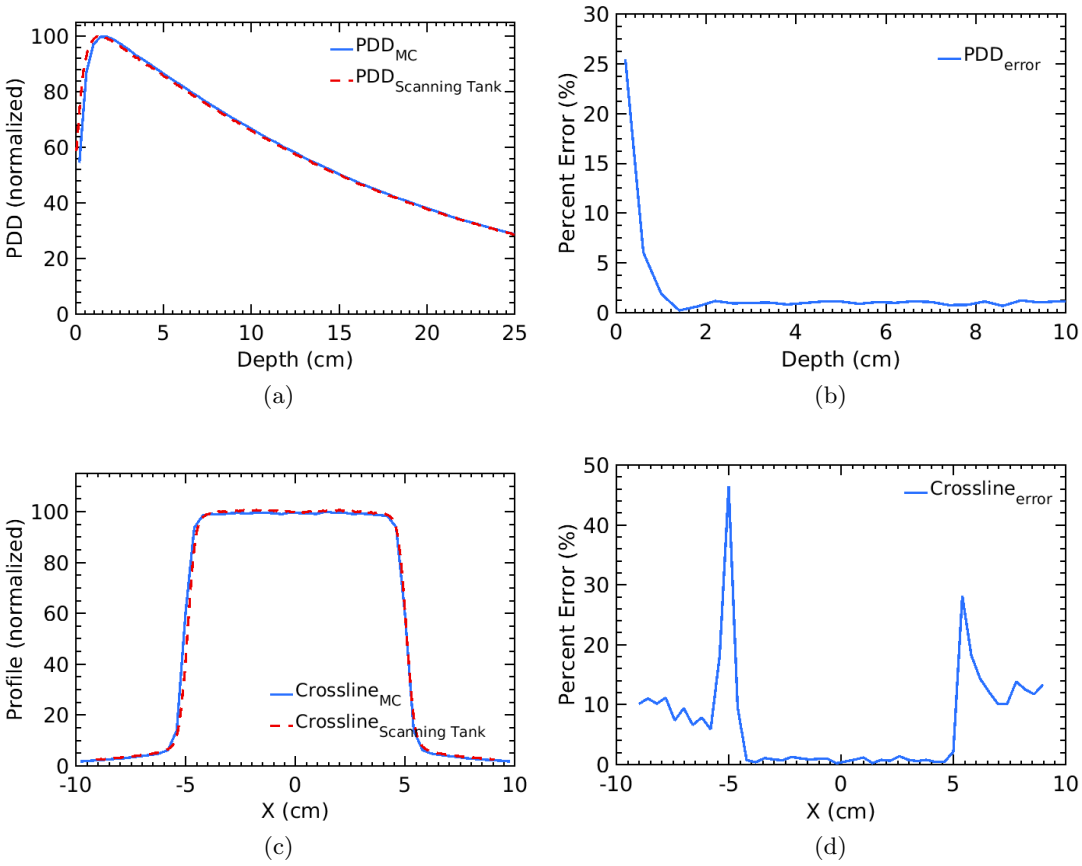

Figure 1.14: (a) The measured and simulated percent depth dose for a 6 MV 10x10 cm^2 field in water from a TrueBeam linear accelerator. (b) The relative error between the trends shown in (a). (c) A cross-line profile for the same beam parameters measured at d_{max}. (d) The relative error between the trends shown in (c).

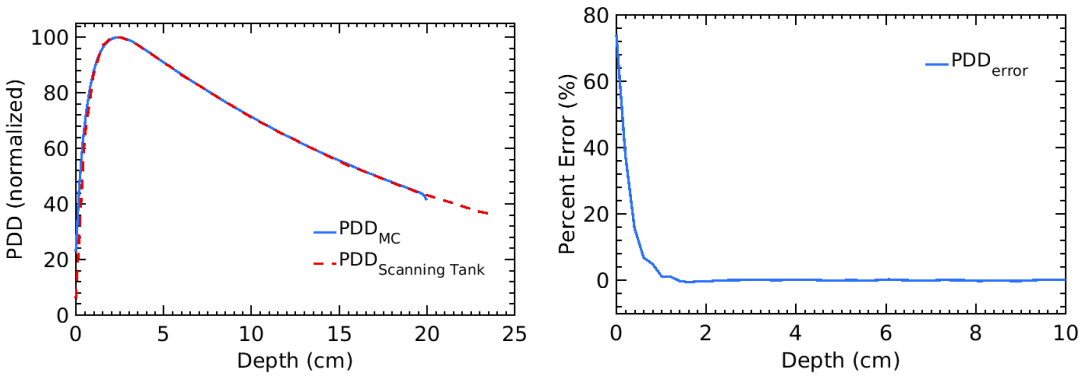

(a) (b)

Figure 1.15: (a) The measured and simulated percent depth dose for a 10 MV 10x10 cm^2 field in water from a TrueBeam linear accelerator. (b) The relative error between the trends shown in (a).

Chapter 2

Cerenkov Radiation

When a charged particle is accelerated or decelerated in free space, it will transfer its kinetic energy to photon radiation through the conservation of energy. A charged particle propagating in free space with uniform linear motion will not radiate any photons. As discussed in the Chapter 1, for a charged particle propagating with uniform rectilinear motion within a dielectric medium, part of its kinetic energy will be transferred to the surrounding medium through soft collisions. These soft collisions will cause local polarization of the neighboring atoms. The polarization reaction occurs at the phase velocity of light in that medium, therefore, if the particle is traveling slower than the phase velocity, the polarization effect is symmetric around the particle. However, if the particle is traveling faster than the phase velocity of light, then the polarization is asymmetric, creating a time-dependent dipole field in the medium. This requirement is written as:

$$v_p > c_n, \text{where } c_n = c/n \tag{2.1}$$

where v_p is the particle velocity, n is the refractive index of the dielectric, and c_n is the phase velocity of light within the dielectric medium. Relaxation of the time-dependent dipole field releases energy in the form of Cerenkov radiation, optical photons in the visible spectrum [19]. A diagram of the atomic-level Cerenkov interaction can be seen in Figure 2.1. This type of reaction can occur when any high-energy charged particle passes through a dielectric that is either transparent or opaque.

This phenomenon was first discovered and coined as the Cerenkov effect in 1934 by Pavel A. Cerenkov and Sergei I. Valilov [20]. In 1937, it was theoretically interpreted by Pavel A. Cerenkov, Igor Y. Tamm, and Ilya M. Frank as the spontaneous emission of visible light by a charged particle traveling faster than the local speed of light in a dielectric medium [19, 21].

A common occurrence of Cerenkov emissions happens with the depleted Uranium fuel from nuclear reactors that is kept underwater for shielding. In this scenario, the fuel appears to be surrounded by a blue glow, which is the Cerenkov radiation. High-energy radiation is emitted from the depleted fuel from fission reactions, which travels through the surrounding water where it emits Cerenkov radiation beginning in the ultra-violet (UV) and blue spectrum. This reaction can easily be seen in water since it is mostly transparent to visible light.

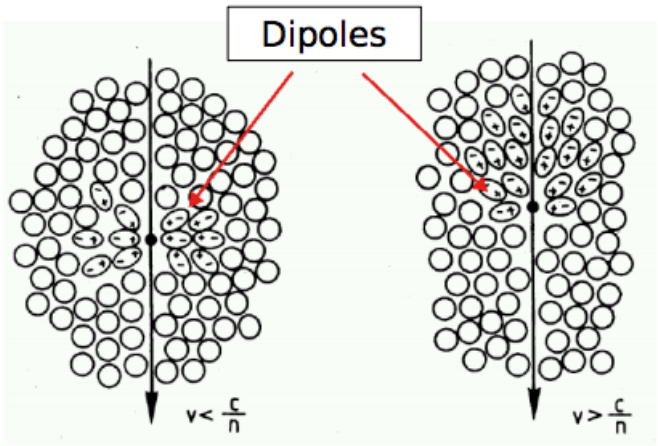

Figure 2.1: The atomic-level interaction of a charged particle passing through a dielectric medium.

2.1 Characteristics

A simple analogy for Cerenkov radiation is that of an optical 'sonic boom'. A charged particle responsible for Cerenkov emission has a velocity that exceeds the local speed of light, therefore, a shock wave effect occurs and the electromagnetic emissions form a

coherent and conical wave front. Cerenkov light is characterized by a cone shaped light emission, where the angle of light emission depends on the n, the index of refraction of the dielectric and v_p, the velocity of the charged particle:

$$\theta_c = cos^{-1}(\frac{c}{v_p n}) = cos^{-1}(\frac{1}{\beta n}) \tag{2.2}$$

where θ_c is the Cerenkov angle, c is the speed of light, and $\beta = v_p/c$ is the relativistic phase velocity. The Cerenkov angle can be solved using the diagram shown in Figure 2.2. β can be defined in terms of kinetic energy as:

$$\beta = \sqrt{1 - \frac{mc^2}{E + mc^2}} \tag{2.3}$$

where E is the kinetic energy of the charged particle responsible for Cerenkov emissions. The minimum charged particle energy, E_{min}, required for Cerenkov emissions to occur is determined by Equation 2.3 as:

$$E_{min} = mc^2(\frac{1}{\sqrt{1 - \frac{1}{n^2}}} - 1) \tag{2.4}$$

As an example, we can solve the Cerenkov angle for a 6 MeV electron beam in water. Using the particle energy of 6 MeV (9.61 x 10^{-13} J), Equation 2.2 can be solved to find a Cerenkov emission angle of $\theta_c = 41.02$ degrees. Due to optical scattering, Cerenkov emissions will disperse from the Cerenkov angle, and in practice, can be viewed from nearby angles relative to the electron beam path.

The spectrum of Cerenkov emissions is governed according to the Frank-Tamm formula [21]. The Cerenkov photon yield per unit path length is a function of the electron energy and refractive index, and varies as a function of the emission wavelength λ:

$$\frac{dN_p}{dx} = 2\pi\alpha z^2 \int_{\lambda_1}^{\lambda_2} (1 - \frac{1}{n^2(\lambda)\beta^2})\frac{d\lambda}{\lambda^2} \tag{2.5}$$

where $\frac{dN_p}{dx}$ is the photon yield per unit path length, α is the fine structure constant (approximately equal to $\frac{1}{137}$), and z is the particle charge. As an example, for the visible spectrum, Equation 2.5 can be integrated from 400 to 800 nm. Using the index of refraction for water, this equation reduces to:

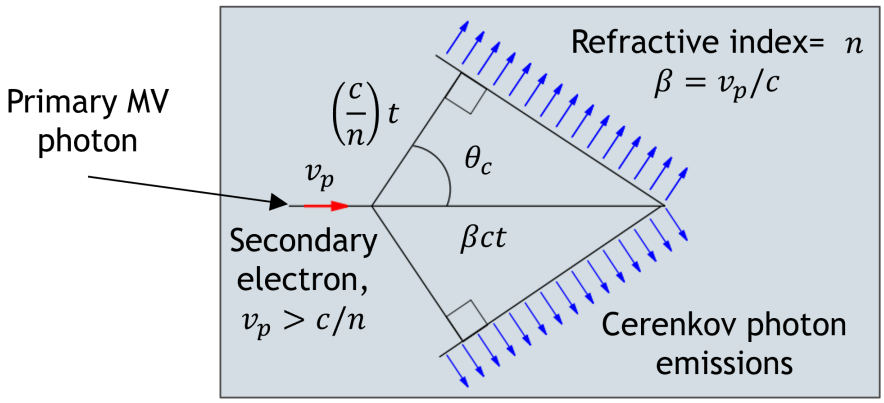

Figure 2.2: The geometry of the conical emission angle of Cerenkov light.

$$\frac{dN_p}{dx} = 490 sin^2(\theta_c). \tag{2.6}$$

This equation shows that electrons in water lose energy at a rate of about 400 eV/cm due to Cerenkov emissions. This amount is about 5000 times less than losses due to ionizations and radiative collisions, which is about 2 MeV/cm in water for electrons. Figure 2.3 displays the number of Cerenkov photon emissions per MeV as a function of electron energy for water, tissue, and plastic materials.

As per equation 2.5, the Cerenkov spectrum is inversely proportional to the square of the wavelength. Figure 2.4 shows an example of a theoretical Cerenkov spectrum. It is heavily blue-weighted, with most of the emissions below 'green' wavelengths, however, the spectrum does extend in the infrared regime and beyond. There does exist a lower limit of wavelength below which, no Cerenkov light is created. This requirement is imposed by the limit due to the inverse cosine in Equation 2.2 that $\beta n \geq 1$. As per Equation 2.3, the value of β is always < 1, therefore this requirement cannot be satisfied for values of $n \leq 1$. For many dielectric materials, this requirement cannot be met in the UV and x-ray range because $n < 1$ in this region of the electromagnetic spectrum. For radiation therapy applications, Cerenkov light is generated beyond a threshold of about 250 keV and can be detected using a camera or measurement device placed in the treatment room.

2.2 Application to Radiation Therapy

Recently, there have been numerous studies on Cerenkov photon imaging in radiation therapy [22, 23, 24, 25, 26, 27, 28, 29, 30, 31, 32, 33, 34, 35, 36, 37, 38, 39, 40, 41, 42, 43, 44, 45, 46, 47, 48, 49, 50, 51, 52, 53, 54, 55, 56, 31, 57] . These included applications in imaging and dosimetry for quality assurance (QA) [22, 23, 25, 26, 27, 28, 30, 32, 34, 35, 40, 44, 47, 48, 52, 57], in vivo dosimetry [24, 29, 36, 37, 46], and basic studies of Cerenkov photon generation using Monte Carlo (MC) simulations [49, 55, 51]. In addition, there is interest in the use of Cerenkov photons as a surrogate for fluorescence-based molecular imaging in both external beam therapy and nuclear medicine[36, 39, 41, 42, 43, 58, 53, 54, 59, 60, 33] . In many of the studies related to QA and in vivo imaging of Cerenkov light produced during EBRT, the intent is typically to measure the dose deposition due to an external beam of radiation incident on either a patient or a phantom through the imaging of Cerenkov photons. These studies share many parallels with those related to plastic scintillation dosimetry, which is currently being explored as a method for QA and in vivo based dosimetry [61, 62, 9, 63, 64, 10, 65, 66, 67, 68, 69, 70, 71, 72, 73, 74]. This thesis was motivated by many of these works and their intent to improve radiation therapy techniques with the use of Cerenkov imaging. The goal of this thesis is to derive a rigid formalism relating imaged Cerenkov photons to dose deposition or primary beam fluence (Chapter 3), characterize and find the limitations of this formalism (Chapter 4), and extend this formalism to clinically-relevant geometries (Chapter 5).

Critical to this thesis is the assumption that Cerenkov photons are generated at the same physical location as dose deposition in an irradiated medium. This assumption was heavily validated by the work of Glaser, et al. (2014) in their publication titled as "Optical dosimetry of radiotherapy beams using Cherenkov radiation: the relationship between light emission and dose" [4]. This work performed a Monte Carlo-based analysis on the relationship between dose deposition and Cerenkov light emission. Monte Carlo simulations were generated for different primary particle types, energies, and irradiated medium.

Figure 2.5 displays the dose and Cerenkov point kernels for a 18 MV x-ray beam in water. Figure 2.6 displays the dose and Cerenkov pencil beam kernels for a 18 MV x-ray beam in water. Figure 2.7 shows the central axis depth curve for dose and Cerenkov

light emission from the pencil beams shown in Figure 2.6. In all figures, the congruence of Cerenkov emission and dose deposition is shown. This study concluded that for mono-energetic pencil beams, the relationship between Cerenkov light and dose is linear with an error of $< 1\%$ over the range of dose deposition. For polyenergetic beams with a finite size, the error as a function of depth varies between 0-5%. This thesis deals with the use of pencil beam kernels and optical diffusion, so the conclusions of Glaser, et al. (2014) serve as a basis for the following chapters.

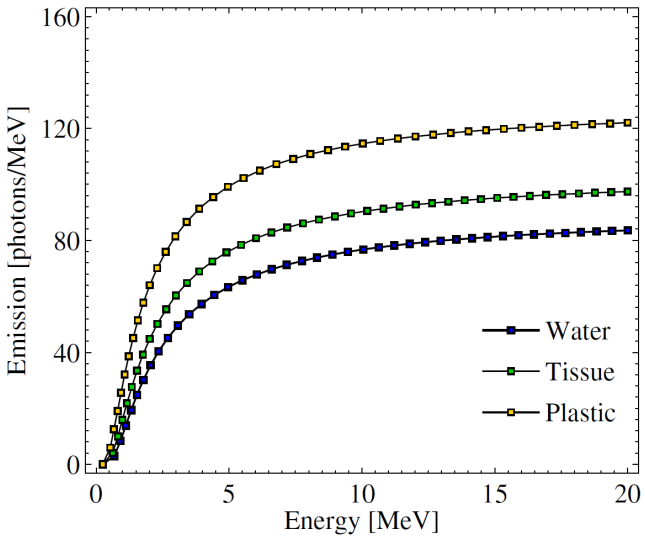

Figure 2.3: The number of Cerenkov photons produced per primary particle for an incident x-ray beam for water, tissue, and plastic materials. (Figure from Glaser, et al. 2014. [4])

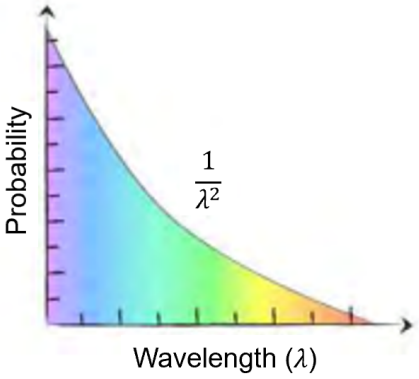

Figure 2.4: A generalized spectrum of Cerenkov light emission, following the inverse square of the wavelength. To the left of this plot, a threshold exists beyond which no Cerenkov light is produced.

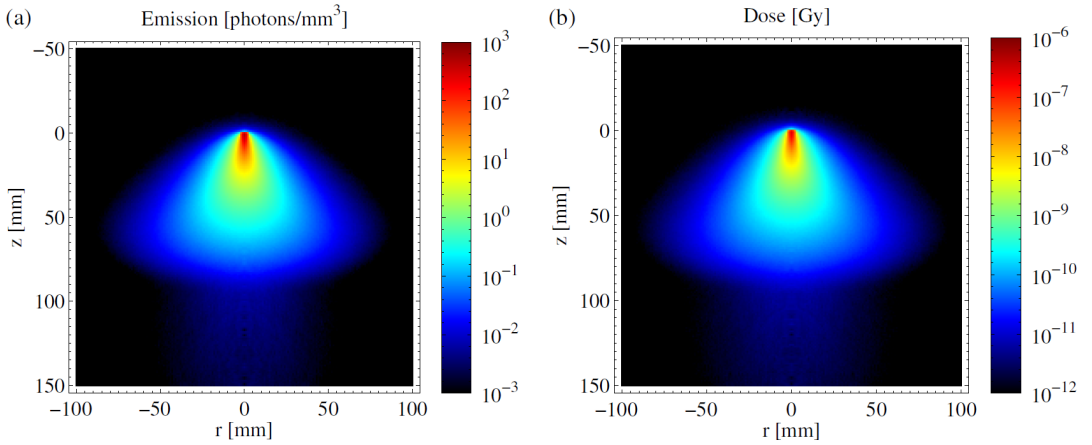

Figure 2.5: The point kernels for (a) the Cerenkov emissions and (b) dose deposition for an 18 MeV x-ray beam in water. (Figure from Glaser, et al. 2014. [4])

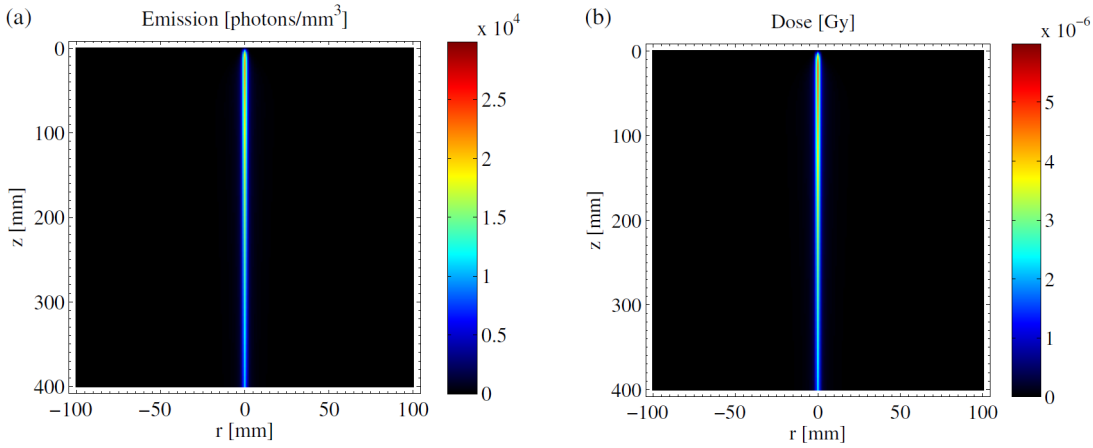

Figure 2.6: The pencil beam kernels for (a) the Cerenkov emissions and (b) dose deposition for an 18 MeV x-ray beam in water. (Figure from Glaser, et al. 2014. [4])

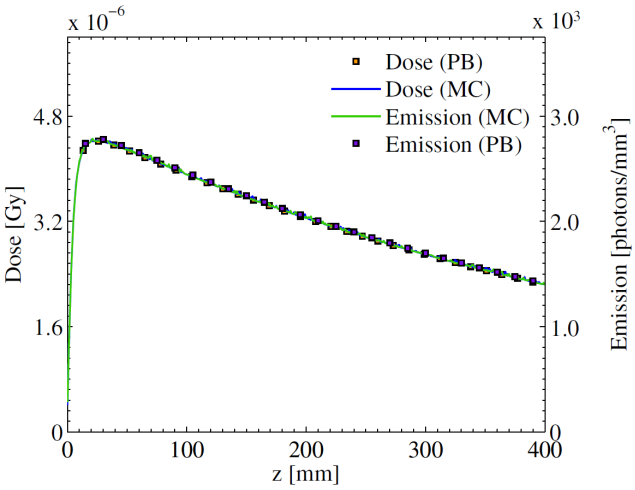

Figure 2.7: The central axis depth dose and depth Cerenkov for the 18 MeV pencil beam kernels. (Figure from Glaser, et al. 2014. [4])

Chapter 3

A Deconvolution Formulation for Cerenkov Light Dosimetry

This chapter is largely derived from: E. E. Brost and Y. Watanabe, "A mathematical deconvolution formulation for superficial dose distribution measurement by Cerenkov light dosimetry." Medical Physics 45(8): 3880-3892 (2018).

3.1 Introduction

In some clinical cases of EBRT, superficial structures and skin may be an intended treatment target or a critical organ where the dose must be limited. In these cases, knowledge of the superficial dose delivered during treatment may improve the therapeutic outcome of the radiation therapy [14]. Superficial dose is measured within the build-up region and depends on both beam and patient parameters including beam energy [75], beam angle [76], field size [77], patient positioning [78], tissue surface structure [79, 80], and tissue composition [81]. These factors, in addition to any error of superficial dose calculated by the treatment planning system, may lead to over- or under-dosing of the skin through the course of EBRT [82].

Current tools used for measuring superficial dose are radiochromic films, ionization chambers, solid diodes, metal oxide semiconductor field-effect transistors (MOSFET), optically stimulated luminescent detectors (OSLD), and thermoluminescent dosimeters (TLD). Although these devices can be used for point or two-dimensional (2D) dose

measurements, none can be used for in vivo 2D dose measurements. A novel dosimetry system utilizing Cerenkov photons generated by high energy photons and electrons allows for in vivo dosimetry during treatment by enabling the physician or physicist to track the superficial dose over the duration of the entire treatment.

Recently, much work has been done to detect Cerenkov photons created by therapeutic radiation beams [22, 23, 24, 25, 26, 27, 28, 29, 30]. These techniques can be used to take high-resolution static or dynamic images of Cerenkov photons [83, 84, 85, 86]. Quantifying the dose deposition based upon Cerenkov photon detection is known as Cerenkov light dosimetry, and it was previously applied to measurement of superficial dose in phantoms [87]. While the practicality of Cerenkov light dosimetry for the dose measurement of EBRT has been shown, performing quantitative dosimetry with this method remains unsolved because this method requires detailed knowledge of the complex relationship between dose deposition and Cerenkov photon emission. Glaser et al. first elucidated the relationship between the dose deposition and Cerenkov photon creation during EBRT using Monte Carlo techniques [4]. They showed that the amount of the Cerenokov light produced by radiotherapy beams is proportional to the absorbed dose within 5% error in a homogenous medium. Zhang et al. quantified the dose deposition per escaped Cerenkov photon by using the Correlation Ratio (CR) in heterogeneous tissue phantoms [55]. These studies have shown that the relationship between dose deposition and Cerenkov photon emission depends on both the characteristics of the radiation beam (particle type, beam energy, field size, source-to-surface distance, beam angle) and the properties of the irradiated medium (surface geometry or curvature, tissue heterogeneity, and the properties of photon scattering and absorption).

The above studies considered the transport of Cerenkov photons to the skin surface as a way to quantify the dose from Cerenkov photons, but they did not explicitly correct for the scattering effects of Cerenkov photons in the medium. Cerenkov photons created within a medium are subject to lateral diffusion as they travel towards the surface. In this chapter, the Cerenkov Scatter Function (CSF) is introduced as a method to account for the diffusive spread of Cerenkov photons [88]. Presented here is a theoretical model and mathematical equations necessary to find the 2D dose distribution at a superficial depth in a medium from an image of Cerenkov photons by introduction of a new scatter kernel, the Cerenkov Dose Scatter Function (CDSF). The equation to find the 2D dose

distribution was solved by an iterative deconvolution method. Monte Carlo simulation techniques are used to solve the scatter kernels used in the formulation. This formulation is validated by comparing experimental results taken with a homogeneous phantom to reference data. The mathematical formulation can be used in either absolute or relative dosimetry, however our experimental validation was performed as relative dosimetry.

3.2 Theory

Figure 3.1 shows a diagram of the physical processes and coordinate system used in the mathematical formulation. Here, a MV photon beam incident on a medium in the Z-direction is considered. An imaging system is placed at some angle relative to the beam on the same side of the medium as the radiation source. The MV photon beam produces secondary electrons which are responsible for both energy deposition and creation of Cerenkov photons within the medium. Cerenkov photons created within the medium will undergo scattering and absorption. Some of the Cerenkov photons will be absorbed, but a fraction is scattered towards the surface and escape from the medium. The fraction of Cerenkov photons that escape the medium is dependent upon the magnitudes of the optical absorption and scattering coefficients of the medium (1% of Cerenkov photons escape from a light-pigmented tissue model). The imaging system can be used to collect the escaped Cerenkov photons and take a planar image of the surface of the medium.

The following integral equation represents the relationship between the fluence of the photon beam entering the medium and the intensity of the Cerenkov photons reaching the imaging system:

$$I(i,j,\theta_{obs}) = \int d\mathbf{\Omega} \int\int dx\, dy \int\int dX\, dY \\ J(x,y,\mathbf{\Omega})\, CSF(x-X, y-Y, \mathbf{\Omega}, \theta_{obs})\, PSF(X-i, Y-j), \tag{3.1}$$

where I is the Cerenkov photon intensity at a pixel (i,j) on the image sensor of the imaging system, J is the total fluence of the MV photon beam with a known energy spectrum entering the medium at the surface point (x,y,z_s) with an entrance vector of $\mathbf{\Omega}$ relative to the surface normal, CSF is the Cerenkov-Scatter Function, and PSF is the

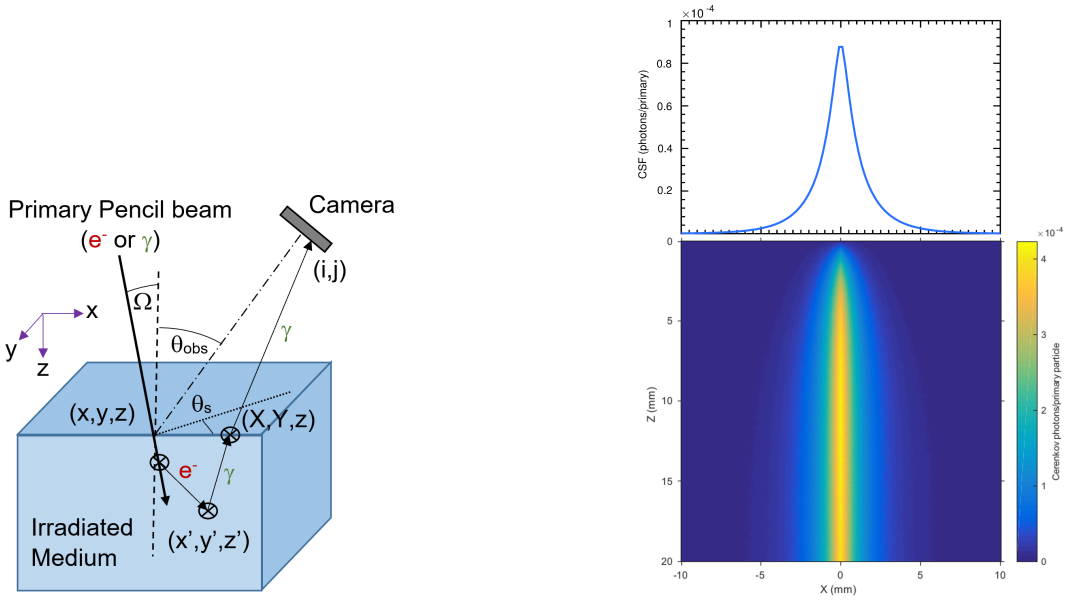

(a) (b)

Figure 3.1: (a) The coordinate system of the Cerenkov photon creation process and subsequent detection by a camera system. γ (photon) and e^- (electron) represent the primary and secondary particle types involved in the transport of energy, respectively. A primary photon pencil beam is incident on a solid block of medium with angle $\boldsymbol{\Omega}$ relative to the surface. The primary photon interacts to create a secondary electron, which then generates a Cerenkov photon. The Cerenkov photon undergoes scattering and absorption within the medium. The CSF is composed of Cerenkov photons that escape the surface. The $\otimes$ symbols represent the interaction points occurring within the medium. Coordinates with a $'$ are under the surface of the irradiated medium. Coordinates (i, j) are at the imaging system. All other coordinates exist on the surface of the medium. (b) A cross-section of the absorption map of Cerenkov photons created by a pencil beam incident on a light skin model. Above the absorption map is a cross-section of the CSF, scaled to the width of the absorption map. The units of (b) are in Cerenkov photons per primary photon particle.

point-spread function representing the transport of Cerenkov photons from the surface at point (X, Y, z_s) to the imaging system. The coordinates x, y, X, and Y are defined on the surface of the irradiated medium at $z = z_s$. The parameter θ_{obs} is the observation angle of the imaging system relative to the surface normal. $\boldsymbol{\Omega}$ can be broken down into the components: θ_{in}, the angle of entrance vector defined from the surface normal and

ϕ, the rotation of the entrance vector about the z-axis.

Using notations similar to Equation (3.1), the three-dimensional (3D) dose distribution, D, at point (x, y, z) in the medium can be expressed by using the energy dependent fluence, j, as follows:

$$D(x', y', z') = \int d\mathbf{\Omega} \int dE \int\int dx\, dy\, j(x, y, \mathbf{\Omega}, E)\, DSF(x - x', y - y', z', \mathbf{\Omega}, E) \quad (3.2)$$

where DSF is the dose scatter function and is often referred to as the dose deposition kernel [14], and E is the incident photon energy.

The CSF in Equation (3.1) represents the number of Cerenkov photons escaping the medium for a pencil beam incident on the surface of the medium and is given by:

$$\begin{aligned} CSF(x - X, y - Y, \mathbf{\Omega}, \theta_{obs}) = \int dE \int\int dx" \; dy" \int\int\int \; dx' \, dy' \, dz' \\ \delta(x - x", y - y", \mathbf{\Omega}) \cdot g(E)\, DSF(x" - x', y" - y', z', \mathbf{\Omega}, E) \\ SC(E)\, F(x' - X, y' - Y, z' - z_s, \mathbf{\Omega}, E), \end{aligned} \quad (3.3)$$

Here, δ is a Dirac-delta function representing a pencil beam entering the medium at the point (x, y, z_s), g is the energy spectrum of the photon beam, SC is the number of Cerenkov photons produced per unit dose, and F is the Cerenkov photon transport from (x', y', z') to the point (X, Y, z_s) on the exit plane. Note that Cerenkov photons are produced at point (x', y', z') by secondary electrons.

The functions CSF, PSF, and DSF in Equations (3.1) and (3.2) are convolution kernels. Hence, these integral equations can be simplified by using the convolution operation $*$ as follows:

$$I(\theta_{obs}) = J(\mathbf{\Omega}) * CSF(\mathbf{\Omega}, \theta_{obs}) * PSF, \quad (3.4)$$

$$D(d_0) = j(\mathbf{\Omega}, E) * DSF(\mathbf{\Omega}, E, d_0). \quad (3.5)$$

Here, the dose deposited in a plane at the depth d_0 is considered. Hence, $D(d_0)$ represents a planar dose distribution.

Equation (3.3) can be rewritten as the convolution of DSF and a new convolution kernel called as the Cerenkov Dose Scatter Function, CDSF:

$$CSF(\mathbf{\Omega}, \theta_{obs}) = CDSF(\mathbf{\Omega}, \theta_{obs}, d_0) * DSF(\mathbf{\Omega}, E, d_0). \tag{3.6}$$

Physically, the CDSF represents the Cerenkov photon production by the secondary electrons and the transport of these Cerenkov photons towards the surface of the medium. Equation (3.6) indicates that CDSF can be found by deconvolving the CSF with the DSF. Inserting Equation (3.6) into Equation (3.4), and using Equation (3.5) for D, I can be expressed as a convolution of D and CDSF as follows:

$$I(\theta_{obs}) = CDSF(\mathbf{\Omega}, \theta_{obs}, d_0) * D(d_0). \tag{3.7}$$

Our aim is to find a 2D dose distribution at a depth in the medium, hence, this becomes a deconvolution problem. The measured Cerenkov photon intensity I can be deconvolved with the known CDSF to obtain the dose profile at the depth d_0.

These formulations required a few assumptions. Firstly, by considering an ideal imaging system, the PSF could be set to be equal to a Dirac delta function. This allows us to ignore the PSF term in Equation (3.4). Secondly, to justify the convolution formulations of Equations (3.4) to (3.7), all convolution kernels must be space-invariant. This requirement can be easily met by considering the incident photon beam to be normal to the surface of the homogeneous medium. Thirdly, the intent of this formulation is to solve for superficial dose within a medium at a depth d_0, which is smaller than the dose maximum depth, d_{max}. Hence, the DSF was found for a plane at the depth d_0, as seen in Equation (3.5).

3.3 Materials and Methods

3.3.1 Monte Carlo Simulations

The GAMOS (Geant4-based Architecture for Medicine-Oriented Simulations) software system was used to generate CSF and DSF functions [3]. The Tissue Optical Modeling

package was used in conjunction with GAMOS to simulate the optical physics and handle optical coefficients of the medium [18]. The CSF and DSF were calculated for a homogeneous optical phantom, which was manufactured to mimic the optical properties of human tissue. The homogeneous optical phantom was fabricated by INO (Ontario, Canada). The optical properties of this phantom were generated from the factory tested coefficients, provided by INO [89, 90]. The absorption and reduced Mie scattering coefficients had values of $\mu_a = 0.3 - 0.0002 \times (\lambda - 450)$ cm^{-1} and $\mu_s' = 114.0$ cm^{-1}, respectively. The index of refraction of the optical phantom was 1.40 for wavelengths from 400-800 nm.

Three types of Monte Carlo simulations were performed. The first simulations were done to obtain CSF. The simulation model consisted of a radiation source and the optical phantom. The radiation source was a pencil beam directed at the optical phantom with a constant beam angle of $\theta_{in} = 0°$. The material geometry was the optical phantom modelled as a box of 20x20x20 cm^3 dimensions. The medium had both radiological and optical properties to simulate tissue for both MV photons and low-energy Cerenkov photons. These simulations utilized the photon energy spectra of 6 MV, 10 MV, and 18 MV beams for the TrueBeam linear accelerator (Varian Medical Systems, Palo Alto, CA) [91]. The initial position and direction at the time of the Cerenkov photon creation and the final position and final direction at which the Cerenkov photon escaped the phantom were recorded. The CSF was calculated by scoring the flux of the Cerenkov photons which escaped from the phantom surface. The positions of the photons leaving the surface were scored in a grid of 0.2x0.2 mm^2 pixels. The second type of Monte Carlo simulation was performed to obtain the DSF function. The dose was scored in voxels of 0.2x0.2x2.0 mm^3 for an incident pencil beam with the same photon energy spectra as those used for the CSF simulation. As mentioned in Section 3.2, the DSF function was calculated on a plane at the depth of 10 mm. The third type of Monte Carlo simulation was done to obtain the dose distributions on a plane at the depth of 10 mm (or d_0) for photon beams with various field sizes. For this simulation, the 6 and 10 MV phase space data of a TrueBeam linac were obtained from Varian [92].

All Monte Carlo simulations were run on an in-house cluster of eight computers with Pentium processors running on the Linux platform. A large number of histories were used to achieve high statistical precision of computed values and reduce the error in

dose calculations to less than 1%. The error in the dose calculations were calculated by GAMOS. The total number of histories were 2.0×10^7 and 2.0×10^{11} for CSF and DSF calculations, respectively. Dose calculations using the TrueBeam phase space file were run with 1.5×10^9 histories.

3.3.2 Cerenkov Dose Scatter Function

The CDSF was calculated by deconvolving the CSF with the DSF with Equation (3.6) using a custom written Matlab program utilizing the deconvlucy function. For superficial regions, the lateral spread of dose represented by the DSF was much less than the CSF. Therefore, the shape of the CDSF was not significantly different from the shape of the CSF. However, the CDSF obtained from Equation (3.6) was prone to noise artifacts; hence, the function was fit and remapped to be symmetric about the axis of the incident pencil beam to reduce uncertainty. For the fitting, the original distribution was sampled along a line from the center of the pencil beam outwards to a radial distance of 20 cm. The fitting used spoke-sampling centered at the origin of the pencil beam entering the medium surface. A diagram illustrating the spoke-sampling schema can be seen in Figure 3.2(a). The sampling was performed for sampling angles 0-345° (θ_s), at 15 degree increments. The mean of all samples was fit using a double-Gaussian distribution in the following formula:

$$CDSF_{mean}(A1, B1, C1, A2, B2, C2, r, d_0) = A1e^{-\frac{(r-B1)^2}{C1^2}} + A2e^{-\frac{(r-B2)^2}{C2^2}}, \tag{3.8}$$

where $CDSF_{mean}$ is the mean of the sampled cross-sections from the original CDSF. Parameters $A1$, $B1$, $C1$, $A2$, $B2$, and $C2$ are the fit coefficients, and r is the radial distance. Fitting of the CDSF can be seen in Figure 3.2(b). The CDSF was normalized such that the peak value equaled one.

3.3.3 Imaging Experiments

Cerenkov images were captured using a Canon EOS 6D commercial camera equipped with a 20.2-megapixel CMOS sensor and square pixel size of 6.55 μm (Canon USA, Huntington, NY). The optical phantom mentioned in Section 3.3.1 was used in all

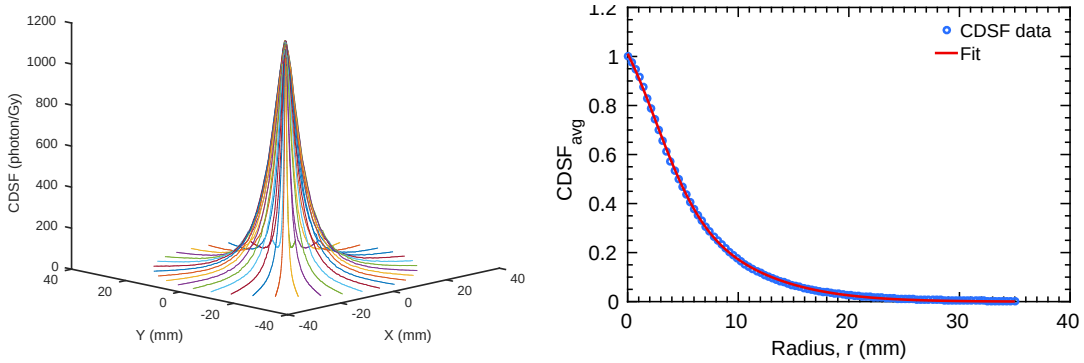

(a) (b)

Figure 3.2: Visualization of the (a) sampling and (b) fitting of the CDSF for 6 MV pencil beam from the optical phantom. (b) shows the normalized mean of all spoke samples displayed in (a). The curve in (b) was remapped to generate a CDSF distribution radially symmetric about the origin, which was used in the deconvolution formulation.

experiments. A diagram and photons of the experimental setup can be seen in Figure 3.3. The optical phantom was mounted to the gantry head of the TrueBeam. The mount kept the imaged surface of the optical phantom normal to the radiation beam at all times. The optical phantom surface was placed at 100 cm source-to-surface distance. The camera was placed at a distance of 100 cm from the optical phantom surface with an imaging angle of $\theta_{obs} = 45°$. The camera was controlled using the default commercial software, EOS Utility, (Canon USA) which allowed for remote shooting through a USB cable on a laptop computer placed at the linac control console. A custom camera mount was used to place a 45° mirror between the camera and the phantom. This was used to reduce stray radiation in the projection area of the CMOS detector and enabled us to place the camera behind lead shielding. The room was darkened as much as possible to reduce stray light to the camera through blocking and turning off of lights.

Three different data sets were taken during imaging experiments. These data sets allowed us to evaluate the dependence of the Cerenkov photon image on dose rate (Dataset A), photon energy (Dataset B), and field size (Dataset C). Dataset A was obtained using a dose rate varied from 200 to 600 MU/min with a 6 MV photon beam and a 5x5 cm^2 field size. Dataset B was taken with 6 MV, 10 MV and 18 MV photon beams at 600 MU/min and a 5x5 cm^2 field size. Dataset C was collected for field sizes

of 0.6x0.6 and 1x1-10x10 cm^2 at a 1 cm increment with a 6 MV photon beam at 600 MU/min. Two more complex fields were also imaged with Dataset C – a 60° hard wedge and an irregular shape created by the MLC. The acquisition parameters of the camera for all experiments can be seen in Table 3.1.

Table 3.1: Camera and linac parameters used in imaging experiments.

Images	ISO	Exposure time	Exposure rate	Energy	Averages
Open fields	1000000	1/6”	600 MU/min	6, 10, and 18 MV	10
Wedged fields	1000000	6”	600 MU/min	6 MV	10

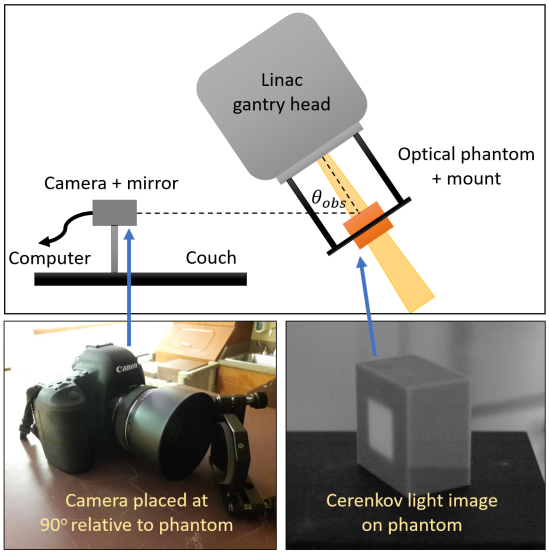

Figure 3.3: The experimental setup used to image Cerenkov photons during EBRT. A commercial CMOS camera was place behind shielding on the treatment couch. A mount was connected to the ganrty head which held the optical phantom used throughout the imaging experiment. Photon images were taken with the room lights off, and subsequently time and spatial filtered after acqusition.

3.3.4 Image Processing

The Cerenkov image data obtained from experiments were taken in the RAW image format in greyscale and then converted into TIFF format. 10 individual images were averaged for each measurement to reduce stray radiation noise. The resulting image

was spatially-filtered by a 15-pixel Gaussian-filter. The use of a Gaussian-filter induced additional blur in images, however, it did not alter the shape of the Cerenkov image profiles. Instead, the application of the filter significantly improved the signal-to-noise ratio (SNR). The SNR was measured in images using the mean value in an area of the Cerenkov signal divided by the mean value found in a background area. The SNR could be further improved through use of background subtraction but was found to not make a significant difference in our images.

When the image was first captured, all images of the phantom surface were distorted due to the imaging angle between the camera and the surface normal. To compare the imaging results with the Monte Carlo simulations, the shape of the Cerenkov images was perspective corrected. A registration image was taken with the room lights on and the beam off. The room-lit image was used to select the four corners of the imaged surface of the phantom (Q). A transformation matrix (T) was used to transform the distorted area to an objective square surface (P). The matrices P, Q, and T were given by:

$$P = \begin{pmatrix} x_1 & x_2 & x_3 & x_4 \\ y_1 & y_2 & y_3 & y_4 \\ 1 & 1 & 1 & 1 \end{pmatrix}, Q = \begin{pmatrix} u_1 & u_2 & u_3 & u_4 \\ v_1 & v_2 & v_3 & v_4 \\ 1 & 1 & 1 & 1 \end{pmatrix}, T = PQ'QQ'^{-1}, \tag{3.9}$$

where $((x_1, y_1), (x_2, y_2), (x_3, y_3), (x_4, y_4))$ are the coordinates of the four corners of phantom in the distorted image and $'$ is the transpose operation [87]. The coordinates $((u_1, v_1), (u_2, v_2), (u_3, v_3), (u_4, v_4))$ are the four corners of an objective square. T was applied to each distorted Cerenkov image (I_0) to yield a perspective corrected image (I) with the equation $I = TI_0$. After the perspective correction was applied, the resulting image was cropped to contain only the top of the optical phantom. This image was set so that the pixel dimensions matched that of CDSF. This image processing schema loosely followed what has been employed in other Cerenkov imaging studies with a stand-alone CMOS detector [87, 93].

All datasets were deconvolved by the CDSFs corresponding to the energy of the beam used according to Equation 3.7. Dataset B was additionally deconvolved by the CSFs for each energy to solve and compare the beam fluence for a 5x5 cm^2 field, according to

Equation 3.4. For the deconvolution calculations, the iterative deconvolution algorithm was used in ImageJ (NIH, Washington DC), available as the plugin "Iterative Deconvolve 3D" [94]. Additional filters were turned off for the deconvolution step. The effects of one to five iterations of deconvolution were tested on the cross-line dose profiles of the Cerenkov imaging data.

3.3.5 Data Analysis

The relationship of image intensity to dose rate, photon energy, and field size was found using all three datasets. The image intensity was obtained by taking the mean of the pixels in a 0.5x0.5 cm^2 area at the center of each field image. The error was expressed by the standard deviation of the pixel values. Deconvolved Cerenkov images for a 10 mm depth were used for these tests.

Cross-line profiles were obtained from Dataset C. The cross-line dose profiles of both the raw Cerenkov images and the deconvolved images were compared with Monte Carlo results. Each cross-line profile was normalized to measure the penumbra, field flatness, and field width. The penumbra was defined as the width of the 20% to 80% of the maximum value and the mean value was found from all four sides of the field. The field flatness was found using the following equation:

$$Flatness = 100 \times (D_{max} - D_{min})/(D_{max} + D_{min}) \tag{3.10}$$

where D_{max} and D_{min} were the maximum and the minimum values across the central 80% of the field width. The beam width was defined as the full width at half of the maximum value of intensity or dose and the mean value was found using both the X and Y-directions. The percent error of these measurements was calculated in comparison to the reference data which were obtained either by Monte Carlo simulations or from the machine commissioning data. Additional comparisons of cross-line profiles of the 5x5 cm^2 fields for different energies were performed using the raw Cerenkov images and fluence profiles, which was obtained by using the CSF as per Equation 3.4.

2D dose distributions from deconvolved Cerenkov images were compared against reference dose data taken with radiochromic film using a custom written Matlab program.

Radiochromic film dose was taken at a 10 mm depth in solid water. Dose distributions were obtained for four fields within Dataset C (0.6x0.6, 1.0x1.0, 3.0x3.0 cm^2, and irregularly shaped).

3.4 Results

Figure 3.4 shows all major components of the imaging protocol. An example of the CSF, DSF, and CDSF for a 6 MV photon beam with $\theta_{in} = 0$ can be seen in Figure 3.4(a-c). An example of a distorted, perspective corrected, and processed Cerenkov image for a 5x5 cm^2, 6 MV beam can be seen in Figure 3.4(d-f).

The Cerenkov photon intensity of the deconvolved images was found to have linear relationships with beam dose rate, which was in agreement with previously published data and therefore verified our methods [87]. This result can be expected because more Cerenkov photons are created per image exposure as dose rate increases. The Cerenkov photon image intensity was found to decrease with increasing beam energy. This is primarily due to the wider build-up region that occurs for higher beam energies. Cerenkov photons are created with a linear relationship to dose, so more Cerenkov photons are created deeper within the optical phantom for higher beam energies. Cerenkov photons will undergo more absorption as the distance to the medium surface increases. The net effect of these physical mechanisms explains the observed data. The Cerenkov photon intensity as a function of field size was found to be similar to the beam output factor of the TrueBeam for field sizes greater than 1x1 cm^2. This is simply explained by larger beam output with increasing field size. It is interesting to see if the Cerenkov light dosimetry can be used for the beam output factor measurements, in particular, for small field sizes with further improvements in the technique.

Tables 3.2 and 3.3 show the field size, penumbra width, and flatness for the unprocessed raw images and single-iteration deconvolved images for 6 and 10 MV beam energies. Deconvolution of raw images reduced the errors of both the field size and the penumbra width. Deconvolution by a single iteration changed the absolute mean error in the field size from 0.95% to 0.97% and in the penumbra from 33.47% to 5.02% for the 6 MV beam data. Deconvolution also reduced the field flatness overall for the 6 MV beam data. The 10 MV beam data displayed an over-correction in the penumbra width

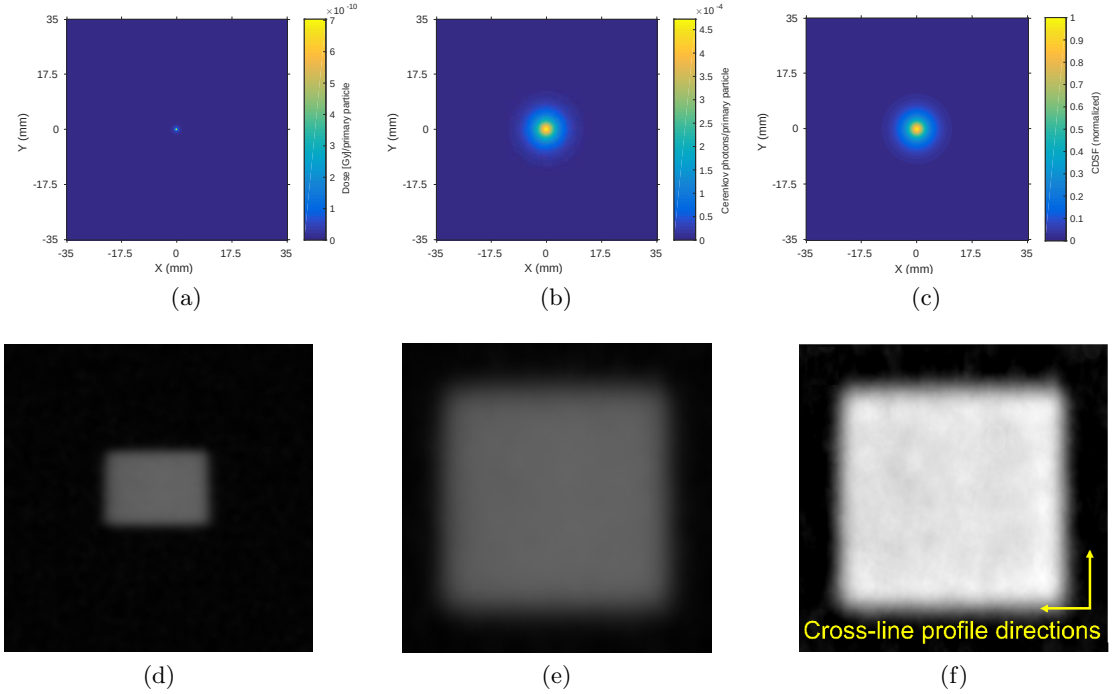

Figure 3.4: Images of the (a) DSF, (b) CSF, (c) CDSF, (d) time-averaged Cerenkov image, (e) perspective corrected image, and (f) deconvolved image from the optical phantom with a 6 MV, 5x5 cm^2 beam. Image (a) represents the DSF, and was obtained with Monte Carlo using a 6 MV pencil beam incident on the simulated optical phantom. It is the lateral dose spread at a 10 mm depth. Image (b) represents the CSF, and was obtained using the same Monte Carlo simulation, scoring Cerenkov photons that escaped from the surface. Image (c) represents the CDSF, and was obtained by deconvolving image (b) by (a). Image (d) is the time-averaged data from an experimental image. Image (e) is a perspective corrected version of Image (d). Image (f) was obtained by deconvolving Image (e) by Image (c). Images (d-f) have dimensions of 7x7 cm^2.

after a single iteration of deconvolution, from a 33.6% error to -14.0%. The field size measurement was relatively unaffected by the deconvolution process for all fields.

Table 3.4 shows the percent error in the measurements of field size, penumbra, and beam flatness for a 5x5 cm^2 beam as a function of iterations used in the deconvolution step. These results showed that the field size and penumbra width decreased with an increase in the number of iterations. A single iteration yielded the smallest percent error. As additional iterations were performed, the penumbra width and field size deviated

further from the true values. Multiple iterations appear to over-correct the beam profile. The absolute mean error in the penumbra increased from 5.02% to 16.94% between one and two iterations. The error in the beam width did not change significantly with increasing iterations. Additional deconvolution iterations increased the field flatness. Figure 3.5 shows a comparison of the measured and the Monte Carlo results for a 5x5 cm^2 for raw Cerenkov image (a), the Cerenkov image processed with one iteration (b), and two iterations (c).

Table 3.2: Field size, penumbra width, and flatness for varying field sizes from the cross-line profiles taken from raw images. The percent error of measurements are given relative to Monte Carlo calculated dose curves, which have values shown in parentheses.

	Raw Image			% Error	
Field Size (cm^2) - Energy	Width (cm)	Penumbra (mm)	Flatness	Width	Penumbra
1x1 - 6 MV	1.10 (1.05)	4.90 (3.90)	23.28%	4.76%	25.6%
2x2 - 6 MV	2.05 (2.04)	5.25 (4.25)	14.96%	0.49%	23.5%
3x3 - 6 MV	3.07 (3.07)	5.60 (4.40)	11.57%	0.00%	27.3%
4x4 - 6 MV	4.09 (4.10)	5.80 (4.45)	9.66%	-0.24%	30.3%
5x5 - 6 MV	5.14 (5.13)	6.05 (4.40)	4.95%	0.20%	37.5%
5x5 - 10 MV	5.18 (5.13)	6.68 (5.00)	0.86%	0.97%	33.6%
6x6 - 6 MV	6.16 (6.16)	7.20 (4.60)	4.75%	0.00%	56.5%

Table 3.3: Field size, penumbra width, and flatness for various field sizes from the cross-line profiles taken from single-iteration deconvolved images. The percent error was calculated relative to Monte Carlo calculated dose curves for the given field size.

	Deconvolved Image - 1 Iterations			% Error	
Field Size (cm^2) - Energy	Width (cm)	Penumbra (mm)	Flatness	Width	Penumbra
1x1 - 6 MV	1.02	3.65	27.43%	-2.86%	-6.41%
2x2 - 6 MV	2.02	4.05	12.98%	-0.98%	-4.71%
3x3 - 6 MV	3.06	4.10	7.88%	-0.33%	-6.82%
4x4 - 6 MV	4.08	4.25	5.90%	-0.49%	-4.49%
5x5 - 6 MV	5.12	4.45	2.48%	-0.19%	1.14%
5x5 - 10 MV	5.13	4.30	1.54%	0.10%	-14.0%
6x6 - 6 MV	6.10	4.30	3.79%	-0.97%	-6.52%

Figure 3.6 shows the cross-line profiles of 6 MV 2x2, 3x3, 4x4, and 5x5 cm^2 field size beams. Figures 3.6(a), (c), (e), and (g) show the profiles of raw Cerenkov images

Table 3.4: Field size, penumbra width, and flatness for a 6 MV, 5x5 cm^2 open field cross-line profile as a function of the number of iterations used in deconvolution. The percent error was calculated relative to Monte Carlo calculated dose curve for a 5x5 cm^2 field size.

	Deconvolved Image			% Error	
Decon. Iterations	Width (cm)	Penumbra (mm)	Flatness	Width	Penumbra
0	5.14	6.05	4.95%	0.20%	37.50%
1	5.12	4.45	2.48%	-0.19%	1.14%
2	5.11	3.90	3.61%	0.39%	-11.36%
3	5.11	3.60	4.38%	0.39%	-18.18%
4	5.10	3.40	4.76%	0.58%	-22.72%
5	5.10	3.25	4.96%	0.58%	-26.14%

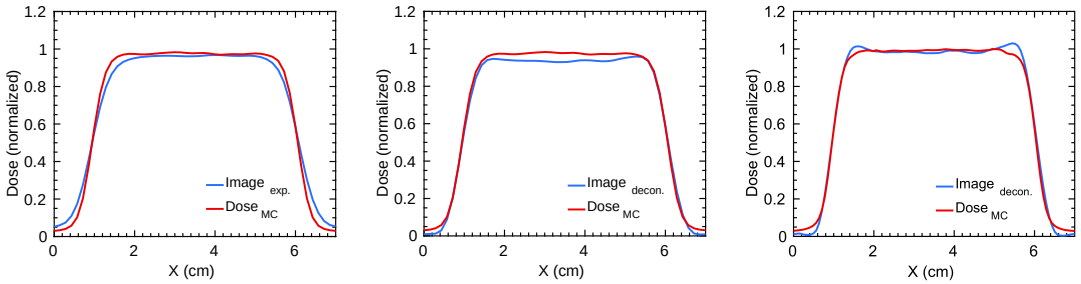

(a) (b) (c)

Figure 3.5: A comparison of cross-line profiles for a 6 MV 5x5 cm^2 open field with (a) zero, (b) one, and (c) two iterations of deconvolution by the CDSF. Also shown in figures is the cross-line profiles from the Monte Carlo calculated dose at 10 mm ($Dose_{MC}$).

and the reference dose profiles obtained by the Monte Carlo simulations. There is good agreement between two profiles in the plateau of the beam, but the penumbra region appears to have a larger discrepancy. The field size is still roughly the same because the profiles intersected around 50% of the maximum dose. Figure 3.6(b), (d), (f), and (h) show the dose profiles of the deconvolved Cerenkov images and the reference dose profiles. The penumbra region shows much better agreement in these figures over the raw images, but slight horns are present towards the edge of the plateau region.

Figure 3.7 shows the profiles of the raw and deconvolved Cerenkov images alongside the reference dose profiles at a 10 mm depth for the 5x5 cm^2 field size beam from 10

MV energy. The deconvolved profile displays the same reduction in the penumbra width seen from 6 MV beam energies but is over-corrected with respect to the dose profile.

Figure 3.8 shows the dose profiles of the raw and deconvolved images as well as the reference data for the 60° hard wedge. The figure exhibits behavior similar to Figure 3.6 with respect to the penumbra agreement. The deconvolved data matched the reference data better than the raw image, but the deconvolved image shows larger horns. The horns are beneficial for image-to-dose agreement, but it remains an artifact of the image processing step. Of note, the beam hardening effects on the energy spectrum were not considered for generation of the CDSF used in this image. The normal 6 MV CDSF was used for generation of the deconvolved cross-line profiles.

Figure 3.9 shows the cross-line profiles of the raw Cerenkov images and beam fluence from the 5x5 cm^2 field size for 6, 10, and 18 MV photon beams. The raw Cerenkov imaged profiles from the different beam energies display slight differences in the penumbra shape. Each beam energy exhibits a unique dose deposition curve and lateral scattering profile, which causes differences in the Cerenkov emissions from the phantom surface as shown in Figure 3.9(a). After deconvolution by the CSF corresponding to each energy, these profiles become much more homogeneous, as shown in Figure 3.9(b). In this case, the profiles represent the beam fluence, which is identical for a fixed field size.

Figure 3.10 shows the 2D isodose profiles and gamma analysis from open and MLC-shaped fields for deconvolved images and radiochromic film data. The gamma maps shown were evaluated with a 5%/3 mm criteria. The isodose distribution of the 3x3 cm^2 deconvolved field agreed well with the film-measured dose distribution (SNR = 22.13 for 3x3 cm^2 field). The horizontal isodose lines showed a slight misalignment, but vertical isodose lines were well matched. However, the deconvolved image of the 3x3 cm^2 field had a 91% pass rate for the 5%/3 mm criteria, but only a 52% pass rate under the 3%/3 mm criteria. This could possibly be improved with automatic registration of the image data with film data. As the field size decreased, the Cerenkov signal decreased. This decreasing SNR resulted in a qualitatively worse agreement of the deconvolved image with the film data for the 0.6x0.6 and 1x1 cm^2 fields when observing the isodose comparison (SNR = 3.17 and 17.84 for 0.6x0.6 and 1x1 cm^2 fields, respectively). However, the gamma analysis on the 0.6x0.6 and 1x1 cm^2 deconvolved fields both had a passing rate of >95% for dose points under the 3%/3 mm criteria. The

MLC-shaped field shows good agreement of the isodose lines in the horizontal direction, but slight misalignment of the isodose lines in the vertical direction. The isodose lines on the right and left sides of the field were near the edges of the optical phantom. The film data were taken with a phantom much larger than the maximum length of the field, which could account for the observed difference in the dose distributions. The MLC-shaped field had a 99% pass rate for data points using the 5%/3 mm criteria, but only a 79% pass rate under the 3%/3 mm criteria.

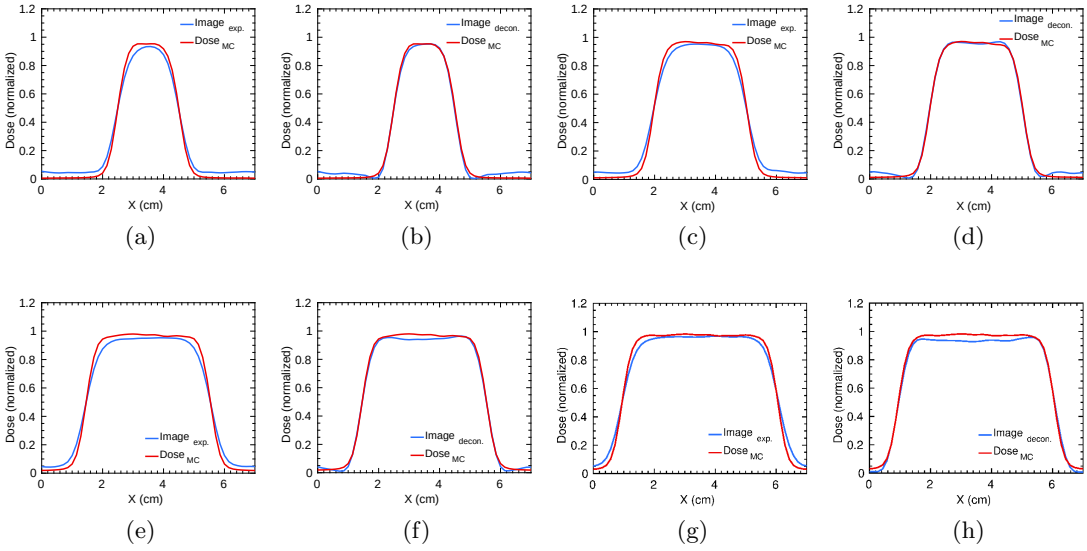

Figure 3.6: A comparison of the cross-line profiles between Monte Carlo dose ($Dose_{MC}$) at a 10 mm depth, raw Cerenkov images ($Image_{exp.}$), and deconvolved Cerenkov images ($Image_{decon.}$) for a 6 MV beam energy. Field sizes shown are (a-b) 2x2, (c-d) 3x3, (e-f) 4x4, and (g-h) 5x5 cm^2. Figures (a), (c), (e), and (g) show raw imaged profiles while (b), (d), (f), and (h) show image profiles deconvolved by the CDSF.

3.5 Discussion

Zhang et al. (2013) measured cross-line profiles of Cerenkov images of square fields using a water equivalent phantom [87]. Their results indicated an error of up to 5% in the penumbra regions of cross-line profiles. The deconvolution method with the CDSF improved both the field size and penumbra width for all images. The agreement of

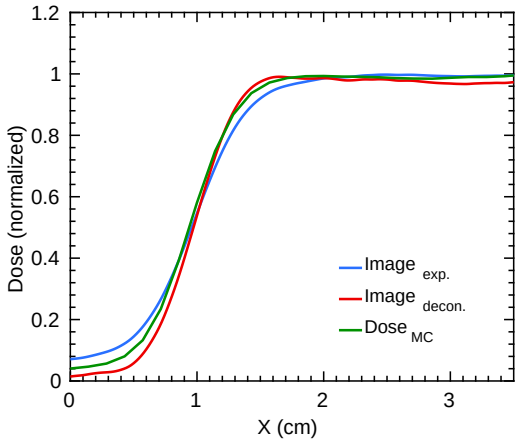

Figure 3.7: A comparison of the cross-line profiles between Monte Carlo dose ($Dose_{MC}$), raw Cerenkov image ($Image_{exp.}$), and deconvolved Cerenkov image ($Image_{decon.}$) for a 10 MV beam energy at a 5x5 cm^2 field size.

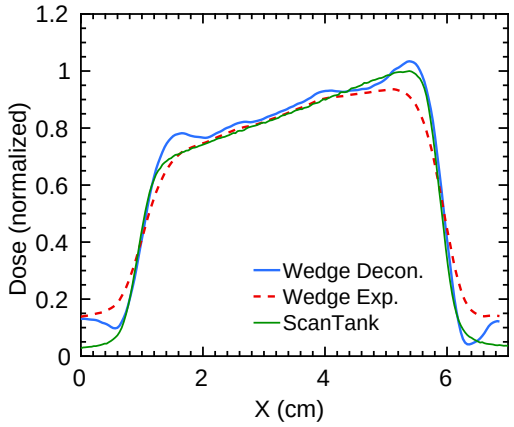

Figure 3.8: Cross-line profile comparison of Cerenkov images for the 60° hard wedged field with a 5x5 cm^2 field size. Profiles shown in this figure are image data deconvolved by the CDSF (Wedge Decon.), raw imaged data (Wedge Exp.), and reference dose data generated by a water scanning system (ScanTank) at a 10 mm depth.

the field flatness also improved after deconvolution. These improvements are achieved because the use of the CDSF pushed back some of the profile energy from regions of high gradient [95].

The Correlation Ratio (CR) was introduced by Zhang et al. for Cerenkov light dosimetry [55]. The CR represents the dose deposited per Cerenkov photon detected by

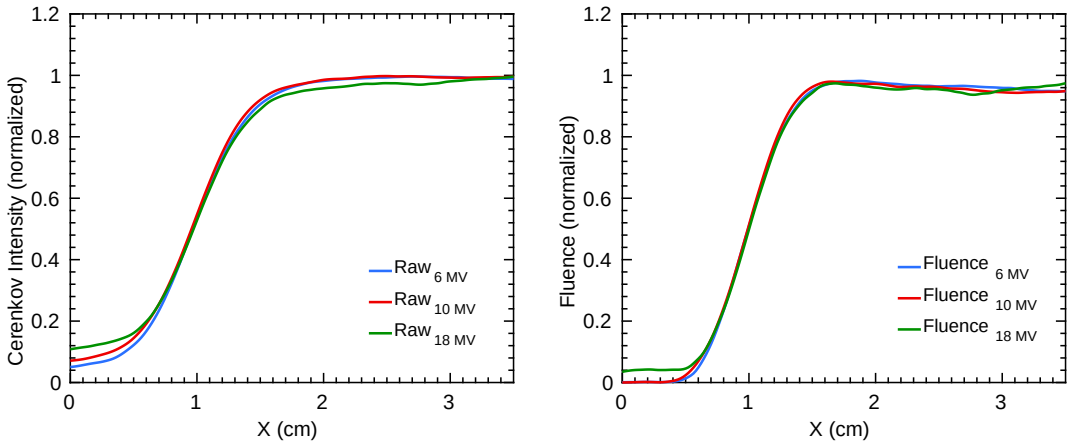

Figure 3.9: A comparison of the incident fluence cross-line profiles for 5x5 cm^2 open fields for three photon beam energies. (a) displays raw Cerenkov images (Raw) and (b) displays deconvolved Cerenkov images at the surface (Fluence). Cross-line profiles in (a) were deconvolved by the CSF corresponding to the given energy to find the fluence profiles shown in (b).

a pixel of the image sensor and enables absolute dosimetry if a photon counting camera is used in an imaging experiment. However, this function does not account for the diffusion of Cerenkov photons as they travel in the medium. Hence, a Cerenkov photon collected in an image pixel does not represent one spatial point of dose deposition in a medium. This compromises the usefulness of the CR as an indicator for dose deposition at a specific voxel in the medium. On the other hand, the CDSF can account for both the spread of Cerenkov photons and dose deposition. Consequently, use of the CDSF leads to better agreement between the measured data and the reference data for various fields. In particular, this method worked well to improve the agreement of regions with high dose variation. In these regions, the diffusion of Cerenkov photons can have a significant effect on the measured dose distribution of the field. I recommend using the CDSF instead of the CR for Cerenkov light dosimetry, however, further studies are needed to prove the validity of the deconvolution formulation in heterogeneous media before this conclusion can be made certain.

The iterative decovolution algorithm was used to solve the convolution equations.

It is typical of conventional deconvolution methods to use many iterations of deconvolution in image processing, therefore, the effects of more than one iteration were tested to see if it would improve the outcome of our result. Although multiple iterations do not hold any physical significance, they are none-the-less relevant to this study. Two or more iterations for the deconvolution created horns at the edge of the field. The horns became more prominent after multiple deconvolution iterations. Future studies may consider applying smoothing to the horn artifacts created as a result of deconvolution. In contrast, a single iteration did not significantly compromise the beam profile and improved the beam flatness. Overall, one deconvolution iteration gave the best agreement of the beam profiles with the reference data. It is suspected that increasing the number of deconvolution iterations beyond one may uncouple the physical significance of the convolution formulation because all kernels in the model represent physical parameters.

For the deconvolution method, neither the beam divergence nor oblique incident beam angles, i.e. non-zero θ_{in}, were considered. Even if the beam is directed normal to the phantom surface, photons at off-axis locations do not intersect the phantom normal to the surface due to divergence. Additionally, as θ_{in} increases, the shape of the CSF changes due to the directionality of the beam. This would mean that the CSF function depends on the beam angle and, consequently, is not space-invariant. The same limitations apply to DSF and CDSF. Hence, the Fourier transform method becomes more complicated than what was demonstrated in this study. To simplify the calculation, the beam was approximated to have no divergence which limited the analyses to $\theta_{in} = 0$. Expanding our formulation to include beam divergence and oblique incident beam angles will be crucial to improve the accuracy when this method is used under a clinical setting.

In addition to expanding our formulation to account for beam divergence, the heterogeneities and curvatures that exist within clinical settings are also being considered. All these factors may be corrected for using a space-variant deconvolution method. Regions of uniform curvature, beam divergence, or a combination thereof within an image may be deconvolved by a corresponding CDSF, and then patched together with the rest of the image [96]. This operation has been studied in the case of camera or image blur correction using a spatially-variant PSF [96, 97, 98, 99]. This method may have limitations

in terms of the number of patches used in the image, or other image processing considerations which are unknown to the authors as yet. It may also be possible to employ more advanced spatially-variant deconvolution methods that rely on the assumption of a smoothly varying PSF [98]. In addition, this study considered a MV photon beam to measure time-integrated cumulative dose. The extension of the presented theory to electron beams and time-dependent or dynamic dosimetry is straightforward but must also be tested.

This study assumed $\theta_{obs} = 45°$. Previously, we found that Cerenkov photon intensity depends on θ_{obs} from the results of Monte Carlo simulations. This effect was modeled by introducing the Directional Radiance Distribution Function (DRDF) [88]. Notably, this effect does not change our results because cross-line profiles were normalized and all data were taken at a single θ_{obs}. However, the DRDF must be taken into account for relative dose measurements on a curved surface or large field and any absolute dose measurements.

While our imaging experiments were performed for relative dose measurements, the new method can be easily applied for absolute dosimetry by obtaining appropriate calibration data. Such data would allow us to relate deconvolved Cerenkov image intensity to dose directly. This option will be explored in future studies. Although a photon counting camera would also allow for absolute measurements of dose, this method could be strongly affected by stray radiation noise, making this approach more difficult to implement for practical uses than a calibration method.

The primary focus of this study was on estimating the dose at a depth of $d_0 = 10$ mm using the DSF of this depth. However, the true significance of the proposed method is in the relationship between measured Cerenkov photons and the incident beam fluence as represented by Equation (3.5). The beam fluence is often measured for IMRT QA by an instrument with a 2D detector array. Our method enables us to easily obtain the beam fluence from the Cerenkov image data, but it does not yet match the speed and accessibility of using a 2D detector array. Furthermore, using the beam fluence and the standard dose calculation algorithm, this technique can be used to relate the Cerenkov photon image to the dose at any depth for superficial dosimetry.

3.6 Conclusions

This chapter introduced a deconvolution method for Cerenkov light dosimetry. The planar dose distribution at a depth of 10-mm in a medium was calculated by deconvolving the measured Cerenkov photon image with the Cerenkov Dose Scatter Function (CDSF). The new technique was evaluated by comparing the measured dose distributions with reference dose distributions. These tests used open square fields, a hard-wedged field, and a MLC-defined irregularly-shaped field, while varying dose rate, beam energy, and field size. The cross-line dose profiles obtained by the deconvolution method showed better agreement with the reference data than the raw Cerenkov images. Notably, the new method improved the agreement greatly in the penumbra region. Comparison of 2D isodose lines also showed good agreement for the 3x3 cm^2 field size and MLC shaped field. Fields smaller than 3.0x3.0 cm^2 field size showed a larger discrepancy due to lower SNR.

The proposed deconvolution method improved the accuracy of Cerenkov light dosimetry when it was used to estimate the dose distribution in the area of steep dose gradients. It provided a more accurate representation of dose from Cerenkov photon images as compared to previous methods, such as the Correlation Ratio. The deconvolution method was validated for beam profile measurements in homogeneous media, which serves as an initial step in development for possible use as an in vivo dosimetry technique during EBRT. It is noted that the capability of estimating the incident beam fluence with the new method can be adopted to the measurement of the dose distribution at any depth in the superficial region by Cerenkov light dosimetry.

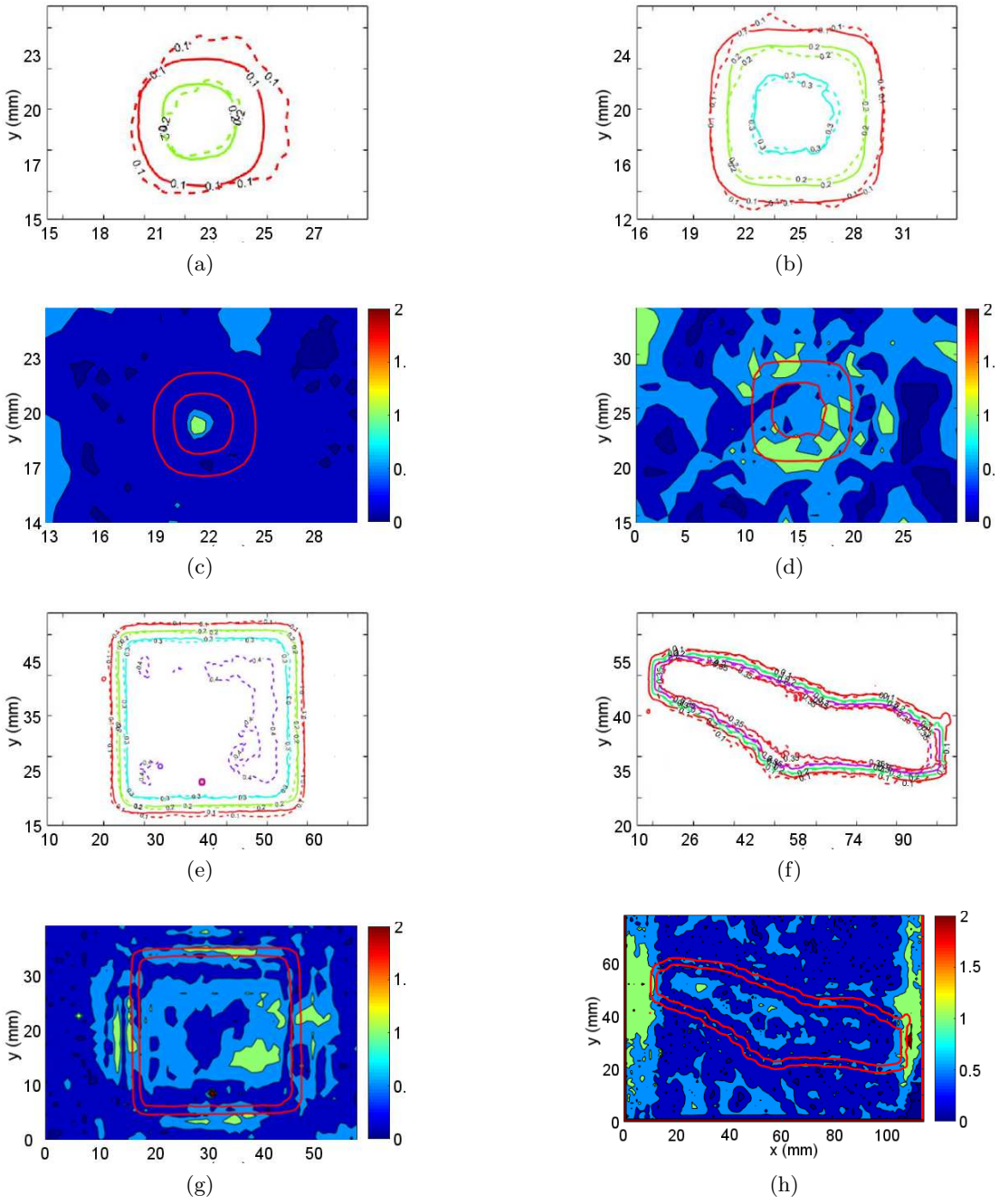

Figure 3.10: Dose distributions and gamma index maps for comparison of Cerenkov images deconvolved by the CDSF and radichromic film for 6 MV small fields. Field sizes shown are (a, c) 0.6x0.6 cm^2, (b, d) 1x1 cm^2, (e, g) 3x3 cm^2, and (f, h) a MLC shaped field. The gamma maps shown were analyzed with a 5%/3 mm criteria.

Chapter 4

Characterization of the Cerenkov Scatter Function

This chapter is largely derived from: E. E. Brost and Y. Watanabe, "Characterization of the Cerenkov scatter function: a convolution kernel for Cerenkov light dosimetry." Journal of Biomedical Optics 23(10): 105007 (2018).

4.1 Introduction

Radiation treatment beams produce electrons which are responsible for dose deposition in a medium. Above a certain energy threshold, these charged particles will travel faster than the phase velocity of light within the medium, and emit Cerenkov photons as visible light along their path of travel [19]. There is currently much interest in using Cerenkov photons during EBRT as a means to estimate the dose delivered by the treatment in 2D and in real-time [55, 56, 4]. However, a better understanding of the complex relationship between Cerenkov photon emission and dose deposition is needed to improve the dose prediction accuracy of this method[55]. The light-to-dose relationship was previously approached as a deconvolution problem [100]. Cerenkov photons are emitted in locations corresponding to dose deposition, hence, deconvolution by a light-transfer function can be used to isolate the regions of dose.

In the previous chapter, the mathematical relationship between Cerenkov photons imaged during EBRT and dose deposition was shown[100], but this did not include a

full characterization of the CSF. The mathematical relationship assumed radiation beam angles normal to the irradiated medium surface and space-invariant transfer functions (i.e. the CSF and DSF). Expansion of this formulation to clinically relevant geometries will go beyond these assumptions, so the relative effects of non-normal beam angles and space-variant CSFs must be investigated. In this chapter, the dependence of the CSF on common beam parameters such as photon energy, incident beam angle, and the type of medium will be examined through Monte Carlo simulation. In addition, the errors introduced into the dose distribution obtained by the deconvolution formulation will be examined through perturbation of the amplitude and shape of the CSF and the incident beam angle. This will allow us to determine the sensitivity of the deconvolution formulation to those physical parameters.

4.2 Materials and Methods

4.2.1 Monte Carlo simulations

GAMOS (version 4.0.0), a Geant4 (version 10.02) based Monte Carlo toolkit for medically-oriented applications, was used to create simulations to generate the CSFs [3]. The Tissue Optical Modeling plugin was used with GAMOS to more accurately simulate the optical physics and handle optical properties [18]. Two simulation studies were done to investigate the dependence of the CSF on various model parameters. The purpose of study (i) was to examine how the CSF changed as a function of incident beam angle. Study (ii) was used to generate CSF fit coefficients for normal beam angles at common treatment energies. Study (ii) utilized the photon energy spectra of 6 MV, 10 MV, and 18 MV beams for a TrueBeam linear accelerator (Varian Medical Systems, Palo Alto, CA) [91]. Table 4.1 details the beam and model parameters used in each study. The "GmEMPhysics" model was used in all simulations, the step sizes and range cuts for all particles were kept at default in each region, the general photon production threshold was between 0 eV to 1 GeV, and the maximum number of Cerenkov photons per step was kept as unlimited.

All CSF simulations involved a pencil beam of radiation incident on a smooth-surfaced, voxelized solid phantom. Each simulation included a geometry file that provided the physical model and optical properties of the phantom. The phantom, a box of

20x20 cm^2 area and 10 cm depth, was placed inside of an empty air volume composed of a 100x100x100 cm^3 box. In each simulation, the Cerenkov photons of wavelengths from 400-800 nm that escaped the medium surface were scored and the initial position, initial direction, final position, final direction, and wavelength were recorded. In addition, the number of photon interactions (scattering or absorption) occurring before the Cerenkov photon escaped were also recorded. Taking a histogram of the initial depth of emission (Z_i-position) allowed for the determination of the sampling depth for each medium [55]. The detection sensitivity was found as the logarithm of the normalized Z_i histogram, and the sampling depth was determined as the depth from which 63% (1-1/e) of the photons originate. CSF simulations were run with 8×10^8 histories in order to minimize statistical uncertainties.

For the perturbation analysis, two additional simulations were performed separately from studies (i) and (ii). The first simulation was for scoring of the DSF in the voxelized phantom. The dose delivered to the solid phantom by an incident pencil beam with the same photon energy spectra as those used in study (ii) was scored in voxels of 0.2x0.2x2.0 mm^3. The DSF function was then calculated as the dose delivered to a plane at the depth of $d_0 = 10$ mm.

The second simulation was done to obtain the dose delivered to a plane at the depth of $d_0 = 10$ mm for a 6 MV photon beam with a field size of 5x5 cm^2. This simulation utilized the 6 MV phase space data of a TrueBeam linac in order to match the experimental results. The phase space data was obtained from the Varian. Dose simulations were run with 1×10^{10} histories to keep the dose uncertainty at <1%.

Table 4.1: The simulation parameters for Monte Carlo studies (i) and (ii). These studies varied the beam angle, energy, and irradiated medium to measure the relative effects on the CSF. Beam energies used were either monoenergetic (mono.) or polyenergetic (poly.). Phantom models used were the optical phantom (OP), light skin (LS), medium skin (MS), and dark skin (DS) models.

Study	Photon energy	Medium	θ_{in}	Field size
(i)	6 MV mono.	LS, OP	0-70°	pencil
(ii)	6, 10, and 18 MV poly.	LS, MS, DS, OP	0°	pencil

4.2.2 Simulated material properties

Four different materials were used throughout simulations: light, medium, dark-pigmented stratified human skin, and a homogeneous optical phantom. The homogeneous optical phantom was created in simulations based upon a real phantom used in the imaging experiments. The optical phantom was purchased from INO (Ontario, Canada). The optical properties of this phantom were generated from the factory tested coefficients provided by the company [89, 90]. The absorption and reduced Mie scattering coefficients had values of μ_a = 0.3-0.0002 $\times$ (λ-450) cm^{-1} and μ_s' = 114.0 cm^{-1}, respectively. The index of refraction of the optical phantom was n = 1.40 for wavelengths from 400-800 nm.

The optical properties of the stratified human skin models were generated from the descriptions and equations given by Meglinski (2002) [101]. The absorption properties of the human skin models were found as a linear combination of the individual tissue components: oxygenated hemoglobin, deoxygenated hemoglobin, water, and percent melanin content in each individual skin layer. The reduced Mie scattering coefficients used for the skin layer models were generated based on equations given by Jacques (2013) and Bhandari, *et al.* (2011) [102, 103]. Table 4.2 presents the thickness of the skin layers and the index of refraction values used in simulations. Table 4.3 details the atomic composition of elements used to create both the skin and optical phantoms, based upon the National Institute of Standards and Technology soft tissue and polyurethane resin models found in the GAMOS library. Figure 4.1 shows the absorption and scattering coefficients of each skin layer within the tissue models alongside the coefficients of the optical phantom.

4.2.3 Scoring and Fitting of CSFs

CSFs were generated by the binning and scoring of all surface-escaped Cerenkov photons in studies (i) and (ii). An 8x8 cm^2, 350x350 bin grid was used to create a histogram of the Cerenkov photon flux on the simulated medium surface. To model the CSF for 0° incident beams, the histogram was sampled along a line from r =-20-20 cm using spoke-sampling centered at the origin of the pencil beam on the medium surface. The

Table 4.2: The thickness, and refractive index of individual skin layers used in the stratified skin model.

Skin layer	Name	Thickness (mm)	Index of refraction
Epidermis	Stratum corneum	0.02	1.50
	Living epidermis	0.08	1.34
Dermis	Papillary dermis	0.15	1.40
	Upper net dermis	0.08	1.39
	Reticular dermis	1.50	1.40
Subcutaneous	Deep net dermis	0.10	1.38
	Subfat	6.0	1.44

Table 4.3: The atomic composition of the stratified skin model and optical phantoms.

Optical phantom $\rho = 1.04$ (g/cm^3)		Stratified skin $\rho = 1.06$ (g/cm^3)	
Element	Percent	Element	Percent
H	0.074	H	0.102
C	0.467	C	0.143
N	0.0156	N	0.034
O	0.3352	O	0.708
Mg	0.0688	Na	0.002
Al	0.014	P	0.003
Cl	0.0024	S	0.003
B	0.0226	Cl	0.002
		K	0.003

sampling angle, θ_s, was defined on the medium surface as the rotation from the +Y-axis about the Z-axis. A diagram illustrating the spoke-sampling schema can be seen in Figure 4.2(a). The CSF was sampled at the angles of θ_s =0-179° with 1° increments. The mean of all samples was fitted using a triple-Gaussian distribution with Equation (4.1):

$$CSF_{mean}(A, B, C, D, E, F, r) = Ae^{-\frac{(r)^2}{B^2}} + Ce^{-\frac{(r)^2}{D^2}} + Ee^{-\frac{(r)^2}{F^2}} \tag{4.1}$$

where CSF_{mean} is the average of the CSF cross-sections over θ_s. Parameters A, B, C, D, E, and F are the fit coefficients, and r is the radial distance from the entrance point

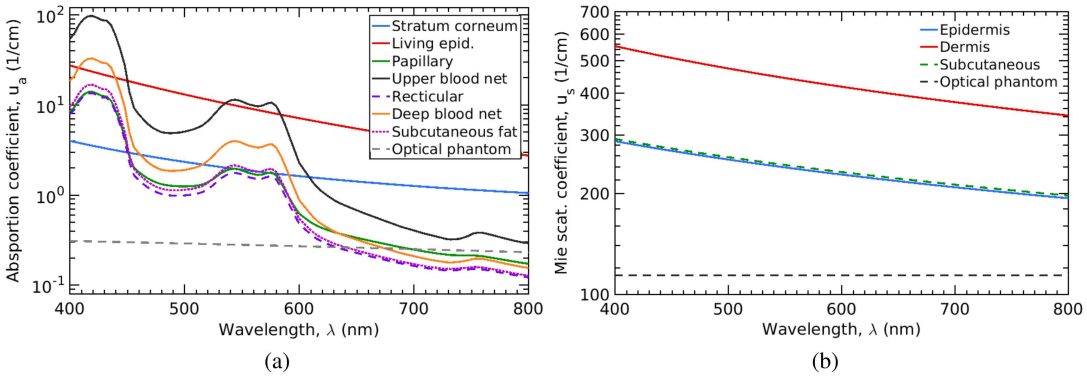

Figure 4.1: The (a) absorption and (b) Mie scattering coefficients of the light stratified skin model and optical phantom. For the medium and dark skin models, the living epidermis has more absorption due to a higher melanin content but other coefficients remain the same.

of the pencil beam on the medium surface. The error in CSF_{mean} was found as the standard deviation at each radial point from the CSF cross-sections. The large number of Monte Carlo histories ensured that the error at each point on CSF_{mean} was <1% of the maximum value for each CSF. The fitting was performed on CSF_{mean} in Matlab (Mathworks) using the $fitnlm$ function. This function also provides the standard error in the individual fit coefficients. A single and double-Gaussian, with and without central offset terms, in addition to a Cauchy-Lorentz distribution were also tested; however, a triple-Gaussian without offset yielded the best fit overall. An example of a fit can be seen in Figure 4.2(b). The coefficients A, C, and E were scaled based upon the number of primary particles used to generate the CSFs. The amplitude and full-width at half-maximum (FWHM) were found for each normally incident CSF.

4.2.4 Imaging experiments

An imaging experiment was performed to measure a 5x5 cm^2 Cerenkov photon image on the optical phantom. Cerenkov images were captured using a Canon EOS 5D commercial camera equipped with CMOS sensors and a F-number 1.4 lens (Canon USA, Huntington, NY). The optical phantom mentioned in Section 4.2.2 was used in the experiment. Photos and a diagram of the experimental setup can be seen in Figure

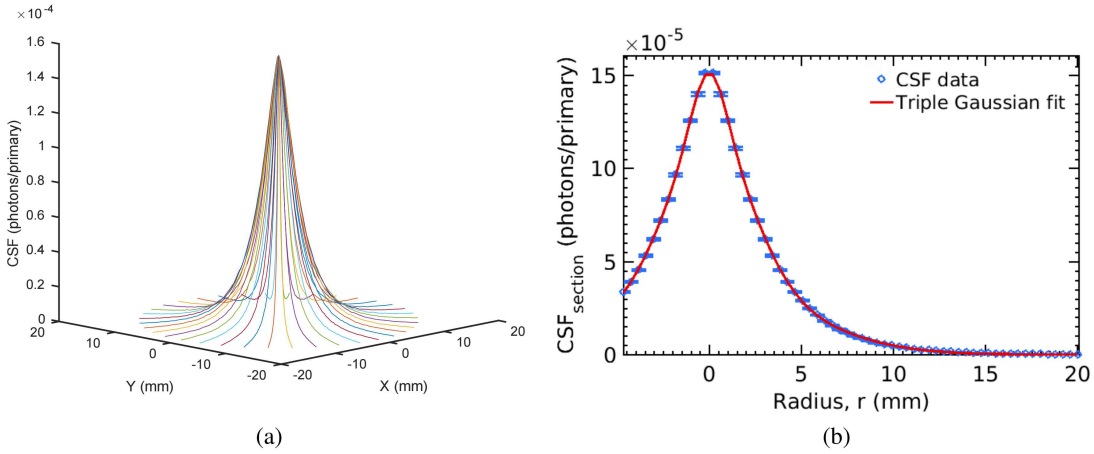

Figure 4.2: Visualzation of the (a) spoke sampling and (b) fitting of the CSF for a 6 MV polyenergetic beam incident on a optical phantom model. Error bars shown on the CSF in (b) are all <1% of the maximum value.

3.3. The optical phantom was mounted to the gantry head of a TrueBeam linear accelerator. The mount kept the imaged surface of the optical phantom normal to the radiation beam at all times. The optical phantom surface was placed at 100 cm source-to-surface distance. The camera was placed at a distance of 100 cm from the optical phantom surface and the imaging angle was $\theta_{obs} = 45°$. The camera was controlled using the default commercial software, EOS Utility (Canon USA), which allowed for remote shooting through a USB cable on a laptop computer placed at the linac control console. A custom camera mount was used to place a 45° mirror between the camera and the phantom. This was used to reduce stray radiation in the projection area of the CMOS detector and enabled us to place the camera behind lead shielding. The room was darkened as much as possible to reduce stray ambient photons to the camera.

Individual Cerenkov images were taken with an exposure time of 1/6" at 1000000 ISO. The beam parameters used on the linac were a 6 MV beam energy with a 600 MU/min dose rate and 5x5 cm^2 field size. Each Cerenkov image was processed using both temporal and spatial filtering. Ten images were used to create a composite average image. This image was spatially filtered using a 15-pixel mean filter. The image was then perspective corrected, as described in previous Cerenkov imaging studies [100, 88, 87]. No spectral correction was applied to the Cerenkov images based upon the quantum

efficiency of the camera as this study utilizes relative dosimetry.

4.2.5 Perturbation analysis

Perturbation analysis was done to measure the effects of changing the amplitude and shape of the CSF and the incident beam angle on the fluence and dose images. It was performed using the Cerenkov photon image of the 6 MV photon beam with a 5x5 cm^2 field size taken with the optical phantom, as discussed in Section 4.2.4. The CSF distribution of the optical phantom with a 6 MV photon beam, as described in section 4.2.1 was used for the perturbation analysis. The triple-Gaussian function representing the CSF was remapped to create a radially symmetric distribution. Remapping was done through the creation of a square matrix, with the same size and dimensions as the experimental Cerenkov photon image, with individual elements representing an increasing radial distance from the center of the matrix. The CDSF was also obtained following Equation (3.6) with the DSF calculated from section 4.2.1.

The CSF and CDSF were used to deconvolve the 5x5 cm^2 Cerenkov photon image to obtain the beam fluence on the surface of the medium and the dose image at a 10-mm depth by Eqns. (3.4) and (3.7). Initial fluence and dose images were first obtained using an unaltered CSF shape. These images served as references which could be compared against fluence and dose images obtained after scaling the amplitude and shape of the CSF. Scaled CSFs were generated by scaling the triple-Gaussian fit coefficients. Scaling the Gaussian amplitude coefficients A, C, and E by a single value allowed for modification of the total CSF-amplitude. Scaling the Gaussian width coefficients B, D, and F by a single value allowed for modification of the total CSF-FWHM. The scaled CSFs, either in their FWHM or amplitude, were used to again solve for the beam fluence and dose. The scaled beam fluence and dose images were compared with the unscaled fluence and dose using the mean-squared error (MSE) and the error of the penumbra width. The MSE of images was calculated using the *immse* function in Matlab, found as:

$$MSE = \frac{1}{N\, I_{max}} \sum_{n=1}^{N} [I_{scaled}(n) - I_{unscaled}(n)]^2 \tag{4.2}$$

where n is the index of individual image pixels, N is the total number of image pixels,

I_{scaled} is the scaled image, $I_{unscaled}$ is the unscaled image, and I_{max} is the maximum value of $I_{unscaled}$ for normalization. The error in the penumbra width was found as:

$$Err_{pen} = \frac{Pen_{scaled\,CSF} - Pen_{unscaled\,CSF}}{Pen_{unscaled\,CSF}} \tag{4.3}$$

where Pen is the measured penumbra in mm from the I_{scaled} and $I_{unscaled}$. The penumbra width was measured as the distance between the 80% and 20% of the maximum value points, taken from a cross-line profile of the image. Penumbra measurements were found using cross-line profiles taken from the center of each image, found as the mean profile of both the horizontal and vertical directions. The scaled images of dose (as calculated using the CDSF) were also compared with the Monte Carlo calculation as described in section 4.2.1.

The resulting MSEs and penumbra errors were used to evaluate the global error introduced in the deconvolution step when using an "incorrect" CSF. The error due to the CSF-amplitude was calculated by the MSE. The error due to the CSF-FWHM was calculated by the penumbra error. The global error was found as the quadrature of these two errors, given by Equation (4.4):

$$Err_{global} = \sqrt{Err_{pen}^2 + MSE^2}. \tag{4.4}$$

Perturbation analysis was also performed using the non-normal CSFs (θ_{in} >0°) obtained from study (i). The beam fluence was calculated using the normal monoenergetic CSF (θ_{in} =0°) and compared with the beam fluence calculated with deconvolution by non-normal CSFs using gamma analysis. Gamma analysis is a method commonly used for comparison of two fluence or dose distributions, one a reference and the other a query for testing. 2D gamma analysis was performed using the definition for γ given by Low, et al. [104, 105] The gamma passing rate between images was calculated in Matlab with custom-written software using four criteria: dose difference/distance-to-agreement (DTA) = 3%/0 mm, 3%/1 mm, 3%/2 mm, and 3%/3 mm.

4.3 Results

4.3.1 Dependence of the CSF on beam parameters

Line profiles of the CSF for a 6 MV polyenergetic photon beam incident on the skin models, as generated by study (ii), can be seen in Figure 4.3. As the skin-melanin content increases, the CSF-amplitude decreases.

Figure 4.4 shows the CSF profiles of the 6 MV monoenergetic photon beam as observed on the optical phantom surface, generated by study (i). The figure also shows the effects of changing the incident beam angle θ_{in} on the shape of the CSF. As the incident angle increases, the CSF becomes elongated in the direction of the beam path. In addition, the peak position of the CSF becomes displaced from the photon beam entrance point. The trend in the displacement was fit and follows the equation $s = 0.62\ tan(\theta_{in})$, where s is the displacement in the direction of the beam path in mm.

4.3.2 Dependence of the CSF on medium properties

The coefficients of the CSF for light, medium, dark skin, and optical phantom materials are listed in Table 4.4. These coefficients can be used to generate radially-symmetric CSFs for 0° incident photon beams of the listed model and beam energy. The goodness-fit, R^2, was greater than 0.99 for all cases and individual coefficient errors were between 1.46-3.90%, indicating a good parameter fitting of the CSF using Equation (4.1).

Table 4.5 shows the amplitude and width of the CSFs of the stratified skin models and optical phantom for θ_{in} =0° and 6, 10, and 18 MV energies. As expected, the CSF-amplitude for a given energy decreases as melanin content increases due to the increased absorption. As beam energy increases, the CSF-amplitude increases due to more dose deposition per primary particle. Additionally, the CSF-FWHM marginally increases with beam energy. However, no particular trend exists in the CSF-FWHM when comparing different skin models at a single energy. The only difference that exists between the skin models is the percent melanin content in the living epidermis. Scattering and absorption of optical photons occurs identically in all other layers of the skin models. Cerenkov photons diffuse in a similar manner when traveling in layers below the living epidermis, but with differing levels of absorption between the skin models for Cerenkov photons exiting the tissue. This results in a similar CSF-FWHM

for all skin models at a single energy. The CSF-amplitude of the optical phantom was overall greater than that of the skin model. In addition, the CSFs of the optical phantom exhibited more lateral spread than that of any stratified skin models. Both of these results were due to the lower absorption coefficients seen in the optical phantom, allowing for more photons to exit from the phantom and further from the entrance point of the pencil beam.

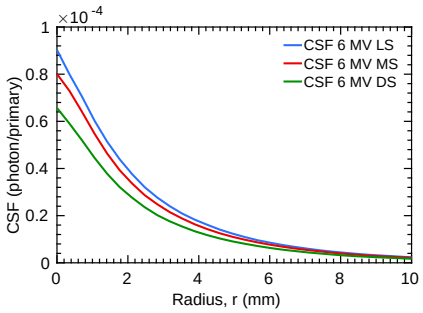

Figure 4.3: A profile of the CSFs of light (LS), medium (MS), and dark (DS) skin-layer models at a 6 MV polyenergetic beam energy.

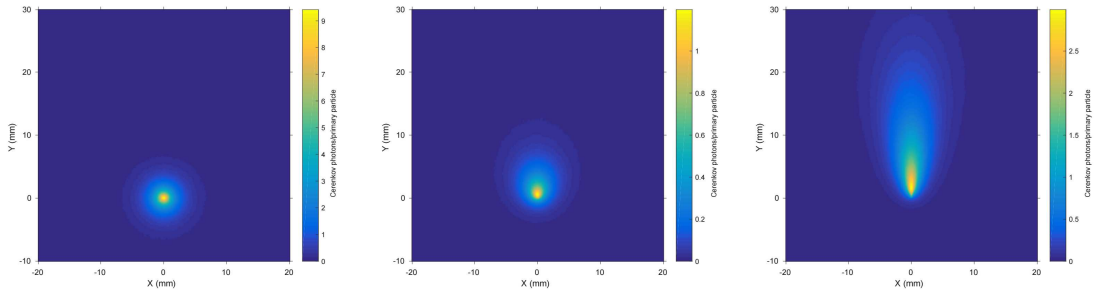

(a) (b) (c)

Figure 4.4: CSFs of a 6 MV monoenegetic photon pencil beam incident on a stratified light skin model with beam angles: (a) θ_{in} =0°, (b) θ_{in} =35°, and (c) θ_{in} =70°.

Figure 4.5 shows the spectra, number of photon interactions, and detection sensitivity of surface-escaped Cerenkov photons. Figure 4.5(a-c) shows the results for the light, medium, and dark stratified skin models. The light skin shows higher counts of photons at the wavelength of 500 nm and above 600 nm than darker skin types. This is due to lower absorption of photons in this wavelength range due to decreased melanin

Table 4.4: The coefficients of the CSF for the optical phantom (OP), light skin (LS), medium skin (MS), and dark skin (DS) models for polyenergetic photon beams of TrueBeam linac for θ_{in} =0°. The coefficient errors shown at the bottom represent the range of the individual standard errors for each column.

	A (phot./prim.)	B (mm)	C (phot./prim.)	D (mm)	E (phot./prim.)	F (mm)
6 MV - OP	3.85e-5	1.34	7.75e-5	3.28	3.52e-5	7.11
6 MV - LS	3.53e-5	0.58	3.92e-5	1.52	1.55e-5	3.76
6 MV - MS	3.48e-5	0.57	3.75e-5	1.52	1.43e-5	3.79
6 MV - DS	3.01e-5	0.58	3.38e-5	1.50	1.35e-5	3.74
10 MV - OP	4.55e-5	1.38	8.81e-5	3.45	4.05e-5	7.46
10 MV - LS	3.78e-5	0.58	4.23e-5	1.55	1.71e-5	3.90
10 MV - MS	3.73e-5	0.62	3.86e-5	1.60	1.55e-5	3.95
10 MV - DS	3.63e-5	0.64	3.37e-5	1.68	1.29e-5	4.06
18 MV - OP	4.64e-5	1.40	9.22e-5	3.51	4.24e-5	7.61
18 MV - LS†	5.94e-5	0.82	3.69e-5	2.88	-	-
18 MV - MS†	5.66e-5	0.82	3.46e-5	2.88	-	-
18 MV - DS†	5.14e-5	0.82	3.15e-5	2.89	-	-
Coeff. error	1.46-3.78%	1.01-2.26%	1.32-2.95%	1.27-1.85%	2.85-3.90%	1.17-1.39%

Table 4.5: The amplitude, FWHM, and the sampling depth of the CSF for the optical phantom (OP), light skin (LS), medium skin (MS), and dark skin (DS) models for 6, 10, and 18 MV polyenergetic beams. † The third Gaussian term has an amplitude statistically consistent with zero, a double Gaussian is sufficient for modeling the 18 MV skin distributions.

	Amplitude (phot./prim.)	FWHM (mm)	Sampling depth (mm)
6 MV - OP	1.54e-4	5.01	5.26
6 MV - LS	1.01e-4	1.69	3.11
6 MV - MS	9.53e-5	1.67	3.13
6 MV - DS	8.58e-5	1.69	3.16
10 MV - OP	1.79e-4	5.22	5.77
10 MV - LS	1.08e-4	1.65	3.35
10 MV - MS	1.02e-4	1.64	3.36
10 MV - DS	9.34e-5	1.62	3.40
18 MV - OP	1.86e-4	5.33	6.02
18 MV - LS	1.11e-4	1.64	3.46
18 MV - MS	1.04e-4	1.64	3.48
18 MV - DS	9.39e-5	1.67	3.52

content. The number of photon interactions before escaping the medium showed a similar trend for all skin types. The detection sensitivity trend was also similar for all skin types. Figure 4.5(d-f) shows the results of the optical phantom for 6, 10, and 18 MV polyenergetic beams. The trend of energy spectra and the number of interactions for all three energies is similar, with 18 MV displaying the highest counts among the three energies. The detection sensitivity changes with energy due to the difference in primary photon attenuation among the different energies.

Table 4.5 also presents the sampling depth for each energy in the different materials. At each energy, the sampling depth increases with the skin-melanin content. This result agrees with what was shown by Zhang, *et al.* (2014), for the sampling depth of electron beams on a similar skin model [87]. The sampling depth also increases with the beam energy. This can be explained by the presence of a larger build-up region for higher energy photon beams.

4.3.3 Effect of perturbation of the CSF on deconvolved fluence and dose

Figure 4.6 shows the experimental Cerenkov image and beam fluence line profiles for various CSF-FWHM. Figure 4.6(a) displays the experimental Cerenkov image taken with a 5x5 cm^2 6 MV beam incident on the optical phantom. Figure 4.6(b) shows the Cerenkov photon image given in 4.6(a) deconvolved with the CSF for θ_{in} =70° of the optical phantom. Here, the effect of using an incorrect CSF for the deconvolution is shown. The Cerenkov image was taken with a uniform, unmodulated field, therefore, a uniform fluence image is expected. But deconvolution with the CSF of θ_{in} =70° yields a gradient fluence due to the elongation of the CSF. Figure 4.6(c) shows the CSF using the triple-Gaussian formula for the 6 MV polyenergetic photon beam with the optical phantom. This figure also shows the change in the CSF shape as the FWHM was scaled by multiplying the fit coefficients B, D, and F with the same value. Figure 4.6(d) shows the effect of scaling the CSF-FWHM on the crossline profile of the beam fluence. Here, it is observed that a wider CSF (1.3 × FWHM) pushes the penumbra region towards the center of the beam. A narrower CSF (0.7 × FWHM) results in a steeper penumbra region. This figure shows the impact of the CSF shape on the deconvolution process.

Figure 4.7 shows the results of the perturbation analysis with varying CSF-FWHM,

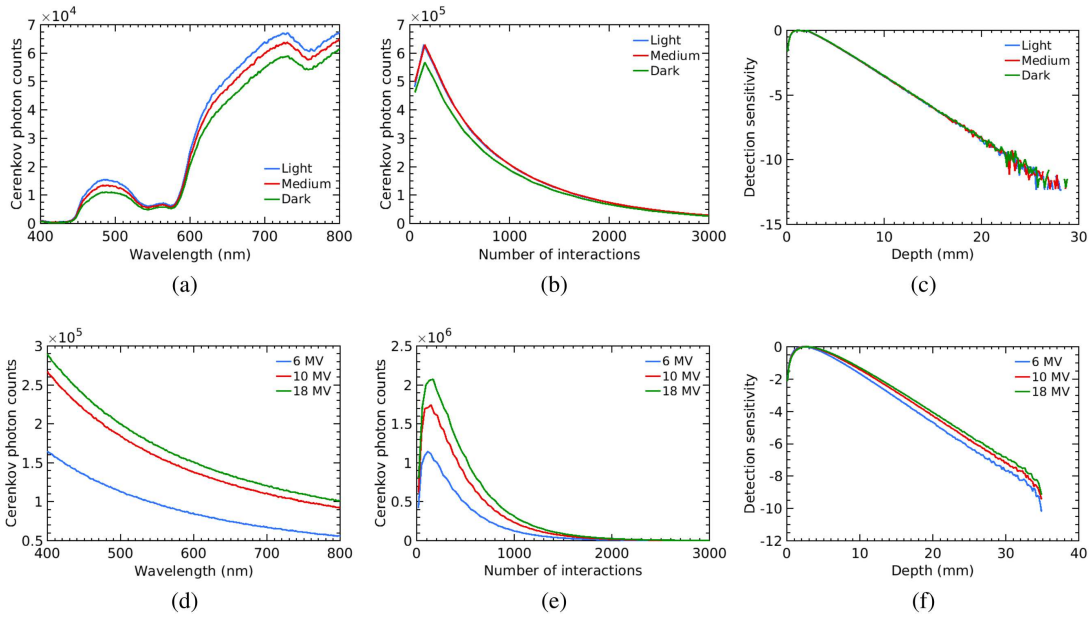

Figure 4.5: Cerenkov photon physical statistics from study (ii) for the optical phantom and stratified skin models. (a) and (d) show the spectrum of Cerenkov photons emitted from the surface. (b) and (e) show the number of photon interactions (scattering and absorption) occurring before the Cerenkov photons escape the material surface. (c) and (f) show the detection sensitivity of the escaped Cerenkov photons. (a-c) are taken from the stratified skin models and show results from light, medium, and dark skin types for a 6 MV polyenergetic beam. (d-f) are taken from the optical phantom and show results from 6, 10, and 18 MV polyenergetic beams.

CSF-amplitude, and the beam incident angle. For Figures 4.7(a-d), the CSF-FWHM and CSF-amplitude were varied relative to the CSF of the 6 MV photon beam with the optical phantom. Figures 4.7(a-b) and (d-e) used the 5x5 cm^2 6 MV optical phantom fluence image as the reference for calculations, i.e. Figure 4.6(a) deconvolved by the 6 MV CSF of the optical phantom. Figure 4.7(c) used the Monte Carlo calculated dose at a depth of 10 mm as the reference image.

Figure 4.7(a) shows the MSE when modifying the CSF-FWHM. For relative CSF-FWHM values <0.5, the CSF becomes more like a δ-function, therefore the MSE shows less variability in this region. The MSE in the deconvolved image increases exponentially for relative CSF-FWHM values >1. Figure 4.7(b) shows the penumbra error, Err_{pen}, and displays a similar trend to that shown in Figure 4.7(a), but also shows an unexpected

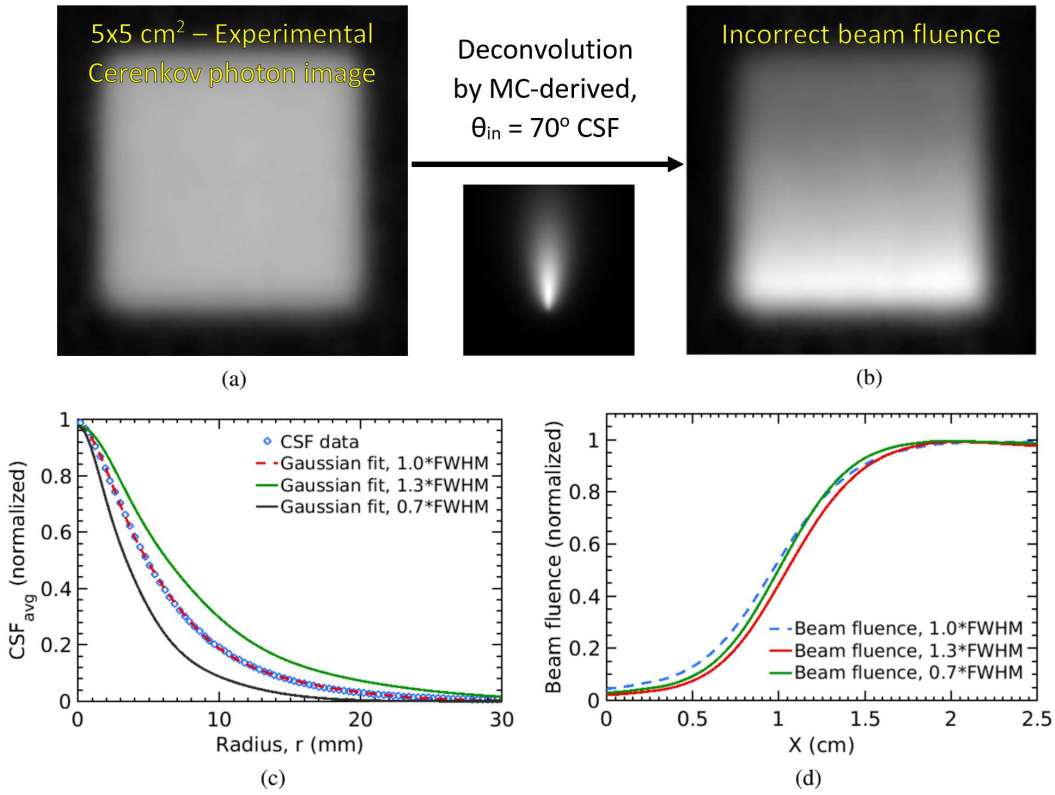

Figure 4.6: (a) The experimental Cerenkov photon image taken with a 5x5 cm^2 6 MV polyenergetic photon beam incident on the optical phantom. This image has been perspective corrected, then temporal and spatially filtered to remove stray radiation noise. (b) Here, the image in (a) has been deconvolved with the incorrect CSF. This image was deconvolved by the mono-energetic θ_{in} =70° CSF. This image represents the beam fluence according to Equation (3.4), however, here it is purposefully incorrect for the purtubation analysis. (c) A cross-section of the CSF from the 6 MV polyenergetic beam with a triple-Gaussian fit. The FWHM of the fit was scaled and overlaid, as shown. (d) The response of the fluence profile to changes in the CSF-FWHM; (a) deconvolved by the CSFs portraied in (c).

second minimum at a relative CSF-FWHM of 0.5.

Figure 4.7(c) shows the MSE when modifying the CSF-FWHM in comparison to Monte Carlo calculated dose. This figure shows three lines for three different convolution functions: deconvolution by the CSF (Decon. by CSF), deconvolution by the CDSF (Decon. by CDSF), and deconvolution by a δ-function (Decon. by δ). Note that the δ-function deconvolution represents the raw experimental Cerenkov photon image,

yielding a constant value for comparison purposes. The MSE reaches a minima at a relative CSF-FWHM of 0.60 for the scaled fluence image and 0.75 for the scaled dose image. According to our formulation, the minimum value of the scaled dose image trend should lie at a relative CSF-FWHM of 1. However, because an experimental dose image is compared to to Monte Carlo calculated dose, any discrepancies or unaccounted for physical effects in the Monte Carlo simulation will modify the location of the minimum value in this trend. For example, not accurately representing the complex micro-surface structure that exists on the experimental optical phantom in the simulation will lead to discrepancies in the results. The surface micro-structure will realistically modify the CSF shape, which may slightly change the shape and profile of the deconvolved dose image.

Additionally, if the PSF of the imaging system is not ideal, blur may exist in portions of the experimental Cerenkov photon image used in deconvolution. Imaging blur leads to further spreading out of photons in the Cerenkov image, which in turn widens the CSF or CDSF beyond what would be required of an ideal imaging system. Therefore, blur or a non-ideal imaging system would shift the minimum value of the trends in Figure 4.7(c) to the right, to a relative CSF-FWHM >1. Because these trends reach a minimum at a relative CSF-FWHM <1, the experimental imaging system used was close enough to an ideal or diffraction-limited case and the simplification used on Equation (3.4) was valid.

The scaled dose image trend in 4.7(c) is expected to reach a minimum value closer to a relative CSF-FWHM of 1 in comparison to the scaled fluence image. The CDSF is calculated from deconvolution of the CSF by the DSF. In general, for superficial dosimetry ($d < d_{max}$), the DSF will be very narrow in comparison to the CSF [100]. Because of this, the CDSF will retain the overall shape of the CSF but will be sharpened slightly. This effect is shown in the similarity between the MSE trends between the scaled dose and scaled fluence images. The fact that the MSE with CDSF is smaller than the MSE with CSF and is closer to a relative CSF-FWHM of 1 implies that the use of CDSF for dose estimation from the raw Cerenkov image is the correct approach. Figure 4.7(c) also shows that the MSEs of the fluence and dose images fall below the value of the raw experimental image trend. This shows the validity of our mathematical approach in solving for and improving the light-to-dose correlation.

Figure 4.7(d) shows the MSE when varying the CSF-amplitude. The trend in this error is seen as a simple parabolic curve. Changes to the CSF-amplitude will result in an exponential increase in the magnitude of the fluence image after deconvolution.

Figure 4.7(e) shows the gamma passing rate when changing the angle of the CSF. The passing rate decreases sharply beyond an angle of θ_{in} >6° for all gamma criteria with a DTA $\geqslant$1 mm. This is primarily due to the gradient created across center of the field for increasing values of θ_{in}, as seen in Figure 4.6(b). The gamma passing rate decreases much more quickly for the 3%/0mm criteria, as this is strictly a measure of the dose difference between the images. The gamma passing rate flattens out beyond θ_{in} >45° for all gamma criteria with a DTA $\geqslant$1 mm. For this region, the dark areas just beyond the penumbra will still have acceptable passing rates, which creates the baseline passing value observed.

Figure 4.8(a) shows a map of the global error determined by Equation 4.4 as the function of CSF-amplitude and CSF-FWHM. Also shown in the Figure 4.8(a) are the points of CSFs for various photon energies and medium types as given in Table 5. The cluster of points in the bottom left represent the CSFs of the stratified skin models at 6, 10, and 18 MV polyenergetic photon beam energies. The three points on the top right represent the CSFs of the optical phantom at the three beam energies. Overlaid on this map is a topographic representation of the global error, relative to the 6 MV light skin CSF data point. The CSFs of all skin models lie within a 1% global error from one another. Using the CSF of any skin model in deconvolution yielded an almost identical result when comparing the penumbra shape or image magnitude. However, the application of the CSF of the optical phantom to a Cerenkov image captured from any stratified skin yielded a greater than 38% error in the deconvolved image. Figure 4.8(b) gives an expanded view of the CSFs of the stratified skin model data points shown in Figure 4.8(a).

4.4 Discussion

The global error shown in Figure 4.8 was calculated using two separate metrics. Both the penumbra error due to CSF-FWHM and the MSE due to CSF-amplitude reflect the changes in the deconvolved image that we are primarily interested in quantifying.

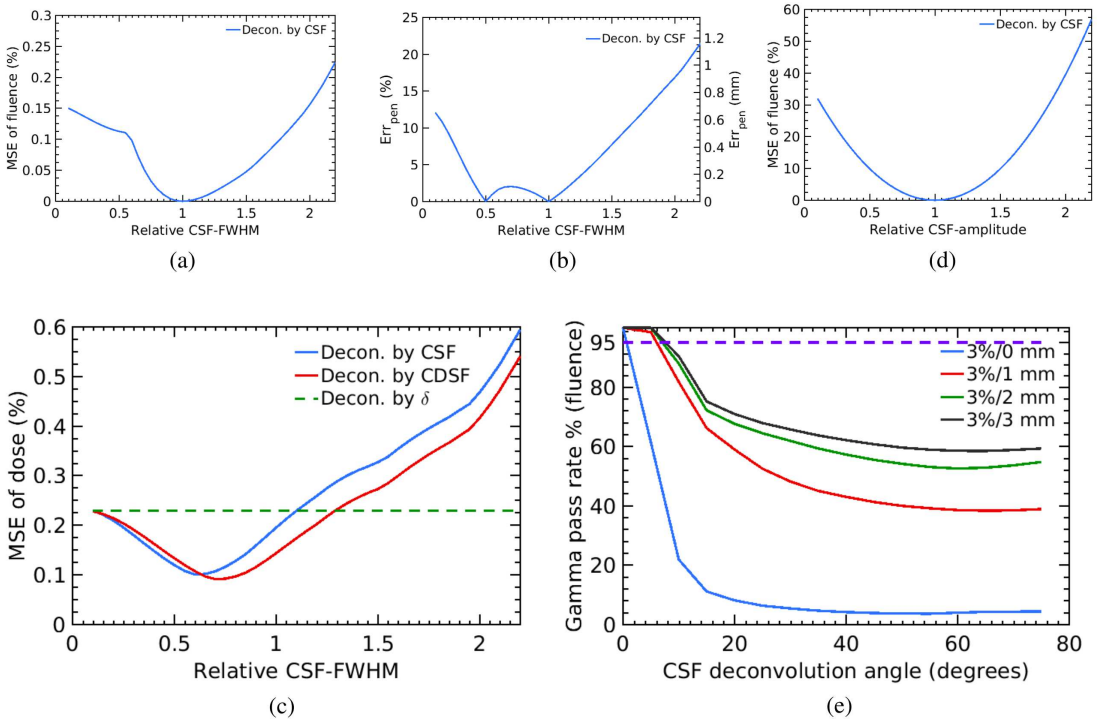

Figure 4.7: The results of the perturbation analysis. (a) The MSE of the beam fluence with respect to itself when modifying the CSF-FWHM. (b) The penumbra error for the fluence image when modifying the CSF-FWHM. (c) The MSE of the various images with respect to the Monte Carlo calculated dose for the same field size, beam energy, and optical phantom model. This image shows three trendlines: deconvolution by the CSF representing the fluence image, deconvolution by the CDSF representing the dose image, and deconvolution by a δ-function representing the raw experimental image. (d) The MSE of the fluence image with respect to itself when modifying the amplitude of the CSF. (e) The gamma passing rate of the fluence image in comparison to the CSF of θ_{in} =0° when changing the entrance angle of the CSF used in deconvolution, as shown in Figure 4.4.

Modifying the CSF-FWHM alone changes the response of the high gradient regions in the deconvolved image, such as the penumbra. Modifying the amplitude alone changes the overall image magnitude but does not modify the image profile. Using the MSE as a metric for the CSF-FWHM does not capture the direct effect on the penumbra. Using the penumbra error as the metric for the CSF-amplitude does not capture the direct effect on the magnitude of the whole image. Therefore, these two different metrics are

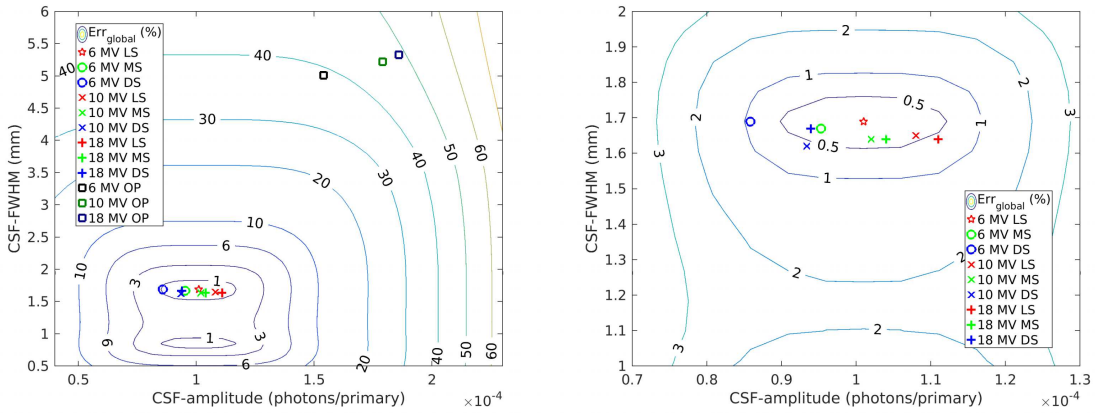

Figure 4.8: (a) A map of the FWHM and amplitude of CSFs generated for the optical phantom (OP), light skin (LS), medium skin (MS), and dark skin (DS) models for 6, 10, and 18 MV polyenergetic beams. Overlaid on this map is the global error in the deconvolution process relative to the 6 MV light skin CSF data point, denoted by a star. The global error was generated as the quadrature of the error in the penumbra measurement for the CSF-FWHM axis and the MSE for the CSF-amplitude axis. The global error displays what the error in the deconvolution product image when using an incorrect CSF. (b) An expanded view of the skin model CSFs shown in (a).

used in one formulation, Equation (4.4), to give a relative estimate of the global error which is expected to arise when deconvolving with an incorrect CSF.

In this paper, the effects of the measurement setup parameters on the CSF and the deconvolved image were studied. These included the beam energy, the irradiated material, and the incident beam angle. It was observed that the beam energy had a noticeable effect on the CSF-amplitude and almost no effect on the CSF-FWHM. The 6 MV CSF-amplitude in the light skin model increased by 6.9% and 10% when the beam energy increased to 10 and 18 MV, respectively. This increase propagated the deconvolution process to yield a 0.3% and 0.5% difference in the global error of the product images, respectively. Therefore, using the CSF with an incorrect photon energy in deconvolution is insignificant.

The irradiated material had a large effect on both the CSF-amplitude and CSF-FWHM. For a 6 MV beam energy, changing from a light skin model to the optical phantom increased the CSF-amplitude by 52% and the CSF-FWHM by 196%. This change propagated the deconvolution process to yield a 39% difference in the product

image using the global error. The irradiated skin-pigment had a small effect on of the CSF-amplitude and no effect on the CSF-FWHM. For a 6 MV beam energy, changing from light skin to medium or dark decreased CSF-amplitude by 6% and 15%, respectively. This decrease propagated the deconvolution process to yield a 0.2% and 0.9% difference in the global error of product images, respectively. Therefore, using the incorrect CSF material has a significant effect on the deconvoluted images, however, using the CSF of an incorrect skin type in deconvolution is insignificant.

The result of errors introduced by changing the beam angle is more difficult to evaluate. It was observed that changing the beam angle from 0° to 35° introduced errors in the deconvolution process that caused the gamma passing rate to decrease to 45%, as per the 3%/1 mm criteria. This effect would be considered very significant. Hence, the space-invariant assumption used for the current mathematical algorithm is not valid when the incident beam angle change is large. To solve this problem, deconvolution will no longer be performed with a single CSF or CDSF over the whole image. Regions of near-uniform beam angles will be deconvolved by the CSF corresponding to that similar beam angle following piece-wise deconvolution techniques. Under this analysis, to minimize the error in the deconvolution product, the range of angles used in a single area of deconvolution should be no more than $\Delta\theta_{in} = 6.04°$, as per the 3%/1 mm gamma criteria. This constraint will keep the gamma passing rate above 95% for that region. This result can be used to partition an image into regions bounded by a difference in the beam entrance angle before piece-wise deconvolution is performed.

4.5 Conclusions

In this chapter, the Cerenkov scatter function (CSF) was more fully characterized. The CSF was found in models of light, medium, dark stratified human skin, and an optical phantom for polyenergetic photon beam energies. The CSF was also solved for oblique incident beam angles in both the light skin and optical phantom models. The CSFs of normally incident beams were fit with a triple-Gaussian function and the coefficients were provided. These coefficients can be used to generate a radially-symmetric CSF which can be used in deconvolution with a measured Cerenkov photon image to find either the beam fluence or dose distribution with a known dose scatter function (DSF).

Perturbation analysis was performed to study the sensitivity of the deconvolved images on the shape and amplitude of the CSF, beam energy, incident beam angle, and the type of medium. The CSF-amplitude and full-width at half-maximum (FWHM) was found to have significant effects on deconvolution. An increase in the CSF-amplitude propagated as an exponential increase in the amplitude of the deconvolved image. An increase in the CSF-FWHM propagated as a near-linear increase in the penumbra width of the deconvolved image. The energy of the beam used to create the CSF was found to be insignificant to the deconvolution process. The angle of the beam used to create the CSF was found to be significant in the deconvolution process. The result suggests the need to move towards piece-wise, space-variant deconvolution when imaging a beam with multiple entrance angles. The incident beam angle used for the CSF should vary by no more than 6.0° for a single region of deconvolution. The material model used to generate the CSF has a significant effect on deconvolution. The CSF from one material should not be used on another. However, the pigment of human skin does not have a significant effect on the deconvolution process. The CSFs of different skin tones can be used interchangeably with a $<1\%$ error in the deconvolution product image.

Chapter 5

Space-Variant Deconvolution of Cerenkov Images

This chapter is derived from a manuscript that has been submitted to the journal Medical Physics for publication in April, 2019, titled as: E. E. Brost and Y. Watanabe, "Space-variant deconvolution of Cerenkov light images."

5.1 Introduction

The previous chapters introduced a system of equations that can be used to relate an image of Cerenkov photons to superficial dose deposition using a deconvolution formulation [100]. The deconvolution formulation was chiefly dependent on a Cerenkov photon transport kernel, called as the Cerenkov scatter function (CSF) [88]. In Chapter 3, the deconvolution formulation was validated on flat surfaces using an optical phantom and a high energy photon beam from a LINAC. It was shown that the deconvolution of the Cerenkov photon images by using the CSF could improve the accuracy of dose distributions near the field edge. This indicated that the deconvolution formulation can be used to improve Cerenkov photon images with steep gradient regions. In Chapter 4, the CSF was more fully explored for use in clinically relevant materials, namely human skin tissue. MC simulations were used to generate CSF distributions in a stratified skin model using three different skin tones (light, medium, and dark) and in an optical phantom material. A triple-Gaussian fit was used on all CSF distributions and coefficients

were provided for 6 MV, 10 MV, and 18 MV treatment energies. Perturbation analysis was performed to test the limitations of the deconvolution formulation.

These previous chapters characterized the use of the deconvolution formulation and the CSF for Cerenkov photon images taken from a flat surface; however, a more clinically relevant geometry is a curved or uneven surface. Application of the deconvolution formulation, as previously defined, to a curved surface will fail, as it relied on the assumption of a space-invariant CSF. The beam incident angle on a curved surface varies due to both the surface geometry and the beam divergence. As the beam incident angle increases, the CSF shape significantly changes. The CSF becomes elongated in the direction of the beam due to a larger superficial photon diffusion within the irradiated medium. Chapter 4 showed that the beam incident angle should change by no more than 6° in order to retain an acceptable deconvolved image as per a 3%/1 mm gamma analysis criteria. Therefore, for Cerenkov photon images taken on a curved surface, the assumption of a space-invariant CSF is invalid and space-variant deconvolution is necessary.

This chapter explored space-variant deconvolution techniques applied to Cerenkov photon images taken on a curved surface. First, the most optimal deconvolution algorithm was selected using a flat surface Cerenkov photon image compared against the primary beam fluence. Second, the parameters of space-variant deconvolution were optimized through perturbation analysis on a composite Cerenkov photon image. Experimental images taken from a curved surface must be perspective corrected before deconvolution, so an image registration technique was applied to map a curved to a flat surface. The optimized deconvolution parameters and image registration technique were applied to experimental Cerenkov photon images taken during EBRT. To test the space-variant deconvolution method, an optical phantom with a curved surface was used.

5.2 Theory

Space-variant degradation of images is a common problem in image deblurring. Some modern charged-coupled device (CCD) and complementary metal oxide semiconductor (CMOS) arrays in digital cameras read out the sensor signals line-by-line, resulting in

image capture taking place over a finite time period [106]. Motion of the camera during this time period can cause space-dependent degradation; the point spread function (PSF) of the imaging system will differ between regions on the image. Another example of space-variant degradation can arise when capturing an image with objects existing in multiple focal planes. An imaging system may capture part of the image within the depth of field of one focal plane, but a portion of the image may appear out-of-focus if it is outside of this range. This situation causes the PSF to differ between regions of the image corresponding to different focal plans. Other applications where space-variant degradation of images can occur include astronomy [107] and single photon emission computed tomography (SPECT) [108].

There have been multiple algorithms developed to correct for forms of space-variant degradation in images. Bar et al. approached the problem of space-variant degradation with known and unknown boundary conditions between blur regions using space-variant deconvolution with a unified common regularizer [99]. Sroubek et al. showed that space-variant blur kernels can be decomposed into singular values which can be used to represent all blur kernels in linear combination [98]. Sindelar and Sroubek showed that an array of space-variant kernels can be estimated using the gyroscopic information recorded in tandem with image collection on a smart phone[106, 109]. This array of kernels was used to deconvolve an image with space-variant blur using a block-deconvolution process.

For space-invariant deconvolution, imaging deblurring takes the approach of a space-invariant kernel plus any added noise:

$$g = h * f + n, \tag{5.1}$$

where g is the degraded observed image, h is the space-invariant blur kernel, $*$ is the convolution operator, f is the ideal image without blur, and n is the added noise. Equation 5.1 is valid only under the assumption that the blur kernel is space-invariant and fails in the space-variant case.

In the space-variant case with a linear blur applied to the image, Equation 5.1 becomes:

$$g = \int h(s, s-u) f(u) du + n, \tag{5.2}$$

where s is a location in the observed image and u is a location in the ideal image.

Figure 3.1 in Chapter 3 shows a diagram of the physical processes and coordinate system used to mathematically define the imaging of Cerenkov photons during EBRT. This coordinate system and the physical equations for this imaging were previously defined in Chapter 3. In this chapter, the formulation was expanded to the space-variant case. A high energy photon beam incident on a medium in the Z-direction is considered as the primary radiation source. An imaging system is placed at an angle relative to the beam on the same side of the medium as the radiation source. The high energy photon beam produces secondary electrons which are responsible for both energy deposition and creation of Cerenkov photons within the medium. The relationship between the fluence of the primary photon beam and the intensity of the Cerenkov photons reaching an imaging system is defined as:

$$\begin{aligned} I(i,j:\theta_{obs}) = \int d\mathbf{\Omega} \int\int dx\, dy \int\int dX\, dY \\ J(x,y,\mathbf{\Omega})\, CSF(x-X, y-Y, \mathbf{\Omega}, \theta_{obs})\, PSF(X-i, Y-j), \end{aligned} \tag{5.3}$$

where I is the Cerenkov photon intensity at a pixel (i,j) on the image sensor of the imaging system, J is the total fluence of the photon beam with a known energy spectrum entering the medium at the surface point (x,y,z_s) with an entrance vector of $\mathbf{\Omega}$ relative to the surface normal, CSF is the Cerenkov scatter function, and PSF is the point spread function representing the transport of Cerenkov photons from the surface at point (X,Y,z_s) to the imaging system. The coordinates x, y, X, and Y are defined on the surface of the irradiated medium at $z = z_s$. The parameter θ_{obs} is the observation angle of the imaging system relative to the surface normal. Equation 5.3 fails in the case of space-variance for the CSF and PSF; the shape and characteristics of these kernels should not change throughout the image I.

For a finite-width radiation field applied over a curved surface, the assumption of space-invariance is broken. The CSF shape and amplitude will change depending on the beam entrance vector at any location. The space-variant form of Equation 5.2

can be applied to Equation 5.3 for the purpose of imaging Cerenkov photons over an arbitrarily-shaped surface S given as $z_S = p(x, y)$:

$$I(i,j) = \int d\mathbf{\Omega} \int\int dx\, dy \int_S dS$$
$$J(x, y, \mathbf{\Omega}(x, y))\, CSF(x - X, y - Y, \mathbf{\Omega}(x, y), \theta_{obs}(x, y))\, PSF(X - i, Y - j), \qquad (5.4)$$

where $CSF(x - X, y - Y, \mathbf{\Omega}(x, y), \theta_{obs}(x, y))$ is the space-variant Cerenkov scatter function, (x, y, z) are arbitrary coordinates in the 3D system, and point (X, Y) exists on the surface S. This integral is performed over the surface S and the transfer functions CSF and PSF collapse the surface defined in (x, y, z_S) into the imaging coordinates (i, j). In this form of the equation, the CSF can vary as a function of the beam entrance position (x, y, z) depending on the beam entrance vector $\mathbf{\Omega}$. $\mathbf{\Omega}$ can be broken down into the components: θ_{in}, the angle of entrance vector defined from the surface normal and ϕ, the rotation of the entrance vector about the z-axis. The angle and rotation of the entrance vector will vary with (x, y, z_S) depending on the patient set-up position, the patient surface geometry, and beam divergence. Ultimately, these are all known parameters which can be measured during treatment in order to solve for the CSF in different regions of an image.

One caveat to the extension of Equation 5.3 to Equation 5.4 is that in accounting for variations in the surface geometry through the beam entrance vector, the angle of observation changing over the surface must also be acknowledged. The patient set-up position and surface geometry will cause the angle of observation θ_{obs} to become dependent upon the (x, y) location on the surface S. The concept called as the directional radiance distribution function (DRDF) describes the dependence of the observed Cerenkov radiance as a function of observation angle[88]. I theorize that this distribution function has properties similar to that of the bidirectional reflectance distribution function (BRDF). The BRDF is dependent upon material composition and the imaged surface microstructure [110]. While the effects of the DRDF may be critical to precise absolute dosimetry preformed with Cerenkov photons, they were not included in this formulation. The DRDF will be ignored in this chapter and will be discussed in further detail in Appendix A.

Note that in Equation 5.4, the variation of the beam entrance vector and observation angle in (x, y, z) coordinates can be collapsed into the imaging coordinates (i, j) after perspective transformation. This will be discussed in further detail in the following sections. In addition, by considering an ideal imaging system, the PSF could be set to be equal to a Dirac delta function. This allows us to ignore the PSF term in both Equations 5.3 and 5.4.

Chapter 3 used the dose scatter function (DSF) to solve for superficial dose deposition in an optical phantom. However, in this chapter, the focus is on applying a space-variant deconvolution formulation. Therefore, the DSF will be ignored here; to solve for superficial dose on a curved surface image, space-variant convolution would also be necessary. This is a non-trivial task; therefore, the focus of this chapter will be on the limitations and application of space-variant deconvolution to solve for the surface beam fluence J rather than superficial dose deposition.

5.3 Materials and Methods

5.3.1 Monte Carlo Simulations

GAMOS (version 4.0.0), a Geant4 (version 10.02) based MC toolkit for medically-oriented applications, was used to create all simulations[3]. The Tissue Optical Modeling plugin was used with GAMOS to simulate the optical physics and handle optical properties [18]. Two sets of simulations were performed in order to solve (A) the CSF distribution for different angles of incidence using a pencil beam of radiation and (B) the primary x-ray beam fluence on curved and flat surfaces for square field sizes. All simulations were performed using a simulated optical phantom material with absorption and scattering coefficients matched to a physical optical phantom, which was characterized by the manufacturer (INO, Ontario, Canada). The absorption and reduced Mie scattering coefficients had values of μ_a = 0.3-0.0002 $\times$ (λ-450) cm^{-1} and μ_s' = 114.0 cm^{-1}, respectively, where λ is the wavelength. The index of refraction of the optical phantom was $n = 1.40$ for wavelengths from 400-800 nm. The physical optical phantom was made from polyurethane resin; therefore, the simulated phantom was given the atomic composition of this material.[111]

The primary radiation source for all simulations was a 6 MV photon beam with

the energy spectrum of a Varian TrueBeam linear accelerator (Varian Medical Systems, Palo Alto, CA). Simulation set (A) used a pencil beam incident on a flat phantom surface at angles of θ_{in} =0-34°, at 1.5° increments. Simulation set (B) used a square field incident on both a flat and curved optical phantom surface. The curved optical phantom surface was a semi-cylindrical shape with a radius of curvature of 9.8 cm and matched the dimensions of the physical optical phantom used in imaging experiments. Field sizes used in simulation set (B) matched those used in experiments. Simulation set (B) utilized phase space data from the Varian TrueBeam LINAC, which was mirrored four times across the quadrants delineated by the X-Y axes to add additional histories to the available data.

In each simulation, the Cerenkov photons of wavelengths from 400-800 nm that escaped the medium surface were scored and the initial position, initial direction, final position, final direction, and wavelength were recorded. In addition, the initial position and initial direction of primary particles entering the phantom were recorded. The position information was used to generate CSF images and primary beam fluence profiles. The CSFs from simulation set (A) were generated by binning the surface-escaped Cerenkov photons in an 11x11 cm^2, 600x600 bin grid. The fluence profiles from simulation set (B) were generated by binning the primary beam fluence entering the phantom in a 11x11 cm^2, 300x300 bin grid. The "GmEMPhysics" model was used in all simulations. The step sizes and range cuts for all particles were kept at default in each region. The general photon production threshold was between 0 eV to 1 GeV. The maximum number of Cerenkov photons per step was kept as unlimited. CSF simulations were run with 1×10^9 histories in order to minimize statistical uncertainties.

5.3.2 Imaging Experiments

Cerenkov photon images were captured using a Canon EOS 6D commercial camera equipped with a 20.2-megapixel CMOS sensor and square pixel size of 6.55 μm (Canon USA, Huntington, NY). An optical phantom fabricated and characterized by INO, with dimensions of 7x11x11 cm^3, was used in all imaging experiments. The front surface of the phantom was milled into a semi-cylindrical shape with a radius of curvature of 9.8 cm. The optical phantom was mounted to the gantry head of the TrueBeam with a custom attachment. The apex of the curved surface was placed at a 100 cm

source-to-surface distance and the camera was placed at a distance of 100 cm from the optical phantom. The camera was controlled using the default commercial software, EOS Utility, (Canon USA) which allowed for remote shooting through a USB cable on a laptop computer placed at the LINAC control console. The room was darkened as much as possible to reduce stray photons reaching the camera. Photos and a diagram of the experimental setup can be seen in Figure 3.3 from Chapter 3.

One data set was collected during imaging experiments. A 6 MV photon beam was used to irradiate the phantom with various open field sizes ranging from 2x2 through 8x8 cm^2. A dose rate of 600 MU/min was used with a 1 second exposure time at 1000000 ISO. The average of 10 images were taken and spatially filtered with a 15-pixel Gaussian filter in ImageJ (National Institutes of Health, Bethesda, MD) to form the resultant image, as used in previous chapters [88, 100].

5.3.3 Perspective Correction of a Curved Surface

Before deconvolution was applied to the images collected from the curved optical phantom, mapping from the imaged curved surface to a flat surface was required. This was necessary as CSFs were derived from a flat surface using the MC results. Perspective correction of experimental images was shown in Chapter 3, however, this form of correction only accounted for perspective distortion due to the imaging angle. This method alone could not perform the full mapping of the curved surface to a flat surface.

A simple method for mapping a curved to a flat surface is described below. This process relied on a transformation matrix used to map a distorted flat surface to an objective square surface, as shown in Chapter 3. The curved surface is assumed to be composed of a finite number of small flat uniform squares in an array flush across the surface. An example of this applied to the optical phantom can be seen in Figure 5.1(a). The process of breaking the curved surface into square elements approximates lines projected onto the surface as being composed of a finite number of smaller straight lines. In this manner, a small amount of information may be lost at the periphery of the square elements if the image of individual squares is much larger than the pixel size on the camera. In the imaging experiments, the square elements were approximately 20 pixels in size, so this effect was considered negligible.

The square elements were generated as a 34x32 checkerboard pattern with 0.344x0.344

cm^2 checkers. The checkerboard was printed onto a piece of office paper and attached flush to the curved surface on the optical phantom. The checkerboard was used to register the pixel coordinates at the junction of adjacent checkers. A custom program was written in Matlab (MathWorks, Natick, MA) using the detectCheckerboardPoints function to detect junctions on the checkboard where four individual checkers met, thus, the middle 32x30 points of the printed board were registered. With the pixel coordinates of checker junctions found, individual checkers were perspective transformed to objective squares. This was performed over the full set of checkers such that the final result was a square image representing a projection of the curved, distorted surface to a square flat one. The result of this transformation can be seen in Figure 5.1(b). The registration image was taken with the room lights on before Cerenkov photon images were acquired. After the registration was performed on the checkerboard image, the same process was applied to all experimental Cerenkov photon images so that all results were square images. Since the size of the overall image was 10.31x11.00 cm^2, pixels with zero values were added to the margins of the image so that the final image size was 11x11 cm^2 at 600x600 pixels. These dimensions matched those of the MC-derived CSFs.

The front surface of the phantom was cylindrical, therefore, experimental images mapped to a flat surface had to be given coordinates along the surface of the cylinder. The X-direction was with the curve of the phantom, so the image coordinates in this direction were solved as:

$$X_{corr} = 9.8 \times arctan(\frac{X}{\sqrt{9.8^2 - X^2}}) \tag{5.5}$$

where X_{corr} is the correct coordinates and X is original distance from the center of the image in centimeters. The Y-direction was against the curve of the phantom and no coordinate correction was required. In addition, for space-variant deconvolution, the entrance angle of the beam, θ_{in}, at any point on the curved phantom surface had to be obtained. This was solved by considering the set-up geometry including the beam divergence and the phantom curvature.

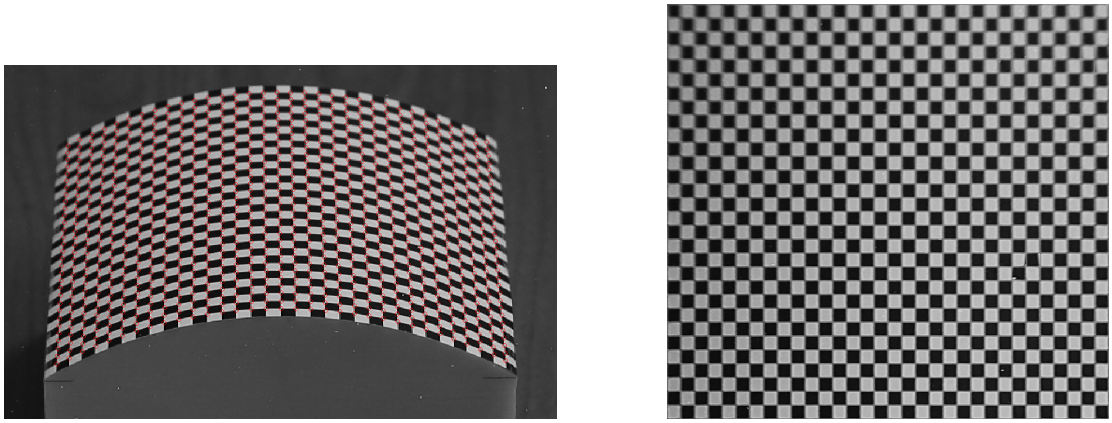

(a) (b)

Figure 5.1: The checkerboard registration method applied to the front curved surface of the optical phantom. (a) In the full image of the phantom, the checker corners are detected. (b) The central checkers are individually transformed into objective squares. This operation is performed over the central checkers to map all but the edges of the curved surface to an objective square.

5.3.4 Selection of Deconvolution Algorithm

After perspective correction, experimental images were subject to deconvolution in order to compare the incident fluence profiles determined from the experimental Cerenkov photon images with MC fluence profiles. Both space-variant and space-invariant deconvolution were used throughout this chapter. The most optimal deconvolution algorithm was selected using the MC fluence profile from a 5x5 cm^2 6 MV field on a flat optical phantom surface, and the experimental data corresponding to this configuration from Chapter 3. Deconvolution was performed on the experimental Cerenkov photon image to select the algorithm which produced the profile closest to the beam fluence. Three deconvolution algorithms were tested: Lucy-Richardson, Blind, and Total Variation (TV/L2) deconvolution [112, 113, 114, 115].

TV/L2 deconvolution followed the form:

$$\text{minimize } f: \quad \frac{\mu}{2}||h * f - g||^2 + ||f||_{TV} \tag{5.6}$$

which is known as the TV/L2 minimization [116]. In this problem, μ is the regularization

parameter, $||\cdot||^2$ is the conventional L2 norm squared, and $||f||_{TV}$ is the isotropic TV norm. The solution to this problem is based upon the parameter μ, which trades off between the importance of the least squared error and a penalty term. The value of μ is not known prior to minimization, therefore, selection of μ is based upon desired results. Larger values of μ tend to give a sharp image, but amplify noise. Smaller values of μ tend to give less noisy results, but smooth the image. In general, this algorithm was found to be desirable for Cerenkov imaging applications because the solution to the TV/L2 minimization preserves flat regions but also accentuates high-gradient regions, such as the penumbra region in the profiles of radiation beams.

TV/L2 deconvolution was applied to images using the Matlab algorithm deconvtv written by Chan, et. al [116]. The values of μ and the number of iterations used by this algorithm were perturbed to find the most optimal values. The other parameters of this algorithm were kept to their default values. Lucy-Richardson and Blind deconvolution were also performed in Matlab using the deconvlucy and deconvblind functions, respectively, under the default parameters.

5.3.5 Space-Variant Deconvolution Method

Space-variant deconvolution was carried out using the block-deconvolution process outlined by Sindelar and Sroubek [106]. This method relies on three steps. In Step 1, the image is partitioned into regions corresponding to various CSFs. Region edges are delineated into blocks by which the CSFs are determined to be near-uniform ($\Delta\theta_{in} < 6°$, as per Chapter 4). Each block is extracted along with a surrounding margin in order to reduce edge artifacts. The block plus the margin area is referred to here as the partition. The CSF was cropped to match the size of the partition. In Step 2, the partition is deconvolved by the corresponding CSF. The deconvolved partition may be additionally windowed by an edge-tapering or Hanning filter to improve blending with adjacent regions [106]. In Step 3, the margin is trimmed and the deconvolved block is patched into its original location. These steps are repeated for the full Cerenkov photon image to obtain a 2D fluence image.

Figure 5.2 shows the steps of the block-deconvolution process applied to an experimental Cerenkov photon image of a flat surface. Figure 5.2(A) represents a composite image derived from combining Cerenkov photon images of 3x3 and 5x5 cm^2 6 MV

open fields, which were taken from the data presented in Chapter 3. The three steps of the block-deconvolution process are shown in the center. Figure 5.2(B) shows the block-deconvolution product.

Images (A) and (B) served as the basis for optimization of the block-deconvolution parameters through perturbation analysis. The CSF of a 6 MV photon beam for the 0° incident angle was used in deconvolution throughout all of image (A). The images obtained by using the block-deconvolution method were compared with the images obtained from direct application of deconvolution to the whole image (space-invariant deconvolution). The comparison was made using gamma analysis with a 1%/1 mm criteria and mean-squared error (MSE) [104].

The sizes of the block and margin were optimized using perturbation analysis. First, the block size was optimized by varying the square block size from 0.2 to 50% (or 1 to 250 pixels) of the image width. The margin size was set to the 100% (or 500 pixels) of the image width. Second, the margin size was optimized by varying the size from 0 to 100% of the image width for a fixed block size of 20% image width (100 pixels). The margin was added to four directions uniformly so that it retained square dimensions. When the margin extended from the partition into the image, the image information was retained and added to the total partition area. When the margin extended from the partition outside of the image, the pixel value of the margin was set as zero.

Once the deconvolution algorithm was selected and the block-deconvolution parameters were optimized, space-variant deconvolution was applied to the Cerenkov photon images taken from the curved phantom surface. Four partitioning schema were tested on the curved surface Cerenkov photon images: partitioning of the image into columns corresponding to a CSF change of $\Delta\theta_{in} = 3°$, partitioning into columns for $\Delta\theta_{in} = 1.5°$, partitioning only the penumbra region of the image with $\Delta\theta_{in} = 1.5°$, and partitioning the image into a grid of 20x20 blocks. In the last partitioning schema, the CSF angle in each block was solved using a histogram from the MC beam fluence in addition to the known phantom curvature.

A flowchart showing all steps from data collection to image processing for space-variant deconvolution is shown in 5.3. For remainder of this chapter, a "space-invariant deconvolved image" refers to a fluence profile obtained by deconvolving a Cerenkov photon image by the space-invariant method. A "space-variant deconvolved image"

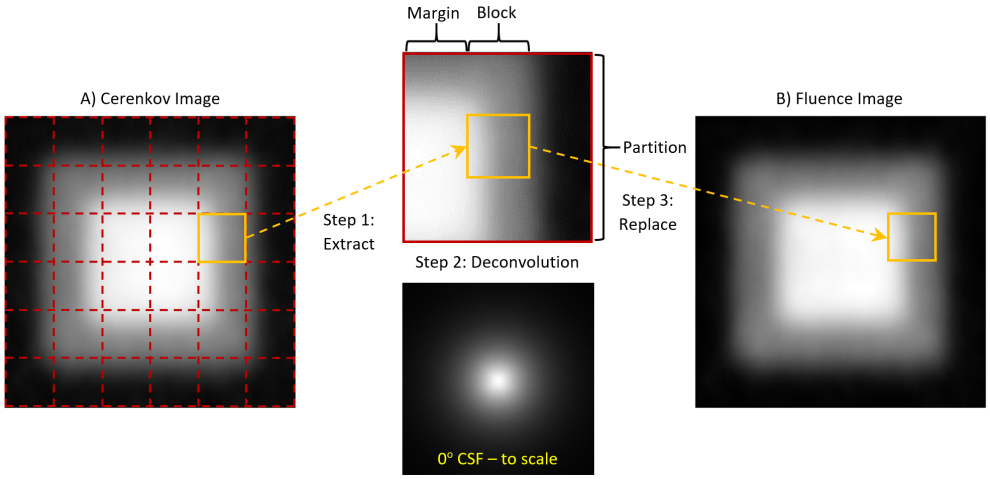

Figure 5.2: A demonstration of space-variant deconvolution applied to a composite 3x3 and 5x5 cm^2 Cerenkov photon image taken on the flat surface of the optical phantom. Image (A) on the left shows the raw composite Cerenkov photon image partitioned into 36 blocks. The middle of this figure shows the 3 steps of block-deconvolution. Step 1: extraction of a block along with a surrounding margin. Step 2: deconvolution of the full partition by the corresponding CSF ($\theta_{in} = 0°$ CSF is shown here). Step 3: replacement of only the block region to the original location. These steps repeated over the full image (A) form image (B), representing the primary beam fluence.

refers to a fluence profile obtained by deconvolving a Cerenkov photon image by the space-variant method.

5.3.6 Image Analysis

Cross-line profiles from the raw curved images, space-invariant deconvolved images, and space-variant deconvolved images were generated using the average pixel values from the central 20% of the field width. These profiles were compared against the MC calculated primary beam fluence.

On all cross-line profiles, the field width and penumbra were measured. The field width was defined as the full width at half of the maximum (FWHM) and the penumbra was defined as the distance between the 20% to 80% of the maximum value.

The MSE of images was calculated using the *immse* function in Matlab, found as:

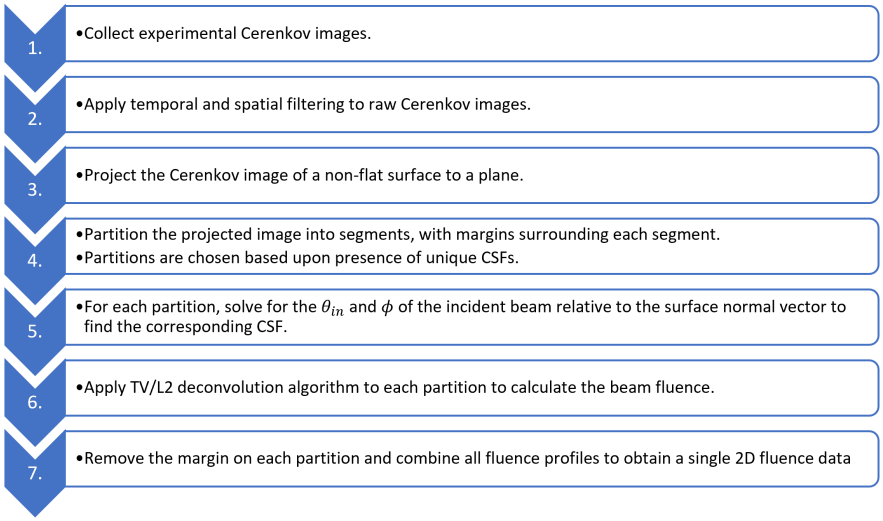

Figure 5.3: A flowchart of all steps required for space-variant deconvolution of curved surface Cerenkov photon images.

$$MSE = \frac{1}{N\, I_{max}} \sum_{n=1}^{N} [I_{comparison}(n) - I_{reference}(n)]^2 \tag{5.7}$$

where n is the index of individual image pixels, N is the total number of image pixels, $I_{comparison}$ is the comparison image, $I_{reference}$ is the reference image, and I_{max} is the maximum value of $I_{reference}$ for normalization. 2D gamma analysis was performed using the definition for γ given by Low, *et al.* [104]. The gamma passing rate between images was calculated in Matlab with custom-written software.

5.4 Results

5.4.1 Selection of Deconvolution Algorithm

Figure 5.4 shows the results of selection of the deconvolution algorithm. The figure shows the beam fluence profile calculated by the MC simulation and three profiles obtained by applying the Lucy-Richardson, Blind, and TV/L2 deconvolution methods to the raw Cerenkov photon image (shown as a dashed red line). The deconvolved image profile from the Blind deconvolution method exactly matched the Lucy-Richardson profile.

Here, it is seen that the TV/L2 provided a near perfect solution to the deconvolution problem. Both the profiles from the Lucy-Richardson and Blind methods were closer to the imaged profile than that of the fluence and did not produce a satisfactory result. Hence, the TV/L2 method was applied to space-variant deconvolution of curved surface Cerenkov photon images.

Figure 5.5 shows the optimization of the parameter μ and the number of iterations used in the TV/L2 deconvolution method. The MSE displayed in this figure was calculated using the deconvolved 6 MV 5x5 cm^2 open field Cerenkov image compared to the primary beam fluence. Figure 5.5(a) shows that the most optimal value of μ is 1.0e-7. Figure 5.5(b) shows that one iteration of deconvolution provides the most optimal deconvolution result, which is in agreement with Chapter 3. All deconvolved images and profiles shown for the remainder of this study were obtained using the TV/L2 algorithm with these optimized values.

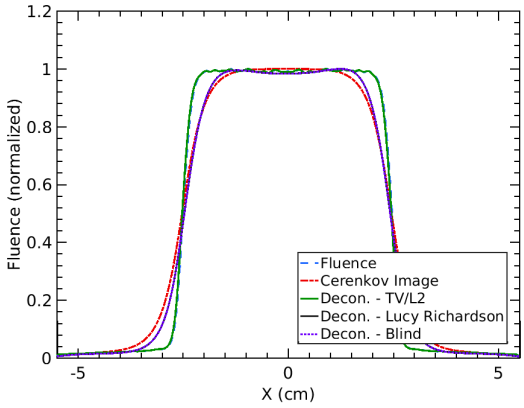

Figure 5.4: The cross-line profiles from a 6 MV 5x5 cm^2 open field on the flat optical phantom. Two comparison profiles are shown, the MC calculated primary beam fluence and a experimental Cerenkov photon image. These profiles were used to select the optimal deconvolution algorithm from three methods: Total Variation minimization (TV/L2), Lucy-Richardson, and Blind deconvolution. The TV/L2 was deemed most optimal, as it most closely matched the primary beam fluence.

5.4.2 Optimization of the Block-Deconvolution Method

Perturbation analysis was performed on Images (A) and (B) in Figure 5.2 to determine the most optimal block and margin sizes for space-variant deconvolution. It was found

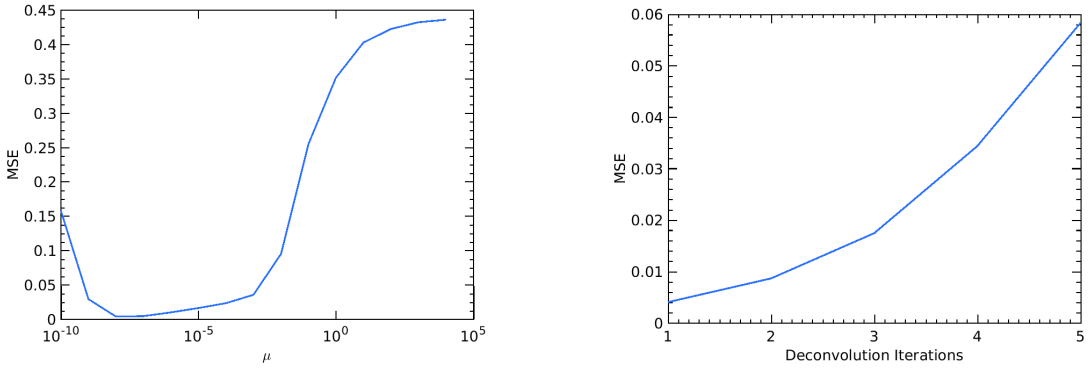

(a) (b)

Figure 5.5: The MSE calculated through perturbation of the parameter μ and number of iterations used in the TV/L2 deconvolution method. The MSE was found using a deconvolved 6 MV 5x5 cm^2 open field Cerenkov image compared against the primary beam fluence. (a) shows the perturbation of the parameter μ. (b) shows the MSE calculated when increasing the number of deconvolution iterations.

that there was no optimal block size - the block size had no discernible effect on either the MSE or the gamma passing rate when comparing the space-variant deconvolved image to the space-invariant deconvolved image. This result is to be expected for space-variant deconvolution using a single CSF. Space-variant deconvolution is driven by the need to deconvolve individual regions in an image with different kernels. This result shows that no artifacts arise in the process of dividing an image into partitions, deconvolving each partition individually, and stitching together the products. However, the use of smaller block sizes does lead to an increase in the computation time. Use of partitions that are 5% of the image width (400 total image partitions) had a computation time of 120 ms while using a 1% partition (10000 total image partitions) had a 3 s computation time.

Figure 5.6 shows results of perturbation of the margin size. In Figure 5.6(a), the margin size has been perturbed to determine the point at which there is no discernible effect on the space-variant deconvolved image in comparison to the space-invariant deconvolved image. A margin size of 22.9% of the image width is the threshold at which the space-variant deconvolved image has a 100% passing rate against the space-invariant deconvolved image. Figure 5.6(b) shows the MSE calculated under the same analysis. Here, a margin size of 42.9% of the full image width minimizes the error between the

space-variant and space-invariant deconvolved images. Figure 5.6(c) displays the increase in computation time as the margin size was increased. The curve follows an exponential trend, which is due to the quadratic increase in the total partition area as the margin size is expanded. There were no undesirable effects caused by including a margin which includes the full image or larger in deconvolution. Including at least the full image produced the most accurate result, only at the expense of computation time.

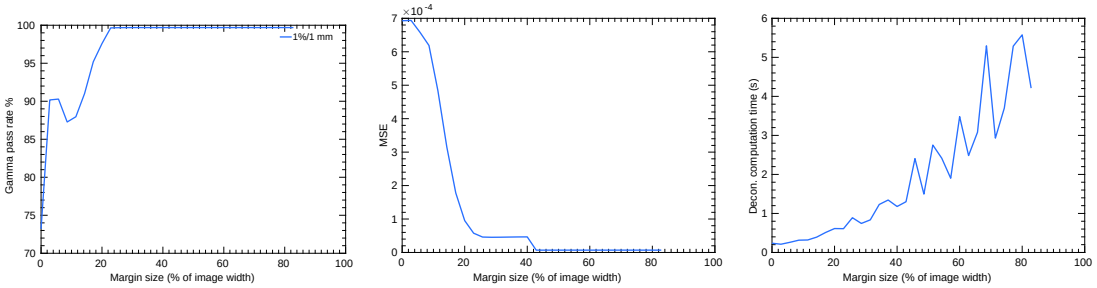

(a) (b) (c)

Figure 5.6: The effects of the margin size used for block-deconvolution of the composite image shown in Figure 5.2(A). The deconvolution results were compared with the true solution which was calculated by deconvolving the whole image without the partitioning. (a) shows the gamma passing rate (1%/1mm criteria). (b) shows the MSE under the same analysis. (c) displays the total computation time with an increasing partition margin size.

5.4.3 Space-Variant Deconvolution on a Curved Surface

Figure 5.7 shows the block-deconvolution process applied to a Cerenkov photon image of a curved surface. This image was partitioned into columns rather than square blocks, with the margin size set to include the full image. The X-direction of the image is with the curve of the phantom, so the CSF changes with the incident angle of the beam in the regions shown. The incident angle for each region was solved as the sum of the beam divergence and the curvature of the phantom using the known geometry. The left and right regions in the image represent an incident angle maximum of $\theta_{in} = +/-30°$. Each other region is a partitions of $\Delta\theta_{in} = +/-3°$ for the CSF angle, thus, the center represents an angle of $\theta_{in} = 0°$ with a total of 20 partitions in the image. The beam divergence also changes the rotation of the CSF within each strip. 40 partitions with

$\Delta\theta_{in} = +/-1.5°$ were also used.

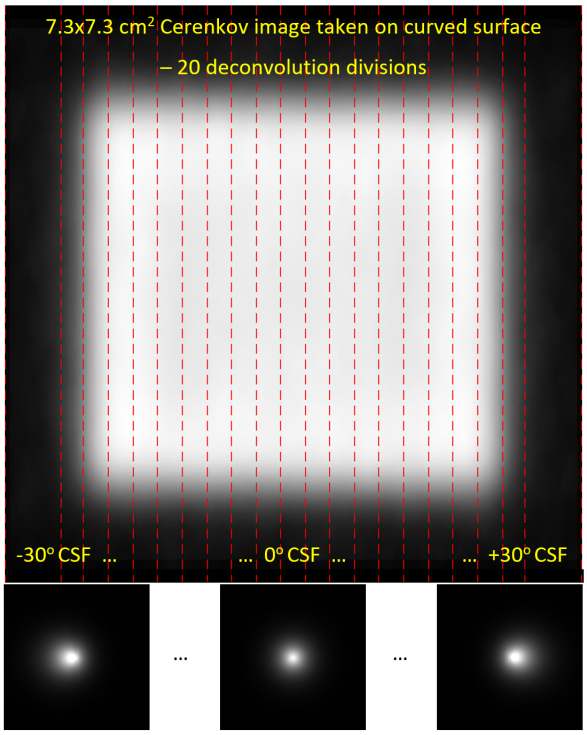

Figure 5.7: The 7.3x7.3 cm^2 Cerenkov photon image taken from the curved phantom surface after perspective correction and mapping to a flat surface. The red lines delineate the partitions used for space-variant deconvolution. Here, 20 regions are shown, each representing a unique CSF due to the incident beam angle changing throughout the image. On the left and right-most sides of the image, CSFs of $\theta_{in} = +/-30°$ are applied. Adjacent partitions change the CSF angle by $\Delta\theta_{in} = +/-3°$ such that a $\theta_{in} = 0°$ CSF is used in the center. The CSFs shown below are scaled to 75% of their original size. Although 20 partitions are shown here, 40 are also partitions with a CSF angle change of $\Delta\theta_{in} = +/-1.5°$ were also tested.

The space-variant images deconvolved with columns were compared against space-invariant deconvolved images using a single CSF with $\theta_{in} = 0°$. Figure 5.8 shows the cross-line profiles from a 7.3x7.3 cm^2 Cerenkov photon image taken from the curved phantom surface. Two deconvolution profiles are shown in this figure as solid lines - the profile of the space-variant deconvolved image (Decon. - SV Column) and the profile of the space-invariant deconvolved image (Decon. - SI). Two comparison profiles are shown in this figure as dashed lines - the Cerenkov photon image profile (Imaged)

and the fluence profile as determined through MC simulation (Fluence). As previously mentioned, the Cerenkov photon images required perspective correction through a coordinate transformation. As such, the X-direction coordinates shown in Figure 5.8 are in the direction of the phantom curvature. The fluence profiles in the X-direction required transformation from Cartesian coordinates to these same coordinates.

Figure 5.8(a) shows the cross-line profiles in the X-direction, along the surface curvature. Figure 5.8(b) displays an expanded view of the left-side of Figure 5.8(a). Table 5.1 contains the measurements of the field size and penumbra for all cross-line profiles shown in this figure. The Cerenkov photon image profile is wider than the fluence profile. This is to be expected as Cerenkov photons undergo scattering as they escape the phantom; the imaged profile represents a blurred form of the fluence profile. Space-invariant deconvolution using column partitions narrowed the penumbra region from 7.00 to 4.73 mm, but did not significantly change the field size measurement. The field size of the space-invariant deconvolved image is closer to that of the imaged profile than the fluence. On the other hand, space-variant deconvolution improved both the field size and the penumbra. Space-variant deconvolution improved measured field size in deconvolved images by 7.37%, as compared with 1.74% by space-invariant deconvolution. The error in the measured penumbra was 1.12 mm after space-variant deconvolution, as compared with 1.76 mm by space-invariant deconvolution. The measurements from the space-variant result are closer to that of the fluence profile than the imaged profile.

Figure 5.8(c) shows the cross-line profiles in the Y-direction. Table 5.1 contains the measurements of the field size and penumbra for all cross-line profiles shown in this figure. Similarly to Figure 5.8(a), the imaged profile is once again wider than both the fluence profile. However, here the effect of the CSF shape on the profile is shown more dramatically. The CSF used in space-variant deconvolution is more spread out in the X-direction than the Y-direction. This spreading is due to the change in angle of incidence from both the geometric curvature and the divergence of the radiation beam. In the Y-direction, the CSF shape is fairly uniform in every partition of the image. Physically, this represents a narrower diffusive spread of Cerenkov photons in the direction against the curve of the phantom. In deconvolution, the uniform shape of the CSF in the Y-direction caused the space-variant and space-invariant deconvolution profiles to be identical. Even though the CSF changes in the X-direction, this had no

effect on the Y-profile.

Figure 5.9 shows the cross-line profiles of additional field sizes in both the X and Y-directions for space-variant images deconvolved with columns. Table 5.2 displays the penumbra width error measurement for each field size in the X and Y-directions, as compared to the primary beam fluence. In all cases, the space-variant deconvolution result was superior to the space-invariant result.

In the previous chapter with space-invariant deconvolution applied to flat surfaces, we found that the incident angle should change by no more than 6° for the space-invariant assumption to remain valid [111]. At the edge of the 2x2 cm^2 field, the incident angle was calculated to be $\theta_{in} = 6.34°$. This angle lies just at the limitation found by the previous study [111]. Thus, for field sizes larger than 2x2 cm^2, we expect that gamma analysis with this criterion will result in a lower passing rate. To confirm this, we performed gamma analysis between the space-variant and space-invariant deconvolution results for the field sizes of 2x2 cm2, 4x4 cm2 ($\theta_{in} = 12.9°$), and 6x6 cm^2 ($\theta_{in} = 19.5°$). The gamma passing rates were 99.9%, 95.7%, and 74.4% for the 2x2 cm^2, 4x4 cm^2, and 6x6 cm^2 field sizes, respectively. These results show that space-variant deconvolution is necessary if the incident beam angle difference is larger than 6° between regions of an image.

Figure 5.10(a-b) shows the block-deconvolution method applied to the 7.3x7.3 cm^2 Cerenkov photon image taken from the curved phantom surface. For this method, the image was partitioned into a grid of 20x20 square blocks rather than columns. The margin size was still set to include the full image. The CSF angle and rotation within each block was determined using a histogram of the MC primary beam fluence and the known curvature of the phantom. Figure 5.10(a) shows a diagram of the CSF angle and rotation within each block. The CSF angle within each block was rounded to the nearest $\theta_{in} = 1.5°$, with a maximum angle of $\theta_{in} = 34.0°$ used at the edge of the image. Within each block, the CSF image was rotated to match the ϕ angle of the primary beam fluence.

Figure 5.10(b) shows the product of the block-deconvolution process. Figure 5.10(c) shows comparison of diagonal profiles of the deconvolved images. Four profiles are shown in this figure - the profile of the deconvolved image using block partitioning (Decon. - SV Block), the deconvolved image using column partitioning (Decon. - SV Column), the

Cerenkov photon image profile (Imaged), and the fluence profile (Fluence). Although the rotation of the CSF was considered in the block partitioning method, both of the deconvolved profiles appear similar. The dominant effect appears to be the CSF angle used in each partition rather than the kernel rotation.

Table 5.1: The field size and penumbra width measured from the cross-line profiles of the primary beam fluence, the Cerenkov photon image, the space-variant (SV) deconvolved image profiles, the space-invariant (SI) deconvolved image profile, and the selective space-variant (SSV) deconvolved image profile. These measurements were taken using the 7.3x7.3 cm^2 open field incident on the curved optical phantom. The error of each measurement, as compared to the fluence, is given in parenthesis.

Profile	Field - X (cm)	Field - Y (cm)	Pen. - X (mm)	Pen. - Y (mm)
Fluence (Ideal)	7.46	7.32	2.97	2.21
Imaged	8.07 (8.17%)	7.57 (3.42%)	7.00 (4.03)	7.97 (5.76)
Decon. - SV Column	7.52 (0.80%)	7.46 (0.19%)	4.09 (1.12)	5.62 (3.41)
Decon. - SV Block	7.53 (0.80%)	7.41 (0.12%)	4.06 (1.09)	5.45 (3.24)
Decon. - SI	7.94 (6.43%)	7.46 (0.19%)	4.73 (1.76)	5.61 (3.40)
Decon. - SSV	7.52 (0.80%)	-	4.09 (1.12)	-

Table 5.2: The measurements of the penumbra width error comparing deconvolution methods for various field sizes in both the X and Y-directions. The penumbra width error was calculated using the primary beam fluence and deconvolvion result for each field size. The space-variant (SV) deconvolution method used column paritioning. The space-invariant (SI) deconvolution method used a single CSF of $\theta_{in} = 0°$.

Decon. Method - Field Size	Penumbra Error - X	Penumbra Error - Y
SV - 2x2 cm^2	0.82 mm	3.03 mm
SI - 2x2 cm^2	1.09 mm	3.03 mm
SV - 4x4 cm^2	1.13 mm	3.08 mm
SI - 4x4 cm^2	1.29 mm	3.08 mm
SV - 6x6 cm^2	1.18 mm	3.20 mm
SI - 6x6 cm^2	1.73 mm	3.20 mm

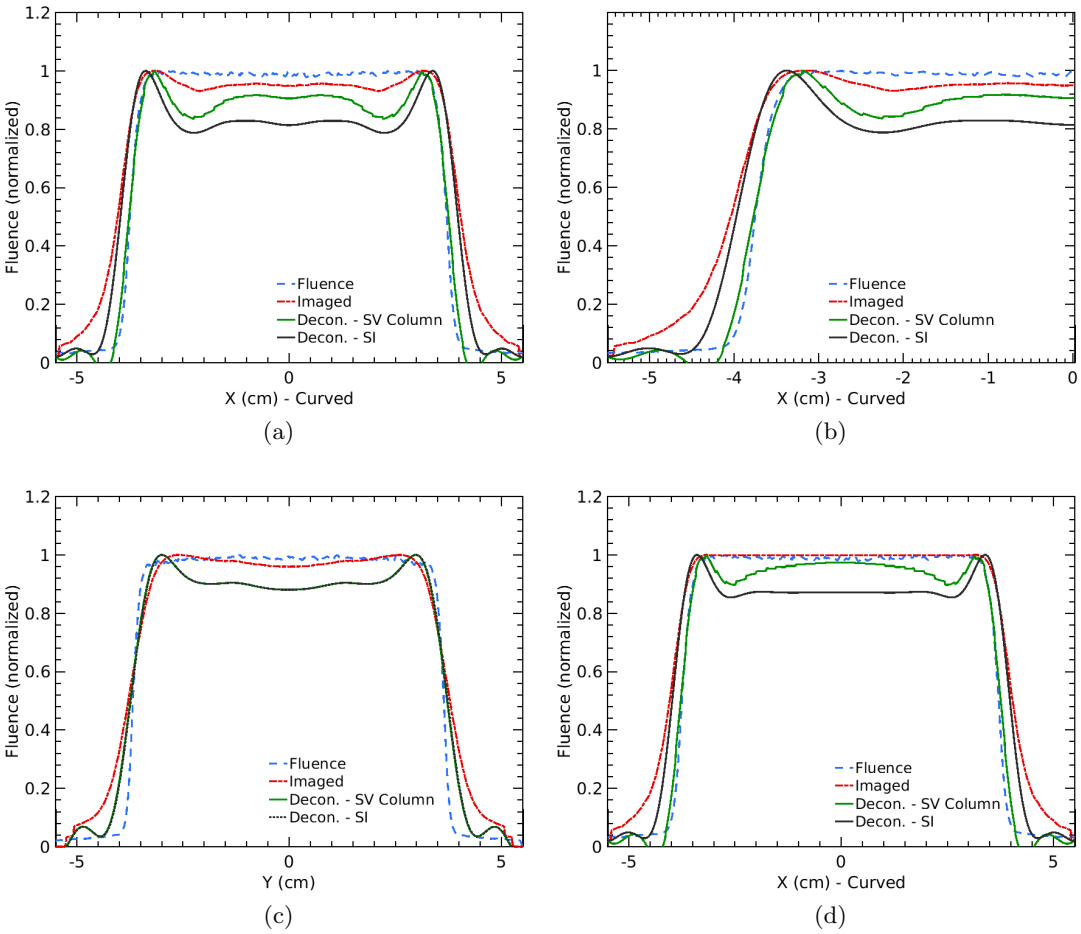

Figure 5.8: Cross-line profiles of the image created using space-variant deconvolution on the 7.3x7.3 cm^2 Cerenkov photon image taken from the curved phantom surface. The four curves are the primary incident beam fluence (Fluence), the raw Cerenkov photon image (Imaged), the space-variant devonvolved image (Decon. - SV), and the space-invariant deconvolved image (Decon. - SI). 40 blocks (or columns) were generated for the block-deconvolution similarly to Figure 5.7. (a) The cross-line profile of the X-direction. (b) An expanded view of the left side of (a). (c) The cross-line profile of the Y-direction. (d) Simulation of a DRDF correction across the central region of the beam. Here, a simulated Cerenkov radiance correction has been made, but fluctuations in the deconvolved profiles persist.

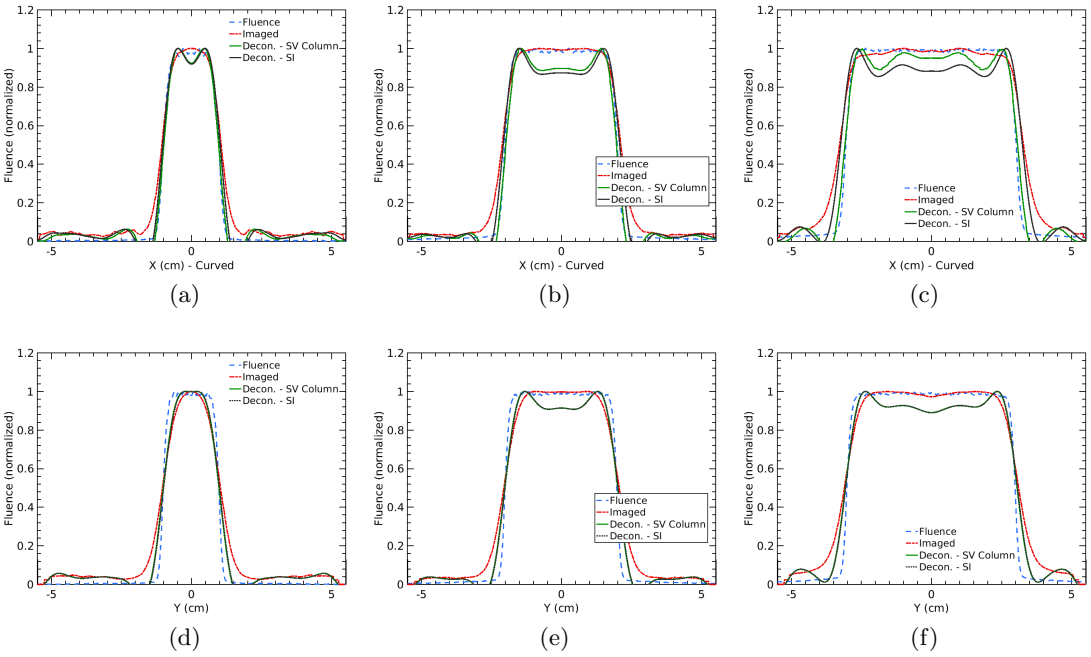

Figure 5.9: Cross-line profiles of the image created using space-variant deconvolution with column partitions on Cerenkov photon images taken from the curved phantom surface for various field sizes. (a) and (d) show a 2x2 cm^2 field size in the X and Y directions, respectively. (b) and (e) show a 4x4 cm^2 field size. (c) and (f) show a 6x6 cm^2 field size.

5.4.4 Selective Space-Variant Deconvolution

From the results of space-variant deconvolution on a curved surface image, it was clear that benefit was gained by this method for shrinking the width of the penumbra region for open field beams. This was particularly true for improving the penumbra measurement in the direction of the phantom curvature. However, within the center of the beam, the artifacts caused by deconvolution were amplified. This provided motivation for selective deconvolution in Cerenkov photon images, deconvolving only regions with a high intensity gradient to improve the correspondence to primary beam fluence. This type of deconvolution remains as space-variant; only selected regions of an image are deconvolved and the rest remain unaltered.

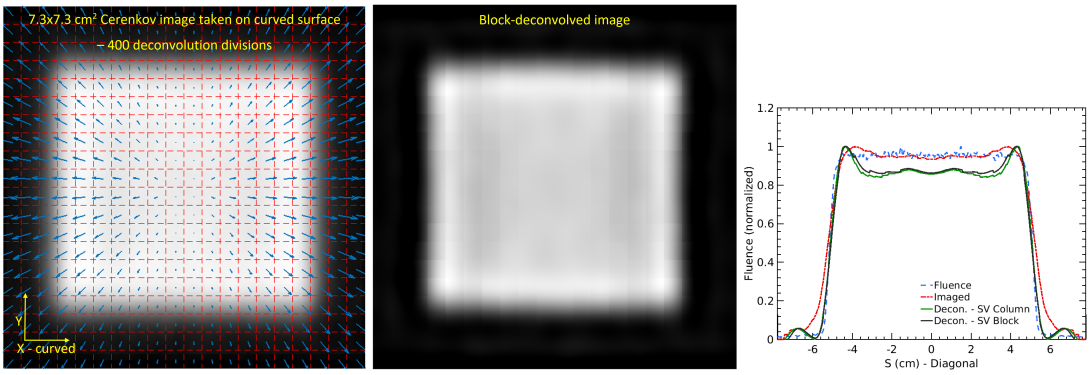

(a) (b) (c)

Figure 5.10: (a) The 7.3x7.3 cm^2 Cerenkov photon image taken from the curved phantom surface after perspective correction with 400 partitions shown with the red lines. In each partition, the CSF angle and rotation used in space-variant deconvolution is shown by the blue arrows. (b) The product of the block-deconvolution of (a). (c) The X-direction cross-line profile of the image shown in (b). The four curves are the primary incident beam fluence (Fluence), the raw Cerenkov photon image (Imaged), the space-variant devonvolved image (Decon. - SV Block), and the space-invariant deconvolved image (Decon. - SI). The Y-direction cross-line profile was nearly identical to that shown in Figure 5.8(c), and is not shown.

Selective deconvolution was performed on the 7.3x7.3 cm^2 experimental curved surface image. Seven regions on both the left and right sides of the image were hand-selected for space-variant deconvolution based upon the penumbra region visible in the image. The left and right-most regions were deconvolved by the $\theta_{in} = +/-30°$ CSFs. Adjacent regions used CSFs at increments of 1.5° such that the innermost CSFs were at $\theta_{in} = +/-21°$. The spacing of regions matched those used in the previous space-variant deconvolution of this image with 40 total partitions. An image of the regions chosen for the selective space-variant deconvolution is seen in Figure 5.11(a).

Figure 5.11(b) presents the X-direction cross-line profile of the selective space-variant deconvolved image in Figure 5.11(a). Here, a combination of various effects shown in Figure 5.8(a) are also observed. The penumbra in the deconvolved profile has been vastly improved over the imaged profile; furthermore, the intensity of the deconvolved profile matches that of the imaged profile in the central region of the beam. Selective deconvolution improved the field size from 8.07 cm to 7.53 cm, as compared to the

ideal fluence field size of 7.46 cm. Selective deconvolution also improved the penumbra measurement from 7.00 mm to 4.01 mm, as compared to the ideal fluence penumbra width of 2.97 mm. See also Table 5.1.

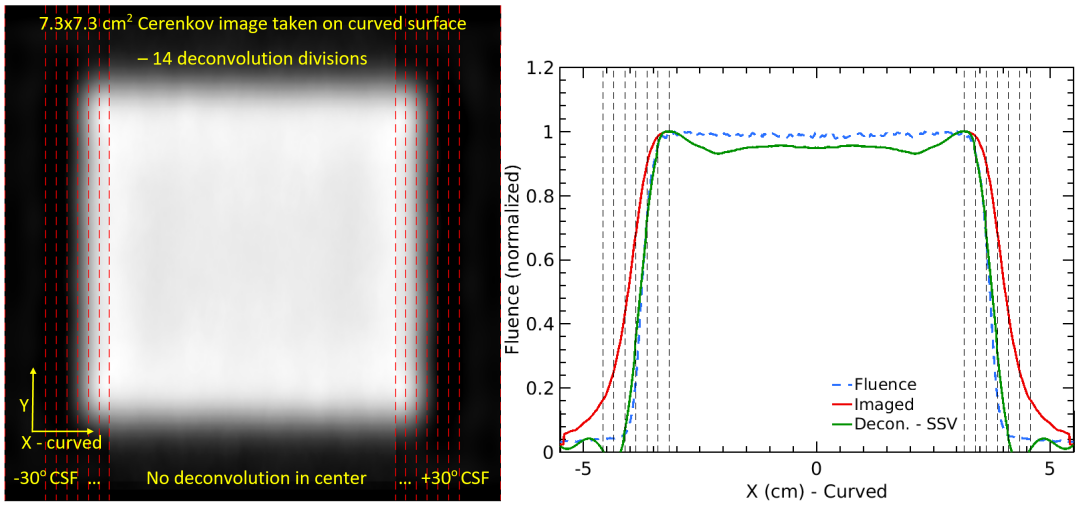

(a) (b)

Figure 5.11: A test of selective space-variant deconvolution on the 7.3x7.3 cm^2 Cerenkov photon image taken on the curved phantom surface. 7 partitions on both the left and right sides of the image were chosen to deconvolve the penumbra region of the beam, as shown with the dotted lines in both (a) and (b). The center of each deconvolution partition corresponds to non-normal CSF kernels ranging from $\theta_{in} = +/-21-30°$. The largest centermost region was unaltered and remained as the imaged profile. (a) The selectively deconvolved Cerenkov image. (b) The X-direction cross-line profile from (a). Here, selective deconvolution improved the correspondence of the Cerenkov profile to that of the fluence in the penumbra region and the center of the image remained unaltered.

5.5 Discussion

From the perturbation analysis of the margin size used in deconvolution, it was seen that a 22.9% margin and 42.9% margin resulted in a 100% gamma passing rate and 0 MSE, respectively. These percentages correspond to widths of 1.60 and 3.00 cm in the image coordinates. As previously shown, the CSF generally follows a triple-Gaussian distribution [111]. With respect to the CSF used in the perturbation study (a 6 MV

CSF of the optical phantom), the CSF distribution falls to 6.02% of its maximum value at a distance of 1.60 cm and 0.52% of the maximum value at 3.00 cm. The 6 MV CSF of the optical phantom has a FWHM of 5.01 mm, therefore, the 42.9% margin size corresponds to 6 times the FWHM of the CSF. This shows that selection of the margin and partition size used in block-deconvolution should be, in part, motivated by the shape of the scatter kernel used in the deconvolution step.

After analysis of the space-variant deconvolution parameters, it was determined that space-variant deconvolution of the curved surface images could use any block size and should include 100% of the image as a margin size. It should be noted that this application was not concerned with computation time; however, general applications of block-deconvolution may use a margin size that is at least 6 times the FWHM of the corresponding scattering kernel and limit the partition size based upon the number of unique scatter kernels present in the image.

In Chapter 3, the Lucy-Richardson deconvolution method was on all data. However, this method created undesirable artifacts at the edge of partitions when used in space-variant deconvolution, seen as jumps in the image amplitude. Blind deconvolution was also tested for space-variant deconvolution, yet yielded similar profiles to that of Lucy-Richardson. As seen in Figure 5.8, the TV/L2 deconvolution method yielded slight artifacts at the edge of partitions similar to that of the Lucy-Richardson deconvolution method, but smaller in magnitude. These artifacts are seen as the slight jumps throughout the Decon. - SV Column line. The artifacts were reduced by normalizing the $\theta_{in} > 0^{\circ}$ CSFs to the $\theta_{in} = 0^{\circ}$ CSF. The CSFs for $\theta_{in} > 0^{\circ}$ were larger in amplitude than the $\theta_{in} = 0^{\circ}$ CSF [111]. These artifacts may be further minimized using boundary conditions. As previously mentioned, the TV/L2 provided the best solution to deconvolution test cases on flat-images. In the case of a curved-image, it also provided the best solution, particularly in the X-direction.

In Figure 5.8(a), the beam divergence was taken into account during space-variant deconvolution whereas in Figure 5.8(c), it was not. As a consequence, the space-variant deconvolution profile shown in Figure 5.8(c) does not closely match the ideal penumbra shape given by the fluence profile. Here, space-variant deconvolution is limited by the accuracy of the scattering-kernels and delineation of regions. By not including beam-divergence in the Y-direction, the space-variant deconvolution result is no better than

space-invariant deconvolution with a single scatter kernel, the $\theta_{in} = 0°$ CSF. This result also is reflected in Tables 5.1 and 5.2, where the penumbra errors in the Y-direction are the same between space-variant and space-invariant deconvolution.

In Figure 5.8(a-c) and Figure 5.9, the profiles of raw Cerenkov image (or "Imaged") and deconvolved images all had fluctuations throughout the central region of the beam. In the imaged profile, this was likely due to effects related to the DRDF - the observed Cerenkov radiance changes with the angle of observation due to the curvature of the phantom. The variation in the central region of the beam was more dramatic in Figure 5.8(a), where the phantom curvature was present, than in Figure 5.8(c), where the phantom curvature was not present.

Figure 5.8(d) presents a scenario where the profile in the central region of the Cerenkov photon image was corrected for the dependence of the photon emission on the observation angle by using a DRDF discussed in [88]. After the correction along the X-axis, the imaged profile in the X-direction became flat as seen in the figure. For the 2D image, the correction was made by assigning a uniform value in the center of the image. Then, deconvolution was applied to the corrected image in the same manner as in Figure 5.8(a). Here, deconvolution created completely new fluctuations throughout the central region of the profile. This result is similar to those seen in Chapter 3, where horns were created at the edges of fields. However, the fluctuations generated by space-variant deconvolution do not follow the same pattern as those made by space-invariant deconvolution.

Evidence of the dependence of the observation angle on Cerenkov radiance was seen throughout this chapter. In the experimentally imaged profiles of Cerenkov photons captured from the curved phantom, the Cerenkov intensity varied throughout the center of the beam where it was expected to be flat. One possible explanation for this fluctuation is an inverse square effect. Due to the curvature of the phantom, less photons reach the camera sensor from irradiated points further away from the camera. However, it is clear that these fluctuations do not follow this behavior. The imaged intensity of Cerenkov photons in the central region of the beam shows horns at the edge of the field, indicating an increase in the Cerenkov radiance at points further away from the camera. The most likely explanation for this behavior lies in the directional radiance distribution function, as discussed in the previous paragraph. The Cerenkov radiance

does not follow a Lambertian pattern, but instead appears dependent upon the angle of observation.

The method of selective-deconvolution provided the best result for improving the penumbra and field width, while avoiding undesirable artifacts that arise in the flat uniform regions of the beam. However, at present, this method requires manual delineation of regions. Future work will examine methods by which regions of high-gradient can be automatically partitioned. One method that will be examined is the use of the image gradient, ∇I, and a qualifier, $g0$. Selective deconvolution with an angle-dependent CSF could be applied to a region of the image if $\nabla I > g0$.

This chapter used a commercial CMOS camera, which was incapable of knowing the full surface coordinates of the imaged phantom surface. Future work may wish to couple the Cerenkov imaging with a system capable of gathering the full 3D coordinates of the phantom so that a correction based upon the incident beam angle and the DRDF can be made automatically for space-variant deconvolution of captured images.

5.6 Conclusions

In this chapter, a space-variant deconvolution method for Cerenkov light dosimetry was developed. This method relied on the parameters of a block size and an added margin size. The optimal margin size was found to be at least 42.9% of the image width in all directions, which corresponded to 6 times the FHWM of the scatter kernel used in deconvolution. There was no optimal block size, but smaller partitions allowed for more segmentation of images with a trade-off in exponentially increasing the computation time. It was determined that Total Variation minimization (TV/L2) method for deconvolution provided the best solution to the Cerenkov imaging equation and was applied in space-variant deconvolution.

The space-variant deconvolution method was applied to Cerenkov photon images taken using an optical phantom with a curved front surface. The space-variant deconvolution improved the penumbra width and field size in the direction of the phantom curvature, but amplified existing fluctuations within the central region of the beam. Gamma analysis of images taken with different field sizes on the curved surface showed that space-variant deconvolution is necessary if the incident beam angle difference is

larger than 6° between regions of an image. Selective space-variant deconvolution improved the penumbra width and field size without modifying any other areas of the image. Moving forward, this is the recommended approach for deconvolution of Cerenkov photon images and motivates an automatic method for delineating regions that could be improved through deconvolution, such as the penumbra or other high-gradient regions.

Chapter 6

Summary and Future Work

6.1 Summary

This work explored the relationship between dose deposition, primary beam fluence, and Cerenkov light emission in external beam radiation therapy through a deconvolution formulation. Equations relating these physical terms were first derived in integral forms. These equations were then simplified into convolution kernels and the deconvolution relationships were shown. These equations relied on the assumption of space-invariance of the convolution kernels. Monte Carlo simulation was used to derive the convolution kernels for an optical phantom material, which was used to experimentally verify the deconvolution relationships. Deconvolution by a Cerenkov scatter function (CSF) was found to improve the correspondence between an image of Cerenkov light and Monte Carlo-derived dose, particularly in the penumbra region.

The CSF was then characterized for both the optical phantom and a layered skin model using Monte Carlo. Optical and radiological coefficients were derived for both the optical phantom and the layer skin model, which were used to find the CSF for different beam parameters. CSFs were solved from the results of the Monte Carlo simulations, and fit using a triple-Gaussian model. Fit coefficients were used in perturbation analysis to discover the errors introduced in the deconvolution product through use of an incorrect CSF. CSFs derived from skin models were found to be used interchangeably in deconvolution, with less than 1% error.

Lastly, the limitation of space-invariance was broken through derivation of a space-variant deconvolution equation for relating Cerenkov light and primary beam fluence. Space-variant deconvolution was applied to Cerenkov images from a curved surface. CSFs for non-normal beam angles were solved using Monte Carlo techniques. Space-variant deconvolution was performed in a block-process, where a portion of the image was deconvolved and then stitched back into its original location. Space-variant deconvolution was found to improve the Cerenkov image to beam fluence correspondence even further than space-invariant deconvolution. In particular, the penumbra region of the images was greatly improved through space-variant deconvolution. Selective space-variant deconvolution was found to provide the most accurate solution to the deconvolution formulation in a practical scenario.

6.2 Future Work

This work shows potential for improving the current methods employed for imaging of Cerenkov light in radiation therapy. Many current applications focus on the use of imaging Cerenkov light, but do not yet apply deconvolution to relate an image to either dose deposition or the primary beam fluence. The labeling of an Cerenkov light image as an image of radiation dose is misleading; it is strictly an image of Cerenkov photons. However, this completed work did not focus on application of the deconvolution techniques to images taken in vivo during patient treatment. A first step for future work is application of these deconvolution techniques to images taken in vivo during an external beam radiation treatment. This step would build guidelines by with others in the field could follow for applying the deconvolution formulation.

Another concern from this work is that of necessity. In practice, it is difficult to derive and apply CSFs to images of Cerenkov light. These corrections were found to matter most when the field was highly varying, containing regions of high dose gradient. As it stands, deconvolution is useful and necessary when imaging Cerenkov light from a phantom material, but validation of the formulation from in vivo images is necessary to determine the true practicality of this technique. Optical diffusion was found to play a larger role in phantom materials than in the layered skin models.

From Chapter 5, it was shown that space-variant deconvolution is the most promising application of this completed work. Hence, in this study we used a phantom with a known geometry so that we could analytically determine the CSF specific to the curvature at each location. For in vivo images collected from a patients skin surface, the geometry will have to be known prior to application of space-variant deconvolution. This goal may be achieved by coupling the Cerenkov imaging system to a camera system capable of determining the coordinates of the patient geometry. Multiple camera systems exist for patient set-up and geometry determination in radiation therapy, including the C-RAD Catalyst (Stockholm, Sweden) and VisionRT AlignRT (London, UK) systems. Extending the use of these systems to imaging Cerenkov light is a non-trivial process, but would allow for proper application of space-variant deconvolution to Cerenkov images.

Once it is possible to couple both the patient surface geometry and the Cerenkov imaging systems, multiple avenues of research can be fully realized. First, the space-variant deconvolution shown in this work was performed largely in just one dimension in the Cerenkov images. In Chapter 5, the block partitioning method performed only slightly better than the column partitioning method. However, partitioning images in both directions may be strictly necessary for in vivo patient images. The limitations of the formula will have to be tested in a more complex geometry. Second, selective space-variant deconvolution was performed using manual determination of image partitions. One avenue of research exists in automatic delineation of regions of high dose gradient in Cerenkov images for application of selective deconvolution. Third, the data presented in Chapter 5 showed evidence of a dependence on observed Cerenkov intensity as a function of the angle of observation. This was called as the direction radiance distribution function (DRDF). With a system capable of determining a patient's surface geometry, accounting for the DRDF through a correction factor would become possible.

Lastly, the largest benefit that this work may provide to radiation therapy remains largely unexplored. This completed work showed the relationship that exists between Cerenkov light and primary beam fluence, but use of the primary beam fluence in secondary applications was not shown. It is well known that primary beam fluence can be related to dose deposition in a medium. This relationship was used, in part, to find the two-dimensional dose delivered to a plane shown in Chapter 3. However, this idea can

be extended towards three-dimensional dose calculations. This technique is largely applied by treatment planning systems using convolution-superposition algorithms. With a system capable of collecting both Cerenkov light and determining the patient geometry, space-variant deconvolution may be capable of solving for the primary beam fluence delivered in vivo. This type of system may allow for in vivo verification of the full three-dimension dose delivered to a patient.

References

[1] Faiz M. Khan. *Khan's the physics of radiation therapy.* Lippincott Williams and Wilkins/Wolters Kluwer, Philadelphia, PA, fifth edition, 2014.

[2] Ervin B Podgorsak. *Radiation Physics for Medical Physicists.* Biological and Medical Physics, Biomedical Engineering. Springer, Berlin, Heidelberg, first edition, 2006.

[3] Pedro Arce, Juan Ignacio Lagares, Laura Harkness, Daniel Prez-Astudillo, Mario Caadas, Pedro Rato, Mara de Prado, Yamiel Abreu, Gianluca de Lorenzo, Machiel Kolstein, and Angelina Daz. Gamos: A framework to do geant4 simulations in different physics fields with an user-friendly interface. *Nuclear Instruments and Methods in Physics Research*, 735:304–313, January 2014.

[4] Adam K Glaser, Rongxiao Zhang, David J Gladstone, and Brian W Pogue. Optical dosimetry of radiotherapy beams using Cherenkov radiation: the relationship between light emission and dose. *Physics in Medicine and Biology*, 59(14):3789–3811, July 2014.

[5] R. H. Bradbury and P. Angibaud. *Cancer.* Topics in medicinal chemistry. Springer, Berlin, first edition, 2007.

[6] International Agency for Research on Cancer. Latest global cancer data: Cancer burden rises to 18.1 million new cases and 9.6 million cancer deaths in 2018. Press Release, September 2018.

[7] O Klein and Y Nishina. Uber die streuung von strahlung durch freie elektronen nach der neuen relativistischen quantendynamik von dirac. *Zeitschrift fur Physik*, 52(11-12):853–869, 1929.

[8] Eric E. Klein, Joseph Hanley, John Bayouth, FangFang Yin, William Simon, Sean Dresser, Christopher Serago, Francisco Aguirre, Lijun Ma, Bijan Arjomandy, Chihray Liu, Carlos Sandin, and Todd Holmes. Task group 142 report: Quality assurance of medical acceleratorsa. *Medical Physics*, 36(9):4197–4212, 2009.

[9] A. S. Beddar, T. R. Mackie, and F. H. Attix. Water-equivalent plastic scintillation detectors for high-energy beam dosimetry: I. physical characteristics and theoretical consideration. *Phys Med Biol*, 37(10):1883–900, 1992.

[10] K. Yogo, Y. Tatsuno, M. Tsuneda, Y. Aono, D. Mochizuki, Y. Fujisawa, A. Matsushita, M. Ishigami, H. Ishiyama, and K. Hayakawa. Practical use of a plastic scintillator for quality assurance of electron beam therapy. *Physics in Medicine and Biology*, 62(11):4551–4570, 2017.

[11] Arash Darafsheh, Rongxiao Zhang, Stephen Chad Kanick, Brian W Pogue, and Jarod C Finlay. Spectroscopic separation of cerenkov radiation in high-resolution radiation fiber dosimeters. *Journal of Biomedical Optics*, 20(9):095001–095001, 2015.

[12] P. Papaconstadopoulos, L. Archambault, and J. Seuntjens. Experimental investigation on the accuracy of plastic scintillators and of the spectrum discrimination method in small photon fields. *Med Phys*, 44(2):654–664, 2017.

[13] L J Schreiner, T Olding, and K B McAuley. Polymer gel dosimetry. *Journal of Physics: Conference Series*, 250(1), 2010.

[14] H. Helen Liu, T. Rock Mackie, and Edwin C. Mccullough. A dual source photon beam model used in convolution/superposition dose calculations for clinical megavoltage xray beams. *Medical Physics*, 24(12):1960–1974, December 1997.

[15] Steve Webb. *The physics of three-dimensional radiation therapy*, chapter 2.5, pages 87–101. Institute of Physics Publishing, Bristol, 1993.

[16] P Arce, J. I Lagares, L Harkness, L Desorgher, G de Lorenzo, Y Abreu, and Zhentian Wang. Gamos: An easy and flexible way to use geant4. In *2011 IEEE Nuclear Science Symposium Conference Record*, pages 2230–2237. IEEE, 2011.

[17] Pedro Arce, Pedro Rato, Mario Canadas, and Juan Ignacio Lagares. Gamos: A geant4-based easy and flexible framework for nuclear medicine applications. In *2008 IEEE Nuclear Science Symposium Conference Record*, pages 3162–3168. IEEE, 2008.

[18] Adam K Glaser, Stephen C Kanick, Rongxiao Zhang, Pedro Arce, and Brian W Pogue. A gamos plug-in for geant4 based monte carlo simulation of radiation-induced light transport in biological media. *Biomedical Optics Express*, 4(5), May 2013.

[19] P. A. Cerenkov. Visible radiation produced by electrons moving in a medium with velocities exceeding that of light. *Phys. Rev.*, 52:378–379, Aug 1937.

[20] P. A. Cerenkov. Visible emission of clean liquids by action of γ radiation. *Doklady Akademii Nauk SSSR*, 2, 1934.

[21] I.E. Tamm and I.M. Frank. Coherent radiation of fast electrons in a medium. *Doklady Akademii Nauk SSSR*, 14, 1937.

[22] BW Pogue, R Zhang, A Glaser, JM Andreozzi, P Bruza, DJ Gladstone, and LA Jarvis. Cherenkov imaging in the potential roles of radiotherapy qa and delivery. In *Journal of Physics: Conference Series*, volume 847, page 012046. IOP Publishing, 2017.

[23] J. Andreozzi, K. Mooney, P. Bruza, A. Curcuru, S. Saunders, D. Gladstone, B. Pogue, and O. Green. Tu-ab-bra-12: Quality assurance of an integrated magnetic resonance image guided adaptive radiotherapy machine using Cherenkov imaging. *Med Phys*, 43(6):3736, 2016.

[24] J. M. Andreozzi, R. Zhang, D. J. Gladstone, B. B. Williams, A. K. Glaser, B. W. Pogue, and L. A. Jarvis. Cherenkov imaging method for rapid optimization of clinical treatment geometry in total skin electron beam therapy. *Med Phys*, 43(2):993–1002, 2016.

[25] A. K. Glaser, S. C. Davis, D. M. McClatchy, R. Zhang, B. W. Pogue, and D. J. Gladstone. Projection imaging of photon beams by the Cerenkov effect. *Med Phys*, 40(1):012101, 2013.

[26] A. K. Glaser, W. H. Voigt, S. C. Davis, R. Zhang, D. J. Gladstone, and B. W. Pogue. Three-dimensional Cerenkov tomography of energy deposition from ionizing radiation beams. *Opt Lett*, 38(5):634–6, 2013.

[27] Yusuf Helo, Rosenberg Ivan, DSouza Derek, MacDonald Lindsay, Speller Robert, Royle Gary, and Gibson Adam. Imaging Cerenkov emission as a quality assurance tool in electron radiotherapy. *Physics in Medicine and Biology*, 59(8):1963, 2014.

[28] Y. Roussakis, R. Zhang, G. Heyes, G. Webster, S. Mason, S. Green, B. Pogue, and H. Dehghani. Real-time Cherenkov emission portal imaging during cyberknife radiotherapy. *Phys Med Biol*, 60(22):N419–25, 2015.

[29] R. Zhang, J. M. Andreozzi, D. J. Gladstone, W. L. Hitchcock, A. K. Glaser, S. Jiang, B. W. Pogue, and L. A. Jarvis. Cherenkoscopy based patient positioning validation and movement tracking during post-lumpectomy whole breast radiation therapy. *Phys Med Biol*, 60(1):L1–14, 2015.

[30] P. Bruza, J. M. Andreozzi, D. J. Gladstone, L. A. Jarvis, J. Rottmann, and B. W. Pogue. Online combination of EPID & Cherenkov imaging for 3-d dosimetry in a liquid phantom. *IEEE Transactions on Medical Imaging*, 36(10):2099–2103, 2017.

[31] Rongxiao Zhang, Alisha V D'Souza, Jason R Gunn, Tatiana V Esipova, Sergei A Vinogradov, Adam K Glaser, Lesley A Jarvis, David J Gladstone, and Brian W Pogue. Cherenkov-excited luminescence scanned imaging. *Optics letters*, 40(5), 2015.

[32] Yiannis Roussakis, Rongxiao Zhang, Geoff Heyes, Gareth Webster, Suzannah Mason, Stuart Green, Brian Pogue, and Hamid Dehghani. Real-time cherenkov emission portal imaging during cyberknife radiotherapy. *Physics in medicine and biology*, 60(22), 2015.

[33] Syed Rakin Ahmed, Jeremy Mengyu Jia, Petr Bruza, Sergei Vinogradov, Shudong Jiang, David J Gladstone, Lesley A Jarvis, and Brian W Pogue. Radiotherapy-induced cherenkov luminescence imaging in a human body phantom. *Journal of Biomedical Optics*, 23(3):030504–030504, 2018.

[34] Jacqueline M. Andreozzi, Karen E. Mooney, Petr Bruza, Austen Curcuru, David J. Gladstone, Brian W. Pogue, and Olga Green. Remote cherenkov imagingbased quality assurance of a magnetic resonance imageguided radiotherapy system. *Medical Physics*, 45(6):2647–2659, 2018.

[35] Adam K. Glaser, Jacqueline M. Andreozzi, Rongxiao Zhang, Brian W. Pogue, and David J. Gladstone. Optical cone beam tomography of cherenkovmediated signals for fast 3d dosimetry of xray photon beams in water. *Medical Physics*, 42(7):4127–4136, 2015.

[36] Brian Pogue. Cherenkov imaging of radiation dose and molecular signaling in vivo. *Biophysical Journal*, 110(3):196a–197a, 2016.

[37] Alisha Dsouza, Huiyun Lin, Jason R. Gunn, David J. Gladstone, Lesley A. Jarvis, and Brian W. Pogue. Cherenkov-excited multi-fluorophore sensing in tissue-simulating phantoms and in vivo from external beam radiotherapy.(report). *Radiation Research*, 189(2), 2018.

[38] Clare Snyder, Brian W Pogue, Michael Jermyn, Irwin Tendler, Jacqueline M Andreozzi, Petr Bruza, Venkat Krishnaswamy, David J Gladstone, and Lesley A Jarvis. Algorithm development for intrafraction radiotherapy beam edge verification from cherenkov imaging. *Journal of Medical Imaging*, 5(1), 2018.

[39] Mengyu Jeremy Jia, Petr Bruza, Lesley A Jarvis, David J Gladstone, and Brian W Pogue. Multi-beam scan analysis with a clinical linac for high resolution cherenkov-excited molecular luminescence imaging in tissue. *Biomedical optics express*, 9(9), 2018.

[40] Tianshun Miao, Petr Bruza, Brian W Pogue, Michael Jermyn, Venkataramanan Krishnaswamy, William Ware, Frank Rafie, David J Gladstone, and Benjamin B

Williams. Cherenkov imaging for linac beam shape analysis as a remote electronic quality assessment verification tool. *Medical physics*, 46(2), 2018.

[41] Rongxiao Zhang, Scott C Davis, Jennifer-Lynn H Demers, Adam K Glaser, David J Gladstone, Tatiana V Esipova, Sergei A Vinogradov, and Brian W Pogue. Oxygen tomography by cerenkov-excited phosphorescence during external beam irradiation. *Journal of Biomedical Optics*, 18(5):050503–050503, 2013.

[42] Huiyun Lin, Rongxiao Zhang, Jason R Gunn, Tatiana V Esipova, Sergei Vinogradov, David J Gladstone, Lesley A Jarvis, and Brian W Pogue. Comparison of cherenkov excited fluorescence and phosphorescence molecular sensing from tissue with external beam irradiation. *Physics in medicine and biology*, 61(10), 2016.

[43] Rongxiao Zhang, Adam Glaser, Tatiana V Esipova, Stephen C Kanick, Scott C Davis, Sergei Vinogradov, David Gladstone, and Brian W Pogue. Cerenkov radiation emission and excited luminescence (crel) sensitivity during external beam radiation therapy: Monte carlo and tissue oxygenation phantom studies. *Biomedical optics express*, 3(10), 2012.

[44] Jacqueline M. Andreozzi, Petr Bruza, Irwin I. Tendler, Karen E. Mooney, Lesley A. Jarvis, Jochen Cammin, Harold Li, Brian W. Pogue, and David J. Gladstone. Improving treatment geometries in total skin electron therapy: Experimental investigation of linac angles and floor scatter dose contributions using cherenkov imaging. *Medical Physics*, 45(6):2639–2646, 2018.

[45] Rachael Hachadorian, Petr Bruza, Michael Jermyn, Amaan Mazhar, David Cuccia, Lesley Jarvis, David Gladstone, and Brian Pogue. Correcting cherenkov light attenuation in tissue using spatial frequency domain imaging for quantitative surface dosimetry during whole breast radiation therapy. *Journal of biomedical optics*, 24(7), 2018.

[46] Yunhe Xie, Heather Petroccia, Amit Maity, Tianshun Miao, Yihua Zhu, Petr Bruza, Brian W Pogue, Jacqueline M Andreozzi, John P Plastaras, Lei Dong, et al. Cherenkov imaging for total skin electron therapy (tset). In *Molecular-Guided Surgery: Molecules, Devices, and Applications IV*, volume 10478, page 1047816. International Society for Optics and Photonics, 2018.

[47] X. Mei, J. A. Rowlands, and G. Pang. Electronic portal imaging based on cerenkov radiation: A new approach and its feasibility. *Medical Physics*, 33(11):4258–4270, 2006.

[48] Yusuf Helo, Ivan Rosenberg, Derek DSouza, Lindsay MacDonald, Robert Speller, Gary Royle, and Adam Gibson. Imaging cerenkov emission as a quality assurance tool in electron radiotherapy. *Physics in Medicine and Biology*, 59(8):1963–1978, 2014.

[49] Y Helo, A Kacperek, I Rosenberg, G Royle, and A P Gibson. The physics of cerenkov light production during proton therapy. *Physics in Medicine and Biology*, 59(23):7107–7123, 2014.

[50] Kyoung Won Jang, Sang Hun Shin, Seon Geun Kim, Jae Seok Kim, Wook Jae Yoo, Young Hoon Ji, and Bongsoo Lee. Measurement of cerenkov radiation induced by the gamma-rays of co-60 therapy units using wavelength shifting fiber. *Sensors*, 14(4), 2014.

[51] Adam K Glaser, Rongxiao Zhang, Jacqueline M Andreozzi, David J Gladstone, and Brian W Pogue. Cherenkov radiation fluence estimates in tissue for molecular imaging and therapy applications. *Physics in Medicine and Biology*, 60(17):6701–6718, 2015.

[52] Petr Bruza, Jacqueline M Andreozzi, David J Gladstone, Lesley A Jarvis, Joerg Rottmann, and Brian W Pogue. Online combination of epid & cherenkov imaging for 3-d dosimetry in a liquid phantom. *IEEE Transactions on Medical Imaging*, 36(10):2099–2103, 2017.

[53] Johan Axelsson, Adam K. Glaser, David J. Gladstone, and Brian W. Pogue. Quantitative cherenkov emission spectroscopy for tissue oxygenation assessment. *Optics Express*, 20(5):5133–5142, 2012.

[54] Robert W Holt, Rongxiao Zhang, Tatiana V Esipova, Sergei A Vinogradov, Adam K Glaser, David J Gladstone, and Brian W Pogue. Cherenkov excited phosphorescence-based po 2 estimation during multi-beam radiation therapy:

phantom and simulation studies. *Physics in Medicine and Biology*, 59(18):5317–5328, 2014.

[55] Rongxiao Zhang, Adam K. Glaser, Jacqueline Andreozzi, Shudong Jiang, Lesley A. Jarvis, David J. Gladstone, and Brian W. Pogue. Beam and tissue factors affecting Cherenkov image intensity for quantitative entrance and exit dosimetry on human tissue. *Journal of Biophotonics*, 10(5):645–656, May 2017.

[56] Diyun Shu, Xiaobin Tang, Changran Geng, Chunhui Gong, and Da Chen. Determination of the relationship between dose deposition and Cerenkov photons in homogeneous and heterogeneous phantoms during radiotherapy using monte carlo method. *Journal of Radioanalytical and Nuclear Chemistry*, 308(1):187–193, April 2016.

[57] Adam K Glaser, William H A Voigt, Scott C Davis, Rongxiao Zhang, David J Gladstone, and Brian W Pogue. Three-dimensional cerenkov tomography of energy deposition from ionizing radiation beams. *Optics letters*, 38(5), 2013.

[58] Xu Cao, Shudong Jiang, Mengyu Jeremy Jia, Jason R Gunn, Tianshun Miao, Scott C Davis, Petr Bruza, and Brian W Pogue. Cherenkov excited short-wavelength infrared fluorescence imaging in vivo with external beam radiation. *Journal of biomedical optics*, 24(5), 2018.

[59] Esther Ciarrocchi and Nicola Belcari. Cerenkov luminescence imaging: physics principles and potential applications in biomedical sciences. *EJNMMI Physics*, 4(1):1–31, December 2017.

[60] Kaveh Tanha, Ali Mahmoud Pashazadeh, and Brian W Pogue. Review of biomedical cerenkov luminescence imaging applications. *Biomedical optics express*, 6(8), 2015.

[61] Katsunori Yogo, Yuya Tatsuno, Masato Tsuneda, Yuki Aono, Daiki Mochizuki, Yoshiki Fujisawa, Akihiro Matsushita, Minoru Ishigami, Hiromichi Ishiyama, and Kazushige Hayakawa. Practical use of a plastic scintillator for quality assurance of electron beam therapy. *Physics in Medicine and Biology*, 62(11):4551–4570, 2017.

[62] J. Archer, E. Li, M. Petasecca, M. Lerch, A. Rosenfeld, and M. Carolan. High-resolution fiber-optic dosimeters for microbeam radiation therapy. *Med Phys*, 44(5):1965–1968, 2017.

[63] A. S. Beddar, T. R. Mackie, and F. H. Attix. Water-equivalent plastic scintillation detectors for high-energy beam dosimetry: Ii. properties and measurements. *Phys Med Biol*, 37(11):1901–1913, 1992.

[64] E. Burke, D. Poppinga, A. A. Schonfeld, D. Harder, B. Poppe, and H. K. Looe. The practical application of scintillation dosimetry in small-field photon-beam radiotherapy. *Z Med Phys*, 27(4):324–333, 2017.

[65] M Rilling, M Goulet, S Thibault, and L Archambault. Towards an optimized 3d scintillation dosimetry tool for quality assurance of dynamic radiotherapy techniques. *Medical Physics*, 42(6):3206–3206, 2015.

[66] P Z Y Liu, N Suchowerska, J Lambert, P Abolfathi, and D R McKenzie. Plastic scintillation dosimetry: comparison of three solutions for the cerenkov challenge. *Physics in Medicine and Biology*, 56(18):5805–5821, 2011.

[67] Daniel Robertson, Cheukkai Hui, Louis Archambault, Radhe Mohan, and Sam Beddar. Optical artefact characterization and correction in volumetric scintillation dosimetry. *Physics in Medicine and Biology*, 59(1):23–42, 2014.

[68] S Beddar. Real-time volumetric scintillation dosimetry. In *Journal of Physics: Conference Series*, volume 573, page 012005. IOP Publishing, 2015.

[69] Mathieu Goulet, Madison Rilling, Luc Gingras, Sam Beddar, Luc Beaulieu, and Louis Archambault. Novel, full 3d scintillation dosimetry using a static plenoptic camera. *Medical Physics*, 41(8), 2014.

[70] L Beaulieu, M Goulet, L Archambault, and S Beddar. Current status of scintillation dosimetry for megavoltage beams. In *Journal of Physics: Conference Series*, volume 444, page 012013. IOP Publishing, 2013.

[71] M. A. Mosleh-Shirazi, W. Swindell, and P. M. Evans. Optimization of the scintillation detector in a combined 3d megavoltage ct scanner and portal imager. *Medical Physics*, 25(10):1880–1890, 1998.

[72] Louis Archambault, Tina M. Briere, and Falk Poenisch. Toward a real-time in vivo dosimetry system using plastic scintillation detectors. *International Journal of Radiation Oncology, Biology and Physics*, 78(1), 2010.

[73] A Sam Beddar. Plastic scintillation dosimetry: optimization of light collection efficiency. *Physics in Medicine and Biology*, 48(9):1141–1152, 2003.

[74] S Beddar and L Beaulieu. Plastic scintillation detectors: Present status and their application for quality assurance and in vivo dosimetry. *Medical Physics*, 40(6), 2013.

[75] A.B. Hwang, J. Chen, E. Kinsey, B.L. Fowble, N.R. Schechter, C.C. Park, A. Bevan, and P. Xia. Effect of photon energy on superficial dose in the treatment of breast cancer with tangent fields. *International Journal of Radiation Oncology, Biology, Physics*, 75(3):S224–S225, 2009.

[76] Nesrin Dogan and Glenn P. Glasgow. Surface and buildup region dosimetry for obliquely incident intensity modulated radiotherapy 6 mv x rays. *Medical Physics*, 30(12):3091–3096, December 2003.

[77] Lukkana Apipunyasopon, Somyot Srisatit, and Nakorn Phaisangittisakul. An investigation of the depth dose in the build-up region, and surface dose for a 6 mv therapeutic photon beam: Monte carlo simulation and measurements. *Journal of Radiation Research*, 54(2):374–382, March 2013.

[78] Mark J. Ashburner and Samuel Tudor. The optimization of superficial planning target volumes (ptvs) with helical tomotherapy. *Journal of Applied Clinical Medical Physics*, 15(6):4–12, November 2014.

[79] Qi Zhenyu, Deng Xiaowu, Huang Shaomin, Zhang Li, He Zhichun, X. Allen Li, Ian Kwan, Michael Lerch, Dean Cutajar, Peter Metcalfe, and Anatoly Rosenfeld. In vivo verification of superficial dose for head and neck treatments using intensity-modulated techniques. *Medical Physics*, 36(1), 2009.

[80] P. D. Higgins, E. Y. Han, J. L. Yuan, S. Hui, and C. K. Lee. Evaluation of surface and superficial dose for head and neck treatments using conventional or intensity-modulated techniques. *Physics in Medicine and Biology*, 52(4):1135–1146, February 2007.

[81] Olivier Blasi, Jonas D Fontenot, Robert S Fields, John P Gibbons, and Kenneth R Hogstrom. Preliminary comparison of helical tomotherapy and mixed beams of unmodulated electrons and intensity modulated radiation therapy for treating superficial cancers of the parotid gland and nasal cavity. *Radiation oncology (London, England)*, 6, December 2011.

[82] Yuichi Akino, Indra J. Das, Gregory K. Bartlett, Hualin Zhang, Elizabeth Thompson, and Jennifer E. Zook. Evaluation of superficial dosimetry between treatment planning system and measurement for several breast cancer treatment techniques. *Medical Physics*, 40(1), January 2013.

[83] Lesley A. Jarvis, Rongxiao Zhang, David J. Gladstone, Shudong Jiang, Whitney Hitchcock, Oscar D. Friedman, Adam K. Glaser, Michael Jermyn, and Brian W. Pogue. Cherenkov video imaging allows for the first visualization of radiation therapy in real time. *International Journal of Radiation Oncology, Biology, Physics*, 89(3):615–622, July 2014.

[84] Rongxiao Zhang, Adam K. Glaser, David J. Gladstone, Colleen J. Fox, and Brian W. Pogue. Superficial dosimetry imaging based on Cerenkov emission for external beam radiotherapy with megavoltage xray beam. *Medical Physics*, 40(10):101914, October 2013.

[85] A. K. Glaser, J. M. Andreozzi, S. C. Davis, R. Zhang, B. W. Pogue, C. J. Fox, and D. J. Gladstone. Video-rate optical dosimetry and dynamic visualization of imrt and vmat treatment plans in water using Cherenkov radiation. *Med Phys*, 41(6):062102, 2014.

[86] R. Zhang, D. J. Gladstone, L. A. Jarvis, R. R. Strawbridge, P. Jack Hoopes, O. D. Friedman, A. K. Glaser, and B. W. Pogue. Real-time in vivo cherenkoscopy imaging during external beam radiation therapy. *J Biomed Opt*, 18(11):110504, 2013.

[87] Rongxiao Zhang, Colleen J Fox, Adam K Glaser, David J Gladstone, and Brian W Pogue. Superficial dosimetry imaging of Cerenkov emission in electron beam radiotherapy of phantoms. *Physics in Medicine and Biology*, 58(16):5477–5493, August 2013.

[88] Eric Brost and Yoichi Watanabe. Characterization of the cherenkov scatter function for use in superficial dose measurement from external beam radiation treatments. In *Optical Interactions with Tissue and Cells XXIX*, volume 10492, page 104920M. International Society for Optics and Photonics, 2018.

[89] T. Moffitt, Y.-C. Chen, and S.A. Prahl. Preparation and characterization of polyurethane optical phantoms. *Journal of Biomedical Optics*, 11(4), July 2006.

[90] J.-P. Bouchard, I. Veilleux, R. Jedidi, I. Noiseux, M. Fortin, and O. Mermut. Reference optical phantoms for diffuse optical spectroscopy. part 1 - error analysis of a time resolved transmittance characterization method. *Optics Express*, 18(11):11495–11507, May 2010.

[91] Daryoush SheikhBagheri and D. W. O. Rogers. Monte carlo calculation of nine megavoltage photon beam spectra using the beam code. *Medical Physics*, 29(3):391–402, March 2002.

[92] Varian monte carlo data package. https://varian.force.com/apex/CpMonteCarlo.

[93] Jacqueline M. Andreozzi, Rongxiao Zhang, Adam K. Glaser, Lesley A. Jarvis, Brian W. Pogue, and David J. Gladstone. Camera selection for realtime in vivo radiation treatment verification systems using Cherenkov imaging. *Medical Physics*, 42(2):994–1004, February 2015.

[94] Robert Dougherty. Extensions of damas and benefits and limitations of deconvolution in beamforming. In *11th AIAA/CEAS Aeroacoustics Conference*, Aeroacoustics Conferences, pages 2005–2961. American Institute of Aeronautics and Astronautics, 2005.

[95] Qi Shan, Jiaya Jia, and Aseem Agarwala. High-quality motion deblurring from a single image. *ACM Transactions on Graphics*, 27(3), August 2008.

[96] Ondfej Šindelář, Filip Šroubek, and Peyman Milanfar. A smartphone application for removing handshake blur and compensating rolling shutter. In *2014 IEEE International Conference on Image Processing (ICIP)*, pages 2160–2162. IEEE, 2014.

[97] Leah Bar, Nir Sochen, and Nahum Kiryati. Blind space-variant single-image restoration of defocus blur. In *International Conference on Scale Space and Variational Methods in Computer Vision*, pages 109–120. Springer, 2017.

[98] Filip Sroubek, Jan Kamenicky, and Yue M. Lu. Decomposition of space-variant blur in image deconvolution. *Signal Processing Letters, IEEE*, 23(3):346–350, March 2016.

[99] Leah Bar, Nir Sochen, and Nahum Kiryati. Restoration of images with piecewise space-variant blur. In *International conference on scale space and variational methods in computer vision*, pages 533–544. Springer, 2007.

[100] E Brost and Y Watanabe. A mathematical deconvolution formulation for superficial dose distribution measurement by Cerenkov light dosimetry. *Medical Physics*, 45(6):3880–3892, 2018.

[101] Igor V Meglinski. Quantitative assessment of skin layers absorption and skin reflectance spectra simulation in the visible and near-infrared spectral regions. *Physiological Measurement*, 23(4):741–753, November 2002.

[102] Steven L Jacques. Optical properties of biological tissues: a review. *Physics in Medicine and Biology*, 58(11):37–61, June 2013.

[103] A. Bhandari, B. Hamre, O. Frette, K. Stamnes, and J.J. Stamnes. Modeling optical properties of human skin using mie theory for particles with different size distributions and refractive indices. *Optics Express*, 19(15):14549–14567, July 2011.

[104] Daniel A. Low, William B. Harms, Sasa Mutic, and James A. Purdy. A technique for the quantitative evaluation of dose distributions. *Medical Physics*, 25(5):656–661, 1998.

[105] Tom Depuydt, Ann Van Esch, and Dominique Pierre Huyskens. A quantitative evaluation of imrt dose distributions: refinement and clinical assessment of the gamma evaluation. *Radiotherapy and Oncology*, 62(3):309–319, 2002.

[106] Ondrej Sindelar and Filip Sroubek. Image deblurring in smartphone devices using built-in inertial measurement sensors. *Journal of Electronic Imaging*, 22(1):011003–011003, 2013.

[107] Tod Lauer. Deconvolution with a spatially-variant psf. In *Astronomical Data Analysis II*, volume 4847, pages 167–174. International Society for Optics and Photonics, 2002.

[108] W. Xia and R.M. Lewitt. Fourier correction for spatially variant collimator blurring in spect. *IEEE Transactions on Medical Imaging*, 14(1):100–115, 1995.

[109] Ondrej Sindelar, Filip Scoubek, and Peyman Milanfar. Space-variant image deblurring on smartphones using inertial sensors. In *2014 IEEE Conference on Computer Vision and Pattern Recognition Workshops (CVPRW)*, pages 191–192. IEEE, 2014.

[110] Takanori Igarashi, Ko Nishino, and Shree K. Nayar. The appearance of human skin: a survey. *Foundations and Trends in Computer Graphics and Vision*, 3(1), January 2007.

[111] Eric Brost and Yoichi Watanabe. Characterization of the cerenkov scatter function: a convolution kernel for cerenkov light dosimetry. *Journal of Biomedical Optics*, 23(10):105007–105007, 2018.

[112] T.F Chan and Chiu-Kwong Wong. Total variation blind deconvolution. *IEEE Transactions on Image Processing*, 7(3):370–375, 1998.

[113] William Hadley Richardson. Bayesian-based iterative method of image restoration. *J. Opt. Soc. Am.*, 62(1):55–59, Jan 1972.

[114] L. B. Lucy. An iterative technique for the rectification of observed distributions. *Astronomical Journal*, 79(6):745–754, 1974.

[115] E. Chan and J. W. Goodman. Iterative statistical approach to blind image deconvolution. *Journal of the Optical Society of America*, 17(7):1177–1184, 2000.

[116] S. H. Chan, R. Khoshabeh, K. B. Gibson, P. E. Gill, and T. Q. Nguyen. An augmented lagrangian method for total variation video restoration. *IEEE Transactions on Image Processing*, 20(11):3097–3111, 2011.

[117] Warren J. Smith. *Modern Optical Engineering*. McGraw-Hill Companies, New York, NY, fourth edition, 2008.

[118] Frank L. Pedrotti, Leno M. Pedrotti, and Leno S. Pedrotti. *Introduction to Optics*. Pearson Education, London, UK, third edition, 2006.

[119] Fred E Nicodemus. Directional reflectance and emissivity of an opaque surface. *Applied optics*, 4(7):767–775, 1965.

[120] Stephen R Marschner, Stephen H Westin, Eric PF Lafortune, Kenneth E Torrance, and Donald P Greenberg. Image-based brdf measurement including human skin. In *Rendering Techniques 99*, pages 131–144. Springer, 1999.

[121] Jamil Lambert, Yongbai Yin, David R Mckenzie, Sue Law, and Natalka Suchowerska. Cerenkov light spectrum in an optical fiber exposed to a photon or electron radiation therapy beam. *Applied optics*, 48(18), 2009.

Appendix A

The Directional Radiance Distribution Function of Cerenkov Photons

Throughout the data presented in Chapter 5, evidence of a dependence on observed Cerenkov intensity as a function of the angle of observation was shown. Figure 5.8 shows that fluctuations exist in the central region of the Cerenkov images acquired from a curved surface using a open field photon beam. Ideally, no fluctuations would exist in the Cerenkov image profile in this region if the Cerenkov radiance followed a Lambertian distribution. Lambertian distributions have the property that the radiant intensity is observed as uniform irregardless of the angle between the observer and the light source [117]. A surface is said to be Lambertian if it obeys Lambert's Cosine Law. Lambert's Cosine Law states that the radiant intensity from a diffusive reflecting surface or an ideal diffuse radiator is directly proportion to the cosine of the angle between the observed light and the surface normal [118]. One common example of a Lambertian surface is a piece of white office paper, which has the same radiance when viewed from any angle. The same radiant intensity will be observed on the piece of office paper because, while the light reflected from the paper is reduced by the cosine of the emission angle, the area element observed by the viewer is increased by an equal amount (1/cosine). In the case of Cerenkov imaging, a remote camera is used to image Cerenkov radiance

from a diffuse radiator. While imaging a Cerenkov photons from a curved surface, the viewing angle is constant at any one point on the surface, but changes with the surface curvature. For more oblique observation angles on the curve, a larger source area will be perceived while the emission angle decreases. If the source radiating Cerenkov light is ideal, it would retain properties of a Lambertian surface. This however, does not appear to be the case for the optical phantom used in Chapter 5.

Outside of the work presented in Chapter 5, Zhang et. al (2016) also showed evidence that Cerenkov photons emitted from a phantom surface under EBRT exhibit a non-Labmbertian radiance distribution [55]. In order to perform quantitative dosimetry with Cerenkov photons, this radiance distribution must be accounted for with a correction factor. For many materials, the radiance distribution will depend on the material and surface structure [110]. For Lambertian reflectors, photons incident on the medium may be transmitted partially into the material and scatter multiple times before being remitted. This multiple scattering gives the surface the diffusive property and Lambertian radiance. For Cerenkov photons created in a material by EBRT, the initial directional properties of Cerenkov photons may alter the diffusion process. A Cerenkov photon that scatters only a few times before surface emission may retain some of its initial non-isotropic behavior. However, Chapter 4 showed that in an optical phantom model, Cerenkov photons are typically undergo more than 100 scattering events before surface emission. This should yield a more Lambertian-like radiance distribution for Cerenkov photons exiting the medium.

The aim of this appendix is to describe and measure the radiance distribution of Cerenkov photon generated by an external beam of photons or electrons incident on a medium. We refer to this distribution as the Directional Radiance Distribution Function (DRDF). In general, radiance distribution functions describe the dependence on the observed photon radiance as a function of imaging parameters. A commonly discussed radiance function is called as the Bidirectional Reflectance Distribution Function (BRDF), which describes the exiting radiance for optical photons reflected off of a material [119]. The DRDF differs from the BRDF in the source of the optical photons - in the DRDF, photons are emitted from within the material, and reflected multiple times before exiting.

Two methods were used to study the DRDF of Cerenkov photons from a medium

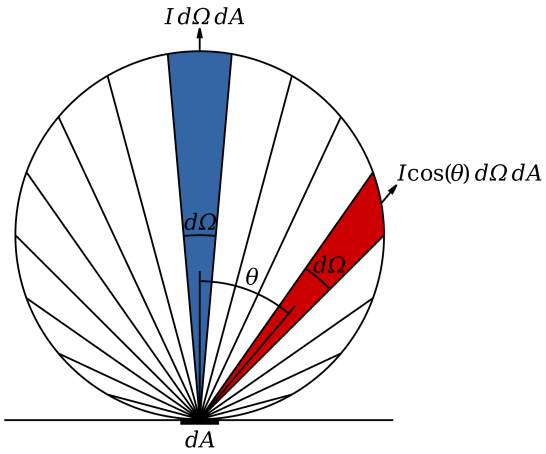

(a)

Figure A.1: The emission of photons in a normal and off-normal direction. The number of photons in any direction is proportional to the area of the wedge.

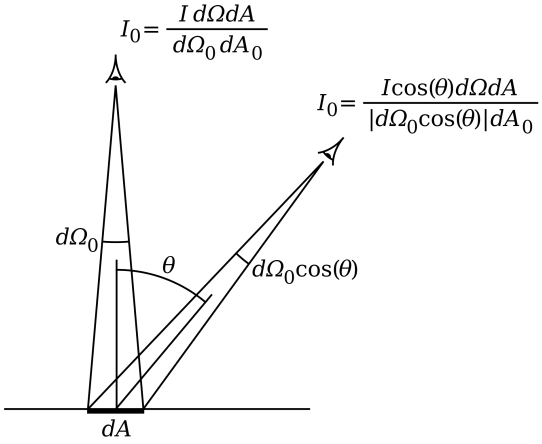

(a)

Figure A.2: The observed photon intensity (photons/(scm2sr)) in a normal and off-normal direction. dA0 is the area of the observation aperature and dω is the solid angle subtended by the aperture from the viewpoint of the emitter. This figure shows that the observed photon intensity is the same regardless of the observation angle.

generated by EBRT. The first was Monte Carlo using Gamos (version 4.0.0). The optical phantom and layered skin models described in Chapters 3 and 4 were used with a beam of primary radiation placed at 1 cm from the model surface. Cerenkov photons

exiting the front surface of the medium were scored and their position, wavelength, and direction were recorded. The simulated DRDF was solved using the final direction of the surface-escaped Cerenkov photons. Monte Carlo simulations were generated for a range of angles of incidence (Angle Study), field sizes (Field Study), and primary particle energies (Energy Study). Table A.1 displays the simulation parameters used in each study. All studies were repeated for both photon and electron beams.

The second method using to study the DRDF was by experiment. The same experimental set-up described in Chapter 3 was used to capture Cerenkov images taken from the flat optical phantom surface with a 5x5 cm^2 6 MV photon beam using a TrueBeam linac. A Canon EOS 6D camera (Canon USA) was placed 100 cm away from the isocenter on the treatment couch behind shielding. The treatment couch was rotated to the 90 degree position. The phantom was mounted to the linac gantry head and the front surface of the phantom was placed at isocenter at 100 SSD. The gantry was rotated from 0-45 degrees, and a irradiation was performed every 5 degrees to capture a Cerenkov image at these points.

Experimental Cerenkov images were perspective corrected and then time and spatially filtered using the same techniques as described in Chapter 3. The central 1x1 cm^2 area of the Cerenkov photon field was used as a reference area, from which the mean pixel value along with the standard deviation were extracted. This was performed over the range of available angles of observation at the different gantry positions.

Table A.1: The simulation parameters for Monte Carlo studies. These studies varied the beam angle, energy, and irradiated medium to measure the relative effects on the DRDF. Beam energies used were all monoenergetic (mono.). Phantom models used were the optical phantom (OP) and light skin. All listed studies were repeated for both photon and electon beams.

Study	Beam energy	Medium	θ_{in}	Field size
Angle	6 MV mono.	LS, OP	0-70°	pencil
Field	6 MV mono.	LS, OP	0°	0-20x20 cm^2
Energy	2-20 MV mono.	LS, OP	0°	pencil

Figure A.3 shows the DRDFs generated from the optical phantom and layered skin

models from the photon beam Monte Carlo studies plotted against a Lambertian distribution. Figure A.1(a) shows the mean DRDF values from the parameterization of changing the beam angle, beam energy, and field size in the optical phantom model. Figure A.1(b) shows the same values in the layered skin model. Figure A.1(c-d) shows the standard deviation of the DRDF as a function of observation angle for the optical phantom and layered skin models, respectively. Figure A.1(a-b) show that there was no dependence on angle, field size, and incident beam energy on the DRDF in either model. The DRDF generated from all studies is nearly identical within each material, and does not exactly follow a Lambertian distribution. The standard deviation of the DRDF is lowest around the angle of $\theta_{obs} = 0$ degrees. For all other angles, the standard deviation is below 1.3%. This could be further decreased by increasing the number of histories used to solve for the DRDF.

Figure A.3 does not display the data from the electron beam simulations. However, the electron beam simulations shared the same result as photon beams: there was no dependence on angle, field size, and incident beam energy on the DRDF. Therefore, the DRDF from electron beams in each model was displayed in Figure A.4, divided by the solid angle.

Figure A.4 shows the simulated DRDFs divided by the solid angle for electrons and photon beams, plotted against a Lambertian distribution. The solid lines in this figure were calculated as the mean of the Angle, Field, and Energy Study DRDFs shown in Figure A.1. Also shown in this figure is the BRDF from human skin, as measured by Marschner, *et.al.* (2011)[120]. For the optical phantom model, the deviation from a Lambertian distribution reaches up to 10% and 13% for electron beams and photon beams, respectively. These curves do not share the same shape as the measured human skin BRDF, but share a similar magnitude of deviation up to observation angles of 70 degrees. For the layered skin model, the DRDFs share a similar magnitude of deviation with the human skin BRDF up to 55 degrees. The magnitude of the DRDF falls of rapidly at more oblique observation angles in the human skin model.

Figure A.4(a) also shows the measured DRDF of the optical phantom, displayed as the circular points. These points were initially normalized to the 45 degree point in this trend, but then re-normalized to better match the data displayed in the range of 45-90 degrees. The measured DRDF follows a similar trend to that of the human skin BRDF

- a dip in the trend occurs at the 50 degree mark, followed by a slight increase for more oblique angles. The exact reason for this trend is unknown to the authors.

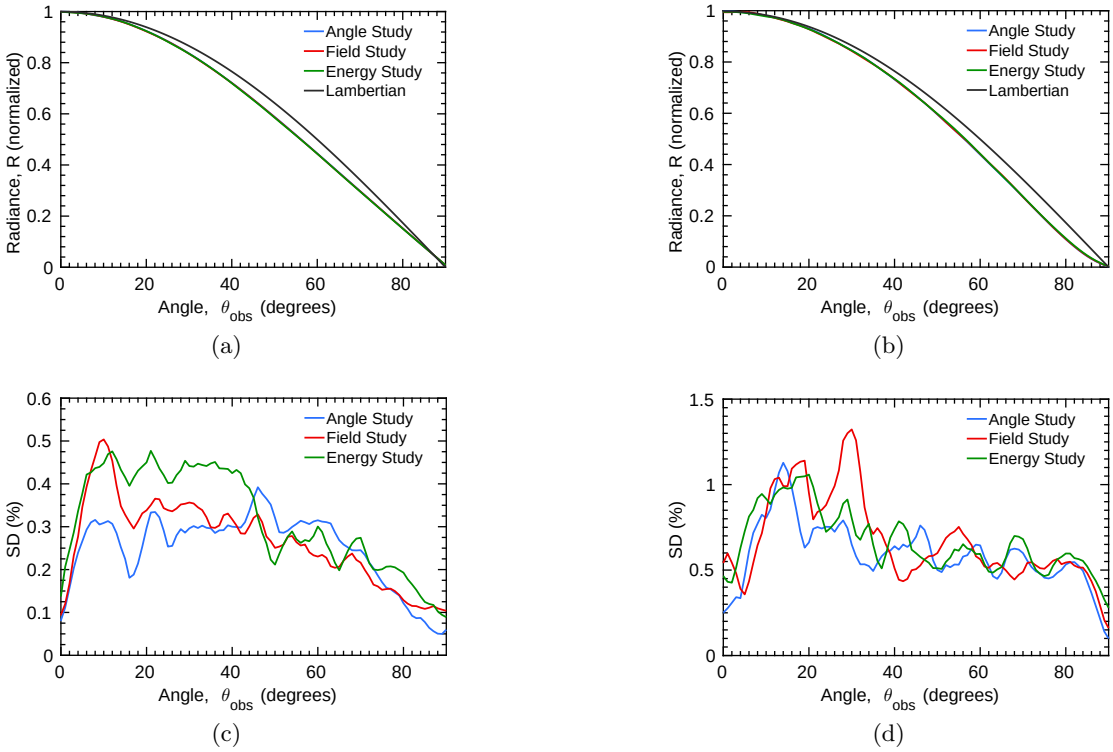

Figure A.3: The results of the Monte Carlo studies of the DRDF for photon beams. (a) The average DRDFs from the optical phantom with the standard deviation of each DRDF shown in (c). (b) The average DRDFs from the layered skin phantom with the standard deviation of each DRDF shown in (d). The average DRDF from each study are nearly identical and show no dependence on the incident angle, field size, or beam energy.

This appendix highlighted the importance of the DRDF for absolute dosimetry using Cerenkov photons. It was shown that Cerenkov light exits an medium under an external beam of radiation following a non-Lambertian distribution. Therefore, the observed Cerenkov radiance changes as a function of observation angle. The observed DRDF is dependent upon the irradiated material and particle type., but it is independent of incident angle, beam size, and beam energy. The measurements and simulations of the DRDF yielded different results. Refinement of these measurements is necessary before

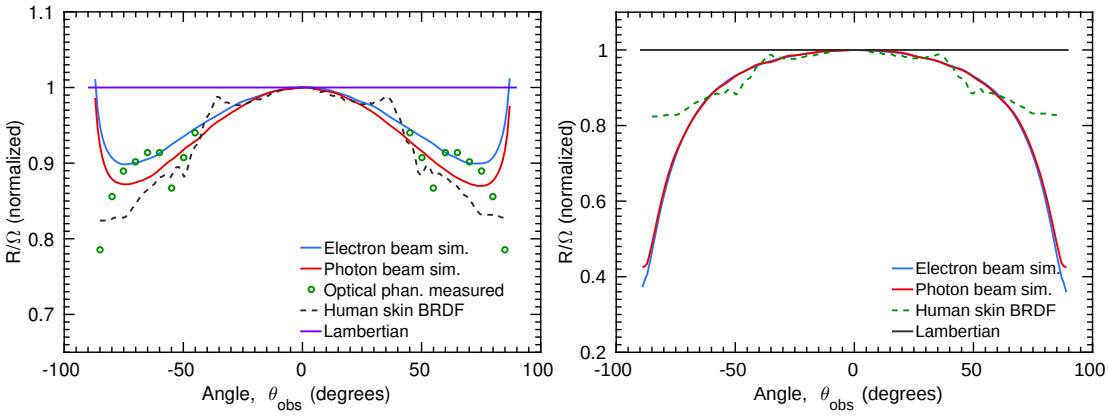

Figure A.4: Simulated and measured DRDFs for different particle types from (a) the optical phantom and (b) layered skin model. The BRDF for measured human skin is overlayed on the DRDF data for comparison.

application of the DRDF in Cerenkov light dosimetry.

Appendix B

Monte Carlo and Semi-analytical Forward Solutions for Cerenkov Imaging

In this section, a forward solution to equate a Cerenkov photon image is shown for both flat and curved surfaces. This method is contrary to the deconvolution techniques presented throughout this thesis; in deconvolution a Cerenkov photon image is used to solve for the primary beam fluence or superficial dose deposition. For the forward solution calculation, the primary beam fluence is known prior to the calculation, and used to solve for the Cerenkov photon image. Two separate methods were tested to equate the forward solution, a semi-analytical (SA) and a Monte Carlo (MC) method. For the SA method, Cerenkov scatter functions (CSFs) for normal and non-normal incident beam angles were pre-calculated using the data from Chapter 4. Both the SA and MC methods utilized the 6 MV phase space data from the Varian TrueBeam LINAC. The SA forward solution was calculated in Matlab (MathWorks, Natick, MA) and the MC forward solution was calculated using GAMOS (version 4.0.0) [3] with the Tissue Optical Modeling plugin [18].

To generate the SA forward solution, the primary beam fluence from the phase space data was used in conjunction with the set of CSFs. First, the phase space data was sampled on a virtual plane to solve for the primary particle position (X,Y,Z), incident

beam angle relative to the surface normal (θ_{in}), and beam rotation relative to the surface normal (ϕ) for primary photons entering a phantom. The phase space data was sampled on either a flat plane at 100 cm from the beam source or a curved plane with the apex at 100 cm from the beam source. Sampling occurred by scoring the primary beam fluence across the virtual plane. These planes correspond to the flat and curved phantom geometries described in Chapter 5. The particle energy was not scored when sampling the phase space data. The CSFs derived from Monte Carlo assumed the polyenergetic spectrum from a 6 MV photon beam on the TrueBeam LINAC. This spectrum was assumed for each primary particle in the SA forward solution irregardless of their individual energies.

For each primary particle, the corresponding CSF was identified using the incident beam angle (i.e. an incident angle of θ_{in} =15° corresponded to a 15° CSF). The corresponding CSF image was rotated to match the beam vector rotation using the *imrotate* function in Matlab. The rotated CSF image was cropped so that it was square with a 600x600 pixel size and 11x11 cm^2 dimensions. The resulting CSF was added to a composite image representing the X-Y coordinates of the primary fluence entrance points on the virtual plane. The composite image began as a null matrix with dimensions twice that of the CSF, being 1200x1200 pixels and 22x22 cm^2 in size. The CSF was added to the composite image such that the origin position of the CSF matched the entrance position of the primary beams. In this manner, as the CSFs from many primary beams were added to the composite image, a SA forward solution was built up over many computations. An image of this process applied to the curved surface beam fluence can be seen in Figure B.1, where 200, 10000, and 8e6 iterations of CSF additions are shown. This computation was repeated for both the flat and curved phantom geometries.

To generate the MC forward solution, the Cerenkov photon fluence was scored for photons exiting the flat or curved simulated phantoms in the MC simulations previously described in Chapter 5. SA and MC forward solutions were generated for a 5x5 cm^2 open field on the flat phantom and a 7.3x7.3 cm^2 open field on the curved phantom. Cross-line profiles were found for each image using the central 20% of the field size, and were compared against experimental Cerenkov photon images from both flat and curved phantoms taken from the data in Chapters 3 and 5. The metrics of field size and penumbra width were measured from each cross-line profile using the definitions

previously given in Chapter 3.

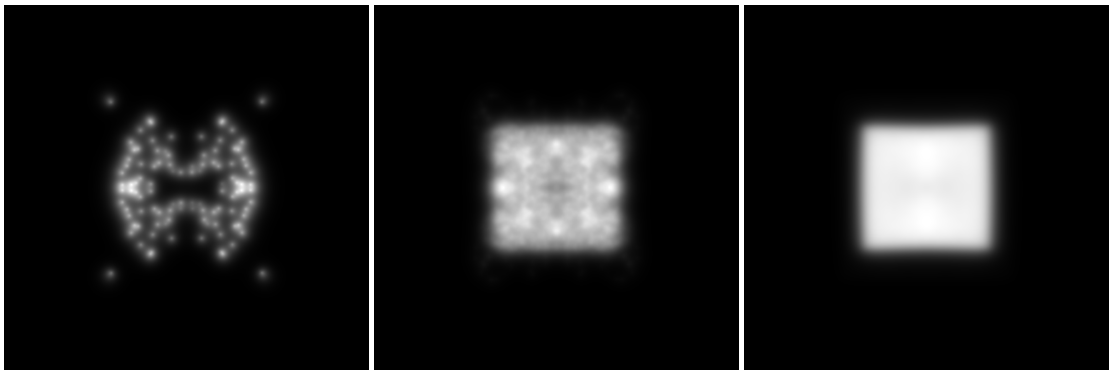

(a) (b) (c)

Figure B.1: Calculation of the semi-analytical (SA) forward solution to solve the Cerenkov image intensity on the curved optical phantom surface for a 7.3x7.3 cm^2 open field. To find this solution, the primary beam fluence incident on the phantom surface was first calculated using Monte Carlo simulation with a TrueBeam phase space file. For each primary particle, the corresponding CSF was found using the angle of incidence relative to the surface normal at the entrance point on the phantom. The CSF was then rotated to match the ϕ rotation of the entrance vector. After rotation, the CSF was added to a composite imge representing the running addition of many primary particles. (a) shows this calculation after 200 iterations, (b) shows 10000 iterations, and (c) shows 8e7 iterations, representing a SA forward solution calculation using a full phase space file.

Figure B.2 shows the forward solution profiles from a 5x5 cm^2 open field on the flat phantom. Three profiles are shown in this figure - the 5x5 cm^2 experimental Cerenkov image from the flat optical phantom, the SA forward solution, and the MC calculated Cerenkov photon fluence representing the MC forward solution. Here, it is seen that all three profiles are nearly identical. Figure B.2 shows the validity of both the SA and MC forward solutions for flat surface Cerenkov image calculation. Table B.1 contains the measurements of the field size and penumbra for all cross-line profiles shown in this figure. This table shows that a small discrepancy exists for the measured penumbra size for the imaged cross-line profile, however, the measured penumbra for the SA and MC forwards solutions are in good agreement.

Figure B.3 shows the forward solution profiles from a 7.3x7.3 cm^2 open field on the curved phantom surface. Three profiles are shown in this figure - the 7.3x7.3 cm^2

experimental Cerenkov image from the curved optical phantom, the SA forward solution, and the MC forward solution. Figure B.3(a) shows the profiles from the X-direction, with the curvature of the phantom. In Figure B.3(a), neither the SA forward solution nor the MC forward solution match the imaged profile. In particular, there are discrepancies between these profiles within the central region of the beam. These profiles do align fairly well at the periphery of the field in the penumbra region. Similar discrepancies exist between the profiles shown in Figure B.3(b), which is against the curvature of the phantom. Figure B.3(c) displays an expanded view of the left-side of Figure B.3(a). Table B.2 contains the measurements of the field size and penumbra for all cross-line profiles shown in Figure B.3.

It is unknown at this time as to why both the MC and SA forward solutions provide imprecise results on the curved surface as compared with experiment. However, the experimental Cerenkov images acquired from the curved surface do contain artifacts caused by the radiance function of Cerenkov photons exiting the irradiated medium, as discussed in Appendix A. It could be assumed that the MC forward solution shown here is the most correct solution, but further investigation is needed.

The SA forward solution on the curved surface shown in Figure B.3 used a space-variant CSF (CSFs ranging from $0^\circ \leq \theta_{in} \leq 30^\circ$). To test the accuracy of the SA forward solution on the curved surface, the calculation was repeated using a space-invariant CSF throughout the whole image ($\theta_{in} = 0^\circ$). The results of this test can be seen in Figure B.4, which shows profiles of the SA forward solution with a space-variant CSF, a space-invariant CSF, and the MC forward solution. Figure B.4(a) shows the profiles from the X-direction, with the curvature of the phantom. Assuming that the MC forward solution is the true solution, this figure shows that the space-variant SA calculation is more accurate than the space-invariant solution along the X-direction. At the periphery of the field in the X-direction, the primary beam angle of incidence increases due to both the beam divergence and the phantom curvature. This requires that the space-variant SA forward solution utilize a CSF corresponding to larger values of θ_{in}. The space-invariant calculation disregards all values of θ_{in}, and therefore provides an inaccurate solution in the X-direction.

Figure B.4(b) shows the profiles from the Y-direction, against the curvature of the phantom. Here, we see that the space-invariant calculation provides a similar solution

to the space-variant calculation in the penumbra region. At the periphery of the field in the Y-direction, the primary beam angle of incidence increases, but only due to the beam divergence and not the phantom curvature. Therefore, the space-variant SA calculation utilizes only the CSFs corresponding to small values of θ_{in}. This causes both the space-variant and space-invariant solutions to be similar in the penumbra region.

In the central regions of the beam in both the X and Y-directions, the space-variant SA profile contains fluctuations that do not match the MC forward solution. This is likely due to use of non-normal CSFs and application of a ϕ rotation. In theory, the space-variant SA calculation should match the MC profile. There may exist an error in the calculation, or a correction factor is required to improve the correspondence of these profiles. Further investigation is needed into the curved surface SA forward solution calculation.

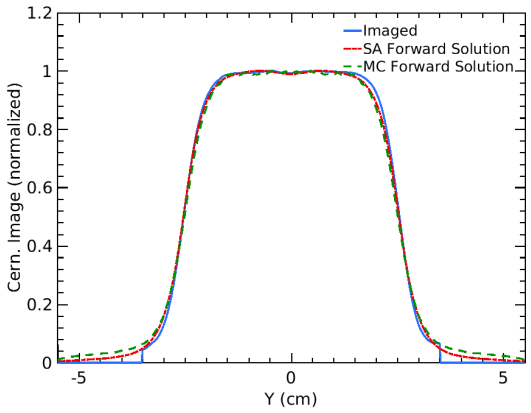

(a)

Figure B.2: The cross-line profiles from the forward solution calculations for the flat optical phantom using a 5x5 cm^2 open field. Three profiles shown are shown - the 5x5 cm^2 experimental Cerenkov image, the SA forward solution, and the MC forward solution.

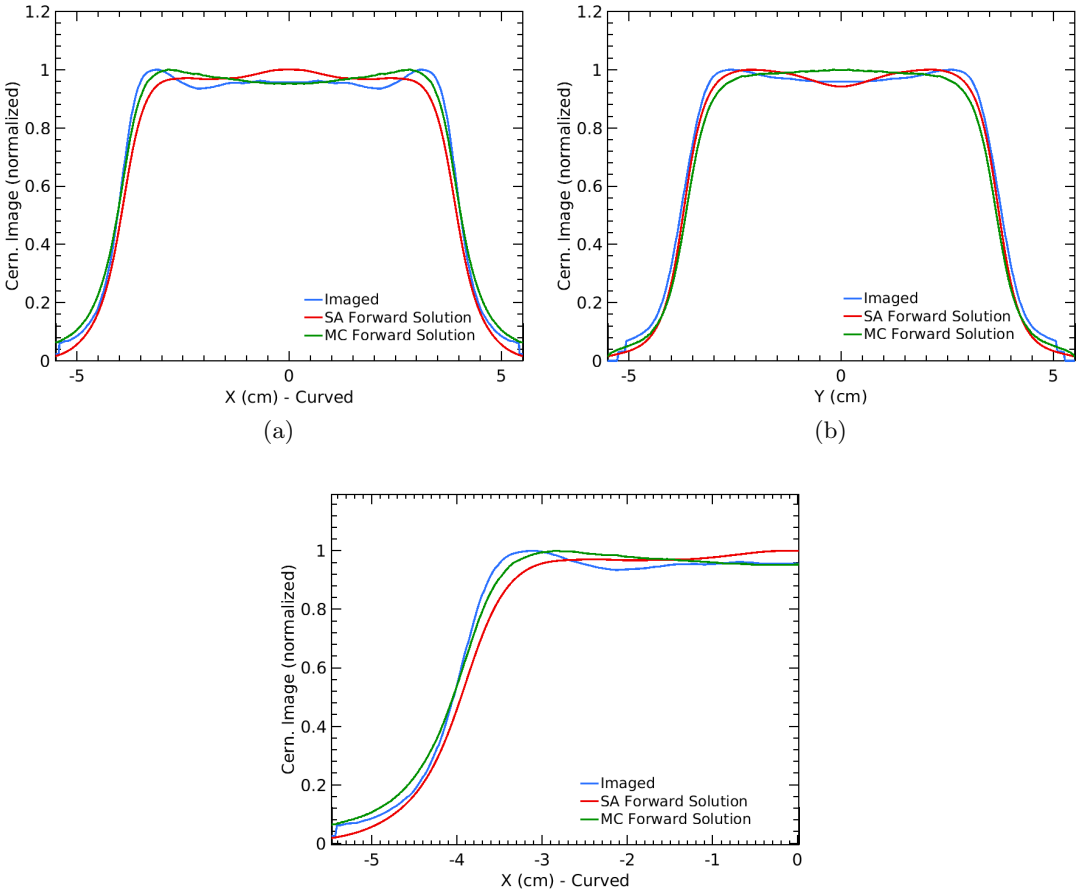

Figure B.3: The cross-line profiles from the forward solution calculations on the curved optical phantom using a 7.3x7.3 cm^2 open field. (a) shows X-direction profiles of both the SA Forward Solution and MC Forward Solution compared against the imaged profile. (b) shows Y-direction profiles for the same images. (c) shows an expanded view of the left side of (a).

Table B.1: The field size and penumbra width measured from the cross-line profiles of the Cerenkov image, the semi-analytical (SA) forward solution, and the Monte Carlo (MC) calculated forward solution. These measurements were taken using the 5.0x5.0 cm^2 open field incident on the flat optical phantom.

Profile	Field - X (cm)	Field - Y (cm)	Pen. - X (mm)	Pen. - Y (mm)
Imaged	5.13	5.08	5.75	6.39
SA	5.06	5.07	7.48	7.18
MC	5.01	5.02	7.66	7.71

Table B.2: The field size and penumbra width measured from the cross-line profiles of the Cerenkov image, the semi-analytical (SA) forward solution, and the Monte Carlo (MC) calculated forward solution. These measurements were taken using the 7.3x7.3 cm^2 open field incident on the curved optical phantom.

Profile	Field - X (cm)	Field - Y (cm)	Pen. - X (mm)	Pen. - Y (mm)
Imaged	8.07	7.57	7.00	7.97
SA	7.90	7.45	8.40	7.47
MC	8.08	7.32	8.80	8.31

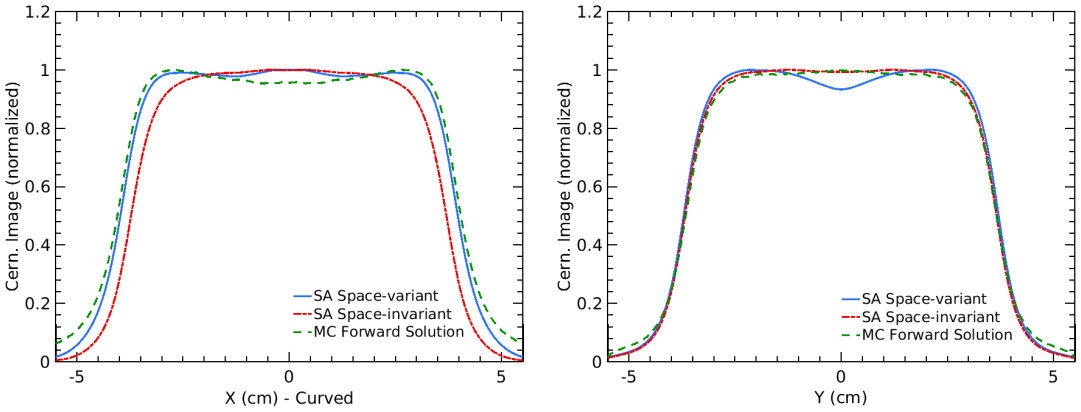

(a) (b)

Figure B.4: A test of using a space-invariant CSF on the SA forward solution from the curved phantom surface. The SA space-variant profile is the conventional calculation also shown in Figure B.3. (a) shows X-direction profiles of both Space-variant and Space-invariant SA forward solutions compared against the MC Forward Solution. (b) shows Y-direction profiles for the same images.

Appendix C

The Measured Cerenkov and Fluorescent Light Spectrum from 3D Printed Materials

An experiment was performed to measure the fluorescence spectrum from 3D-printed materials doped with strontium aluminate. While this was not directly applicable to the deconvolution imaging shown throughout this work, there is potential to extend the deconvolution techniques to fluorescent materials. Both Cerenkov and fluorescent photons are created in materials doped with a fluorophore under external beam irradiation. Both Cerenkov and fluorescent photons are subject to the same scattering and absorption and therefore, optical diffusion. Thus, an external beam of radiation incident on a fluorescent material generates a light profile on its surface that is composed of both fluorescent and Cerenkov photons. Similar mathematics to those introduced in Chapter 3 can be used to solve for the beam fluence from a light profile composed of both Cerenkov and fluorescent photons. The relative composition of fluorescent and Cerenkov photons would determine the weighting of a kernel that could be used in deconvolution. While the mathematics will not be shown here, this appendix will focus on finding the relative composition of photons from various fluorescent materials under external beam irradiation.

Three 3D printed materials were irradiated: A control sample was printed with no

doping using Esun natural ABS filament (Shenzhen Esun Industrial Co., Ltd), Sample A was printed using Esun luminous green filament, and Sample B was printed using luminous filament from 3D Solutech. Each sample was printed as a round cylinder with a 15 cm diameter and a 5 cm thickness. Samples were placed at the beam isocenter at a 120 cm source-to-surface distance. A f/4 collimating lens (Ocean Optics 84-UV-25) was placed above the sample, out of the radiation beam path. The lens was angled downwards toward the front surface of the 3D printed sample to collect photons that exited the sample. A 16 meter-long, 0.5 numerical aperture custom optical fiber (Thorlabs FP1000ERT) was attached to the collimating lens and routed light from the treatment room to the control room. The other end of the optical fiber was attached to an Exemplar Plus 25 um-slit cooled spectrometer (B & W TEK), which was operated using the default software in the control room. A 10x10 cone was used with 20 MeV electrons to irradiate all materials using a TrueBeam linac (Varian). The beam was run continuously at 1000 MU/min while the spectrometer collected exposures with a 5 min acquisition window. 5 averages were used for each sample to reduce noise in the spectrum signal.

Flourescent materials, whether transparent or opqaue to light, produce both fluorescent and Cerenkov photons [121, 11, 61]. The relative composition of the light spectrum from each sample was found as a linear combination of the raw fluorescent and Cerenkov photon spectra. The raw fluorescence spectrum was found using a pure sample of strontium aluminate, excited outside of the treatment room using a flashlight and then placed inside of a black box with the collimating lens. This spectrum can be seen in Figure C.1(a). The raw Cerenkov spectrum was acquired using the control sample under the external beam irradiation conditions listed above. This spectrum can be seen in Figure C.1(b). Using the Cerenkov and fluorophore spectra, a linear fit was performed on the sample spectra in Matlab (MathWorks) using custom written code.

In addition to the fluorescent and Cerenkov photons generated in the 3D printed samples, Cerenkov photons were created in the collimating lens and fiber due to stray radiation in the room. These photons were considered as noise in the collected signal and were removed from the final spectrum before processing. The Cerenkov spectrum from within the optical system was collected by imaging the control sample with a cover over the collimating lens.

Figure C.2(a-b) displays the spectrum and fit for Samples A and B. The relative light

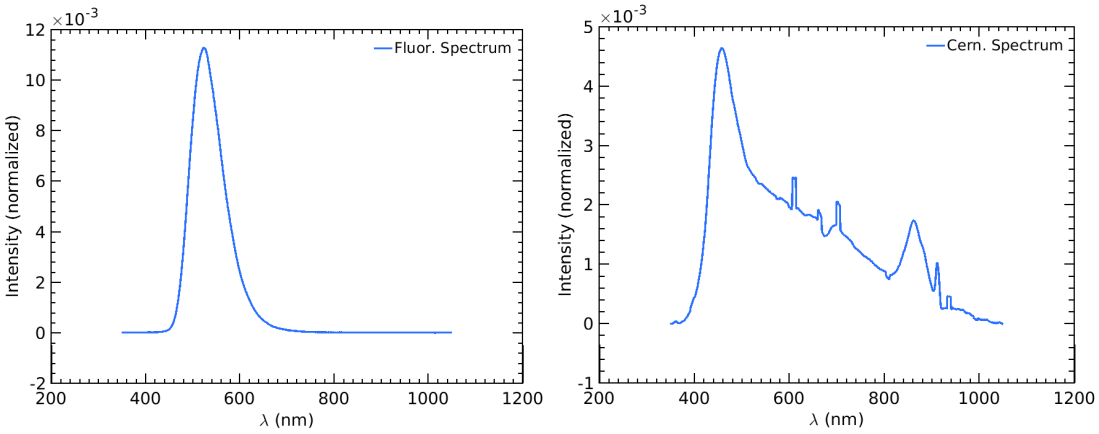

Figure C.1: (a) The fluorescence spectrum from strontium aluminate and (b) the Cerenkov spectrum from the 3D printed control sample. These spectra were used in linear combination to fit the experimental measured spectra from the fluorescent 3D printed test samples.

composition from each sample is roughly the same regardless of the filament. Between 60-66% of the light leaving the irradiated material is from Cerenkov photons and the remaining 34-40% is from fluorescence. This signals that a scattering kernel could be found as a linear combination using these relative values. Chapter 4 displays various kernels of Cerenkov origin, and a similar set of simulations could be made with pencil beam irradiations on a material with the fluorescent coefficients defined.

One factor not investigated in this experiment is using a fluorophore other than strontium aluminate. The quantum efficiency of the fluorophore used for doping will determine how many fluorescent photons are generated. This will affect the total composition of light exiting the irradiated material. Additionally, this study assumed a uniform distribution of fluorophores throughout the material. Additional factors could arise with an inhomogeneous distribution of fluorophores.

Of note, there are a few small artifacts shown in Figure C.1(b), seen as small bumps in the spectrum for wavelengths longer than 600 nm. A theoretical Cerenkov spectrum follows a $1/\lambda^2$ relationship following a cutoff frequency after which Cerenkov light is created[19]. The spectrum shown in Figure C.1(b) roughly follows this trend with a cutoff frequency around 400 nm. However, the presence of additional peaks at longer

wavelengths should not exist. We believe these peaks are from light emitting diodes on the TrueBeam linac that are used to sense any potential collisions between the gantry and a patient. These peaks were present in both the control and sample spectra acquisitions, therefore, did not have a significant effect on the linear fitting.

This experiment showed the relative composition of light exiting a 3D printed material doped with strontium aluminate under an external beam of radiation. About two-thirds of the light arises from Cerenkov interactions in the material. The remaining one-third of the light arises from fluorescence within the material.

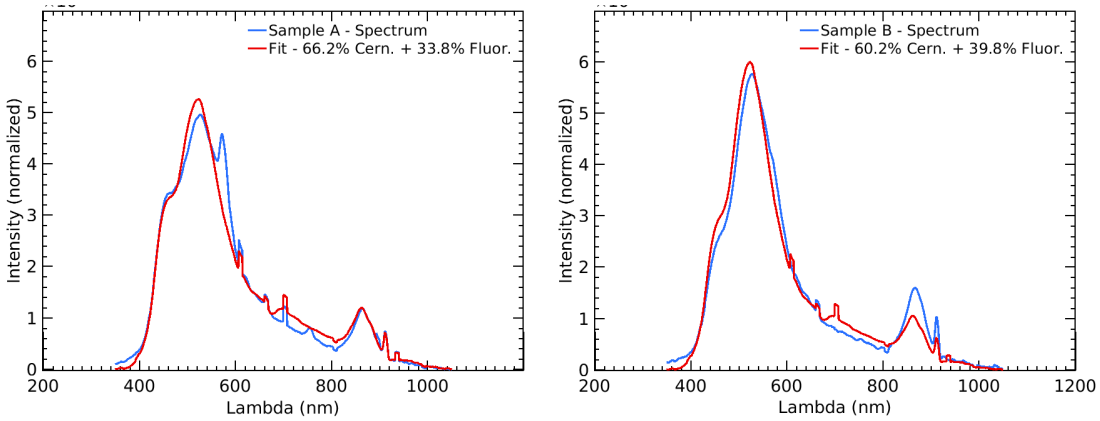

(a) (b)

Figure C.2: The measured photon spectrum from the 3D printed (a) Sample A and (b) Sample B. Each spectra has been fit with a linear combination of Cerenkov and fluorescent light to find the relative composition of the photons emitted from each sample. Sample A emitted 66.2% Cerenkov photons and 33.8% fluorescent photons under EBRT using electrons. Sample B emitted 60.2% Cerenkov photons and 39.8% flourescent photons under the same conditions.